Study of the Decay $K_L \to \pi^{\pm} e^{\mp} \nu e^{+} e^{-}$ to Probe the Semileptonic K-π Structure

by

Katsushige Kotera

DISSERTATION SUBMITTED TO

THE GRADUATE SCHOOL OF OSAKA UNIVERSITY

IN CANDIDACY FOR THE DEGREE OF

DOCTOR OF SCIENCE

September 2006

Abstract

We observed a new neutral kaon decay mode, $K_L \to \pi^{\pm} e^{\mp(}\bar{\nu}^{)} e^+ e^-$ for the first time. Based on the 20225 events including 1018 ± 25 background events, we determined the branching ratio, $B(K_L \to \pi^{\pm} e^{\mp(}\bar{\nu}^{)} e^+ e^-; M_{e^+e^-} > 5$ MeV/c^2, $E^*_{e^+e^-} > 30$ MeV$) = (1.281 \pm 0.041) \times 10^{-5}$. This branching ratio agrees with a theoretical prediction based on the chiral perturbation theory (χPT) calculation at $\mathcal{O}(p^4)$. Most of the kinematical distributions agree with the χPT $\mathcal{O}(p^4)$ calculation. We also measured one of the low energy coupling constants for the χPT $\mathcal{O}(p^4)$, $L_9^r = (8.0 \pm 1.6) \times 10^{-3}$. The $M_{e^+e^-}$ distribution below 100 MeV showed a 3 σ deviation from the χPT $\mathcal{O}(p^4)$ calculation. This requires further studies in theory and experiments.

Acknowledgment

First of all I would like to express my special thanks to my supervisor Prof. Taku Yamanaka for his advice, guidance, and friendship. I can not imagine how dull my student life would have been if I did not knock on the door of his room six years ago. He introduced me to a very special and fascinating world.

I would also like to give thanks to Prof. Yorikiyo Nagashima for giving me a theoretical foundation of high energy physics.

I would like to express my deepest gratitude to KTeV collaboration. My work is completely based on their great, bold, delicate, and precise experiments (I came to KTeV after the data taking was finished.). Especially, I am deeply grateful to Rick Kessler. Without him, this study would not have been done. Three hundred of my emails and three hundred of his replies flew across the Pacific Ocean or just the door to door of the HEP building in the Fermi Institute.

I owe thanks to Kentaro Tsuji and his advisor, Professor Toru Sato. This study could not done without their calculations as well as many discussions with them.

I would like to express my appreciation to the staff and students of Yamanaka-Taku lab. I have made extensive use of their lab's facilities, and their kindnesses have always helped me studying in lab. The discussions with Takanori Hara, Mitsuhiro Yamaga, and many admirable foregoers and many active junior fellows gave me meaningful hints for my study. Koji Hara and Hideki Miyake provided enjoyable and frank discussion with this elder colleague. Ken Sakashita's excellent work always encouraged me in my own work.

I would like to give special thanks to my family Noriko Nakazawa and Yuu Nakazawa for helping me keep my work and family life in balance. My family has been an oasis for me this long and challenging journey.

Thanks to my parents for their support and faith in me and for not saying "why didn't you study harder when you were younger".

Finally, I would like to express special appreciation for the social system in these beautiful islands especially that has developed from 60 years ago. This society has allowed me, not a rich man or a genius, but a husband and a father, to pursue my own passion for studying physics. Such a situation would absolutely never have been allowed in our society without large and hurtful change in 1945, when the average duration of a man's life was only 24 years.

Katsushige Kotera
August 2006

Contents

1 Introduction **1**

1.1 $K_L \to \pi^{\pm} e^{\mp(}\bar{\nu}^{)} e^+ e^-$ — a new K_L decay mode as a probe of kaon structure — 1

1.2 Physics of the $K_L \to \pi^{\pm} e^{\mp(}\bar{\nu}^{)} e^+ e^-$ decay 2

1.3 Expression of K-π current 3

1.3.1 Phenomenological form factor 3

1.3.2 The chiral perturbation theory 4

1.4 Photon radiation 5

1.4.1 Form factor and Low's theorem 5

1.4.2 The chiral perturbation theory 5

1.5 Evaluation of the chiral perturbation theory 6

1.5.1 Branching fraction 6

1.5.2 Comparisons of the spectra 6

1.6 Summary of introduction 7

2 Measurement Technique and Apparatus **9**

2.1 Overview 9

2.2 KTeV Experiment 10

2.3 K_L beams 11

2.4 The KTeV Detector 12

2.4.1 Overview of The KTeV Detector 12

2.4.2 The Decay Region 13

2.4.3 The Spectrometer 13

2.4.4 The Transition Radiation Detector 17

2.4.5 The Trigger Hodoscopes 18

2.4.6 The CsI Calorimeter 19

2.4.7 The Photon Veto System 22

2.4.8 Hadron Anti 23

2.4.9 The Muon System and Other Components 23

2.5 Trigger system 24

2.5.1 Level 1 Requirements 24

2.5.2 Level 2 Requirements 25

2.5.3 Level 3 Requirements 27

2.6 Monte Calro simulation 27

2.6.1 K^0 and $\bar{K^0}$ production and decay 28

2.6.2 $K_L \to \pi^{\pm} e^{\mp(}\bar{\nu}^{)} e^+ e^-$ decay generator 28

2.6.3 Other decay generators for normalization and backgrounds 29

2.6.4 MC for tracing of decay products 30

2.6.5 MC for detector responses 30

3 Analysis **35**

3.1 Event reconstruction and selection 35

3.1.1 The clustering, tracking, and vertexing 35

3.1.2 The particle identification 37

3.1.3 Cuts on the kaon energy, the squared longitudinal momentum of neutrino in the kaon rest frame, and the Z-vertex 39

3.1.4 The energy of observed particles in the laboratory frame 43

3.1.5 The invariant masses of some particle systems 43

3.1.6 A kinematic requirement to reduce $K_L \to \pi^+\pi^-\pi^0_D$ background . . . 45

3.1.7 Summary of the selection criteria 47

3.2 Background estimation 48

3.2.1 $K_L \to \pi^+\pi^-\pi^0_D$ 49

3.2.2 $K_L \to \pi^\pm e^\mp \nu \pi^0_D$ 51

3.2.3 $K_L \to \pi^+\pi^-\pi^0_{4e}$ 53

3.2.4 $K_L \to \pi^\pm e^{\mp(}\bar{\nu}^{)}\gamma$ 53

3.2.5 $K_L \to \pi^\pm e^{\mp(}\bar{\nu}^{)}$ double decays 53

3.2.6 $\Xi \to \Lambda(\to p\pi^-)\pi^0_D$ 54

3.2.7 A confirmation of background estimation using $P^{*2}_{\nu||}$ 54

3.3 Summary of the signal analysis 55

3.4 Kaon flux 56

3.4.1 Event selection for $K_L \to \pi^+\pi^-\pi^0_D$ 56

3.4.2 Background for the normalization analysis 61

3.4.3 Result of the kaon flux 61

4 The branching fraction analysis of $K_L \to \pi^\pm e^{\mp(}\bar{\nu}^{)}e^+e^-$ 63

4.1 Measurement of the branching fraction of $K_L \to \pi^\pm e^{\mp(}\bar{\nu}^{)}e^+e^-$ 63

4.2 Results of branching fraction 64

4.3 Systematic uncertainties of the branching fraction 64

4.4 Summary of the branching fraction of $K_L \to \pi^\pm e^{\mp(}\bar{\nu}^{)}e^+e^-$ 75

5 Evaluation of χPT[NLO(p^4)] 77

5.1 The branching fraction of $K_L \to \pi^\pm e^{\mp(}\bar{\nu}^{)}e^+e^-$ by χPT 77

5.2 Comparisons of spectra 78

5.2.1 The square of the transition momentum 78

5.2.2 The invariant masses 82

5.3 Result on the invariant mass: $M_{e^+e^-}$ 84

5.4 Discussions on the $M_{e^+e^-}$ 84

5.4.1 Possibility of a wrong estimation of backgrounds 84

5.4.2 Possibility of incorrect detector simulations 86

5.4.3 Discussions on the theoretical model 89

6 Conclusions 93

A A brief explanation of χPT 95

B The phase-space generator for $K_L \to \pi^{\pm} e^{\mp} \overset{(-)}{\nu} e^+ e^-$ 99

C Study of Pion-hadron interaction in TRD 107

D The index for π-e separation by TRD; $Prob_{\pi}$ 111

E Corrections for inefficiencies in π-e separations 115

E.1 The E/p selection. 115

E.2 The TRD selection 117

F Correction factor for the ratio that a pion misidentified as an electron 119

G The transition momentum 121

G.1 The effect of incorrect E_K selection 122

G.2 The effects of the selection cuts 123

G.2.1 Pion energy cut 123

G.2.2 The electron and positron energy cuts 124

G.2.3 The reason why the *Slope* is smaller for large electron energy 124

G.2.4 The reason of the difference between *Slope*s and shapes of t/M_π^2 for E_K maximum and for E_K minimum after $E_{e^+}, E_{e^-} > 3$ GeV cuts . . 126

G.2.5 Validation of the hypothesis of the effect of that t becomes greater than Q^2 126

G.3 data / MC-LO 129

G.3.1 The square of the transition momentum 129

G.4 Conclusions 129

H A study of the shift of Z-vertex of e^+e^- pair 131

Chapter 1

Introduction

1.1 $K_L \to \pi^{\pm} e^{\mp(}\bar{\nu}^{)} e^+ e^-$ — a new K_L decay mode as a probe of kaon structure —

We discovered a new neutral kaon decay mode, $K_L \to \pi^{\pm} e^{\mp(}\bar{\nu}^{)} e^+ e^-$. This mode is a radiative semileptonic kaon decay, $K_L \to \pi^{\pm} e^{\mp(}\bar{\nu}^{)} \gamma^*$, in which a virtual photon, γ^*, converts to e^+e^-. Figure 1.1 shows the Feynman diagrams of the $\bar{K}^0 \to \pi^+ e^- \bar{\nu} e^+ e^-$ decay; K^0 and $\bar{K}^0$ are the strong interaction eigenstates of neutral kaon, and K_L is a superposition of them. This mode was not noticed before our study, because the $K_L \to \pi^{\pm} e^{\mp(}\bar{\nu}^{)}$ events accompanying a positron-electron pair were considered as the $K_L \to \pi^{\pm} e^{\mp(}\bar{\nu}^{)} \gamma$ events, where the real photon converted into a e^+e^- pair in materials.

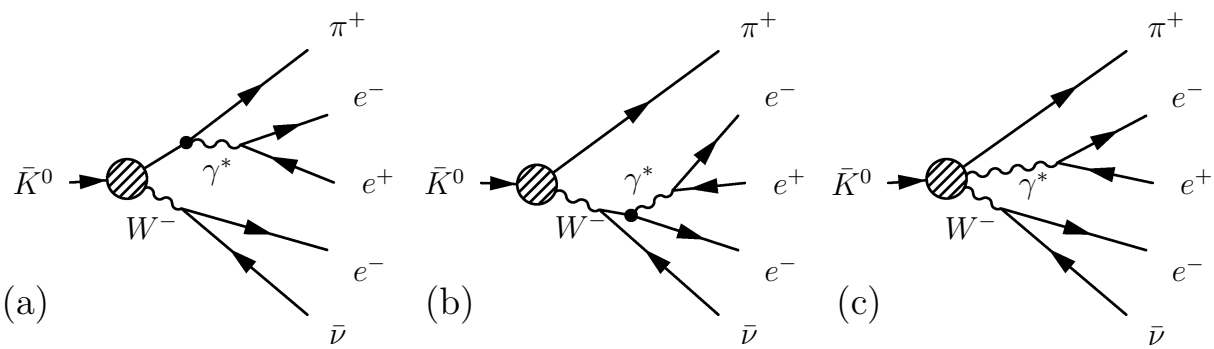

Figure 1.1: The Feynman diagrams of $\bar{K}^0 \to \pi^+ e^- \bar{\nu} e^+ e^-$; (a) a virtual photon is emitted from the charged pion, (b) from the electron, and (c) from the vertex. Note that (c) includes both inner bremsstrahlung and the direct emission term.

However, as shown in Fig. 1.2, we found events whose e^+e^- invariant mass are too large to have come from the external conversion. We have also confirmed that the e^+e^- pairs originate at the decay point.

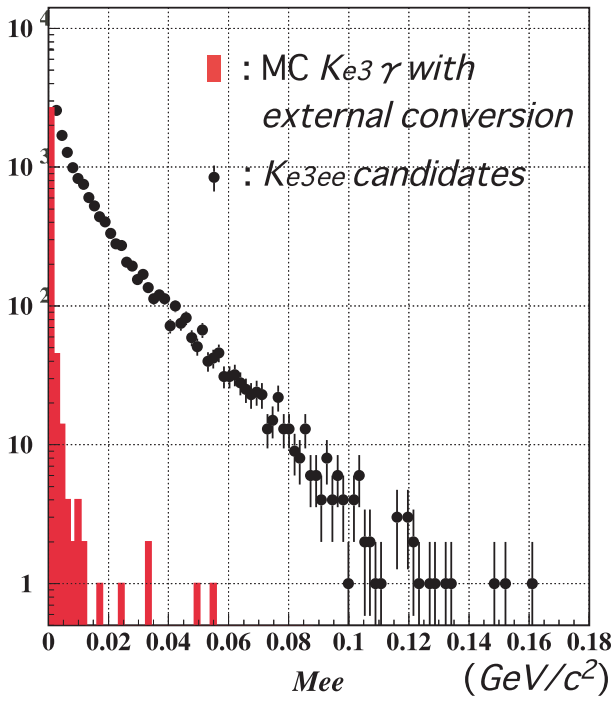

Figure 1.2: The invariant mass distribution of e^+e^- pair; Red histogram is the Monte Carlo simulation events of the radiative $K_L \to \pi^\pm e^{\mp(}\bar{\nu}^{)}$ with the external conversion in the detector materials. Dots are data of candidates of $K_L \to \pi^\pm e^{\mp(}\bar{\nu}^{)} e^+e^-$ events which we are going to investigate in this thesis.

1.2 Physics of the $K_L \to \pi^\pm e^{\mp(}\bar{\nu}^{)} e^+e^-$ decay

The $K_L \to \pi^\pm e^{\mp(}\bar{\nu}^{)}$ decay mode family, including $K_L \to \pi^\pm e^{\mp(}\bar{\nu}^{)}\gamma$ and $K_L \to \pi^\pm e^{\mp(}\bar{\nu}^{)} e^+e^-$ decay modes, contain electro-weak current and K-π hadronic current. The electro-weak current can be described precisely using standard perturbation theory. However, the K-π hadronic current obeys Quantum Chromodynamics (QCD), and the low energy QCD like in kaon decays cannot be calculated with perturbation in terms of quarks and gluons fields. We call this un-point-like structure as "K-π structure" in this study. The expression of the K-π structure is one of the difficulties in the $K_L \to \pi^\pm e^{\mp(}\bar{\nu}^{)}$ physics. It is interesting to study whether the model or theory that were used to explain the K-π structure in the $K_L \to \pi^\pm e^{\mp(}\bar{\nu}^{)}$ and $K_L \to \pi^\pm e^{\mp(}\bar{\nu}^{)}\gamma$ decay modes can also be applied to the $K_L \to \pi^\pm e^{\mp(}\bar{\nu}^{)} e^+e^-$

decay mode or not.

Some radiative photons in the $K_L \to \pi^{\pm} e^{\mp(} \bar{\nu}^{)} \gamma$ are expected to couple directly with the K-π structure. Therefore, we expect that the virtual photons in the $K_L \to \pi^{\pm} e^{\mp(} \bar{\nu}^{)} e^{+} e^{-}$ decay mode also couple to the K-π structure.

In the following two sections, we explain how the K-π current and photon radiation are represented theoretically.

1.3 Expression of K-π current

There are two ways to express the K-π current: phenomenological description using the form factor, and calculation with an effective theory.

1.3.1 Phenomenological form factor

The Lorentz invariance requires that the pseudo-scalar weak K-π current is represented by the four-vector momentum of kaon and pion, p_K and p_π, respectively, with the form factors as:

$$\langle \pi^-(p_\pi) | \, \bar{s}\gamma^\mu u \, | K^0(p_K) \rangle = f_+(t)(p_K + p_\pi)^\mu + f_-(t)(p_K - p_\pi)^\mu \tag{1.1}$$

where $t = (p_K - p_\pi)^2$. The contribution of $f_-(t)$ is small for the $K_L \to \pi^{\pm} e^{\mp(} \bar{\nu}^{)}$ decay modes because it is proportional to $m_e/m_K \simeq 10^{-6}$. Therefore, we discuss only $f_+(t)$ for $K_L \to \pi^{\pm} e^{\mp(} \bar{\nu}^{)}$ and $K_L \to \pi^{\pm} e^{\mp(} \bar{\nu}^{)} \gamma^{(*)}$ decay modes. The $f_+(t)$ is described in the series with the experimental parameters, λ's, as:

$$f_+(t) \quad = \quad f_+(0)\Big(1 + \lambda'_+ \frac{t}{m_\pi^2} + \frac{1}{2}\lambda''_+ \frac{t^2}{m_\pi^4} + \cdots\Big), , \tag{1.2}$$

The latest values of λ's in the liner and the quadratic models were measured by KTeV [1]. In the linear parameterization, the λ'_+ was determined as $(28.32 \pm 0.57) \times 10^{-3}$ for the $K_L \to \pi^{\pm} e^{\mp(} \bar{\nu}^{)}$ decay mode.

1.3.2 The chiral perturbation theory

One of the effective theories to express the K-π structure is the Chiral Perturbation Theory (χPT). χPT is based on the symmetry principle of QCD (chiral symmetry). The essential points in the χPT for our study are as follows [2].

1. The massless pseudo-scalar mesons, called Nambu-Goldstone bosons (NGB's), appear when the chiral symmetry breaks spontaneously [3, 4].

2. Assuming that u, d, s quarks are massless, and using the flavor $SU(3)_L \times SU(3)_R$ symmetry among them, the NGB's correspond to our real pseudo-scalar mesons, $K, \pi,$ and η.

3. The fields are written in a unique Lagrangian.

4. The Lagrangian can be expanded by the square of the momentum of the fields (p^2) using a perturbation method.

5. The masses of pseudo-scalar mesons arise from the finite quark masses, and this is calculated perturbatively by adding a mass term in the Lagrangian.

6. The couplings of electro-magnetic fields, A_μ, and weak fields, W_μ^+, are included in the covariant derivative as the gauge principle.

A brief explanation of χPT is given in Appendix A. The most important point is that χPT is based on the underlying QCD theory, and once the highest expansion order for p is chosen, χPT gives a unique prediction.

The lowest transition amplitude has a point-like K-π current (LO) and the higher order corrections represent the structure of the K-π current [NLO(p^4), (p^6), $\cdots$]. Although the low energy coupling constants of each term of Lagrangian of NLO cannot be determined by the theory, they are provided by other experiments, because the χPT can describe various decays universally.

Because of the universality of χPT, the decay $K_L \to \pi^{\pm} e^{\mp(}\bar{\nu}^{)}$, $K_L \to \pi^{\pm} e^{\mp(}\bar{\nu}^{)}\gamma$, and $K_L \to \pi^{\pm} e^{\mp(}\bar{\nu}^{)} e^{+} e^{-}$ can be treated systematically.

1.4 Photon radiation

1.4.1 Form factor and Low's theorem

Fearing *et al.* calculated the matrix element for the $K_L \to \pi^{\pm} e^{\mp(}\bar{\nu}^{)}\gamma$ decay [5]. The photon radiation was attached to the $K_L \to \pi^{\pm} e^{\mp(}\bar{\nu}^{)}$ decay, following to Low's theorem [6]. In this case, the form factor should be provided by experiments. The photon coupling with the structure of K-π current cannot be obtained from the theory.

1.4.2 The chiral perturbation theory

The χPT determines photon emission systematically. Additionally, the photon emission coupling with the structure of K-π current is provided uniquely by χPT. Figure 1.3 shows the examples of photon coupling with the NGB fields, and a photon coupling with their vertex representing the K-π structure. In this case, the photon emissions depend on the field and vertex.

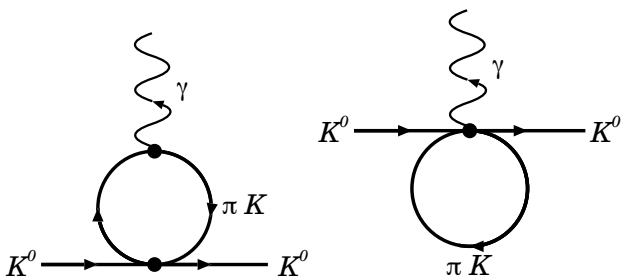

Figure 1.3: Diagrams for neutral kaon form factor at NLO, as an example of NLO diagram [7].

1.5 Evaluation of the chiral perturbation theory

As discussed in above sections, χPT is systematically expanded to describe the $K_L \to \pi^{\pm} e^{\mp} \overset{(-)}{\nu}$, $K_L \to \pi^{\pm} e^{\mp} \overset{(-)}{\nu} \gamma$, and $K_L \to \pi^{\pm} e^{\mp} \overset{(-)}{\nu} e^{+} e^{-}$ decays. Therefore, using the newly discovered $K_L \to \pi^{\pm} e^{\mp} \overset{(-)}{\nu} e^{+} e^{-}$ decay, we can test this systemicity of χPT, and probe the K-π structure.

The absolute square of the amplitude of the $K_L \to \pi^{\pm} e^{\mp} \overset{(-)}{\nu} e^{+} e^{-}$ decay mode by χPT-LO and NLO(p^4) are calculated by Tsuji [7].

1.5.1 Branching fraction

We will first measure the branching fraction of the $K_L \to \pi^{\pm} e^{\mp} \overset{(-)}{\nu} e^{+} e^{-}$ decay. According to the Tsuji's amplitudes, the branching fractions by LO calculation is 5.8% smaller than NLO(p^4) calculation.

The comparison of the branching fraction between data and the theoretical prediction based on χPT[NLO(p^4)] and LO is a good test of the expression of π-e structure by NLO(p^4).

1.5.2 Comparisons of the spectra

Figure 1.4 shows the theoretical prediction of the ratio of $\sqrt{t}$ distribution by LO and NLO(p^4). The ratio varies up to 26% and it shows that the t is sensitive to the structure of K-π current. We will compare the t distribution of data and χPT [NLO(p^4)].

In the LO calculation, the form factors are constant numbers. The NLO(p^4) gives corrections to these form factors. The most significant correction is one of the low energy coupling constants of χPT, called L_9^r [7]. We will measure L_9^r based on the spectrum of t.

We will also compare the invariant mass of e^+e^- pair ($M_{e^+e^-}$) distribution between data and the theoretical predictions. Figure 1.5 shows the ratio of the theoretical predictions of the $M_{e^+e^-}$ distribution by LO and NLO(p^4). The effect of NLO(p^4) correction on the $M_{e^+e^-}$

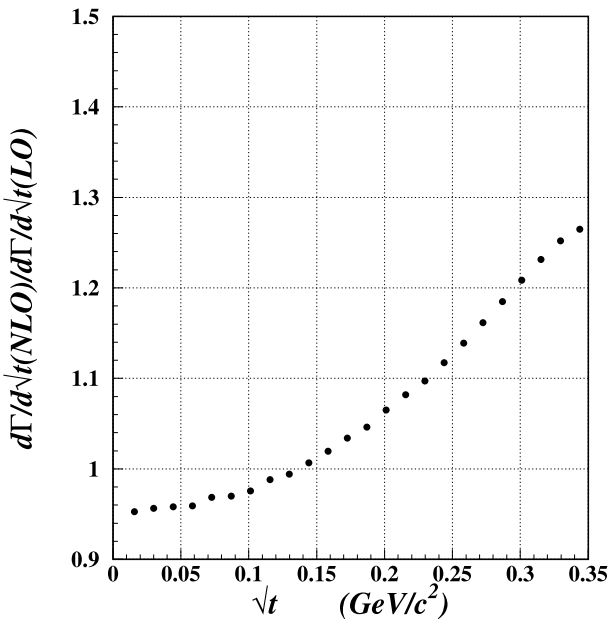

Figure 1.4: A theoretical prediction for the ratio of $\sqrt{t}$ distribution by NLO(p^4) to by LO [7].

distribution is smaller than the effect on t. However, this kinematical variable cannot be observed in the $K_L \to \pi^{\pm} e^{\mp} \overset{(-)}{\nu} \gamma$ decays with real photons. The none zero $-q^2 = M_{e^+e^-}{}^2$ has possibility to show a different effect of K-π structure which vanishes in the $K_L \to \pi^{\pm} e^{\mp} \overset{(-)}{\nu} \gamma$ decay.

1.6 Summary of introduction

We found a new neutral kaon decay mode, $K_L \to \pi^{\pm} e^{\mp} \overset{(-)}{\nu} e^+ e^-$. In this thesis, we will use this decay mode to study the universality of χPT in the $K_L \to \pi^{\pm} e^{\mp} \overset{(-)}{\nu}$ decay family, by measuring the branching fraction, and by comparing t and $M_{e^+e^-}$ distributions.

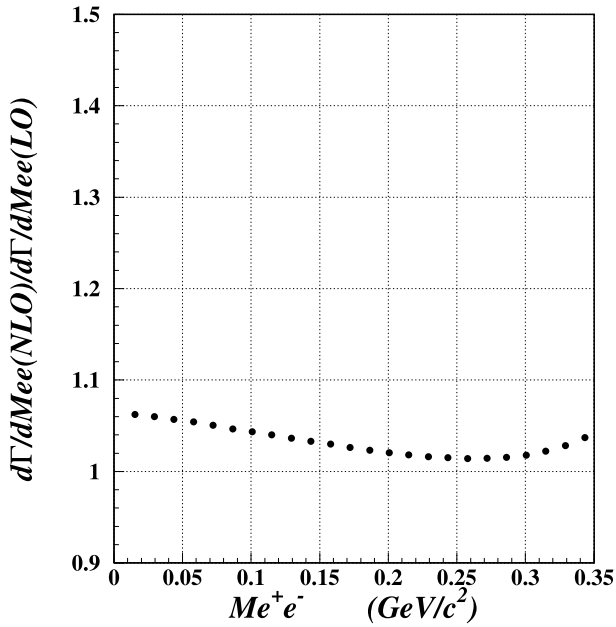

Figure 1.5: A theoretical prediction for the ratio of $M_{e^+e^-}$ distribution by NLO(p^4) to by LO [7].

Chapter 2

Measurement Technique and Apparatus

2.1 Overview

The $K_L \to \pi^{\pm} e^{\mp(}\bar{\nu}^{)} e^{+} e^{-}$decay has four charged particles in its final state. The signature of the decay is one charged pion and three electrons coming from the same vertex.

One of the dominant background to this decay mode is $K_L \to \pi^+\pi^-\pi^0_D$ with a pion misidentified as an electron, where π^0_D denotes the decay $\pi^0 \to e^+e^-\gamma$. Therefore, π-e rejection is crucial for this measurement. The $K_L \to \pi^+\pi^-\pi^0_{4e}$ decays, where π^0 decays into four electrons, are also a large background. Both backgrounds are rejected using a kinematical feature of $K_L \to \pi^+\pi^-\pi^0$ decays. Therefore, a precise momentum measurement is also crucial. Another large background comes from the $K_L \to \pi^{\pm}e^{\mp}\nu\pi^0_D$ decays. Estimated amount of the $K_L \to \pi^{\pm}e^{\mp}\nu\pi^0_D$ background is assured by information of photon. Therefore we should measure the photon energy and position.

Therefore, detector elements are required to have following functions:

- Momentum measurement of charged particles
- Identification of $e^{\pm}, \pi^{\pm}$ and $\mu^{\pm}$.
- Photon energy and position measurements

The KTeV detector satisfies these requirements.

In order to measure the branching fraction of $K_L \to \pi^{\pm} e^{\mp(}\bar{\nu}^{)} e^+ e^-$ and to estimate the number of background events, we need to know the number of kaon decays during the measurement. This number is referred to as a kaon flux. We used the $K_L \to \pi^+\pi^-\pi^0_D$ decay mode as a normalization mode to measure the kaon flux, because it also has four charged particles, pions and electrons, and its branching fraction is large, and known precisely.

Besides collecting data in the experiment, we also ran Monte Carlo simulation (MC) of the experiment. The MC was used:

- to determine the acceptance of signal mode, normalization mode, and background modes,
- to understand the distribution of kinematic observables to separate signal mode from background modes, and
- to verify the theory we want to investigate.

In this chapter, we describe the detector and MC for our experiment.

2.2 KTeV Experiment

The KTeV experiment at Fermilab consisted of two experiments; E832 to measure the direct CP violation parameter, $Re(\epsilon'/\epsilon)$, and E799-II to study rare K_L decay processes [8, 9]. Both experiments used the same beam-line and detector, except for some minor differences.

For this thesis, we used data set acquired by E799-II from January to March of 1997 (*the Winter '97 data*).

2.3 K_L beams

The Fermilab *Tevatron* provided a proton beam to produce neutral kaons. The protons were accelerated by the 53 MHz radio frequency (RF) resonant cavities up to the energy of 800 GeV. This acceleration took 40 seconds. After acceleration, the protons were delivered continuously for 20 seconds referred to as a spill. The number of protons per spill was $(2-4)\times 10^{12}$. The proton beam had a 53 MHz RF structure, bunched in 1 ns wide *buckets*, spaced by 19 ns.

After being focused to a width of less than 250 μm, the proton beam bombarded a Berium oxide (BeO) target. The target was 30 cm long (about one proton interaction length), and had a 3 mm squared cross-section. The incident proton beam was directed downwards at an angle of 4.8 mrad.

The coordinate system in this study is defined that the center of the target is the origin of the coordinate, and downstream horizontal direction along beams is the positive z axis. The y axis is defined as vertically pointing up. The three axes are defined with the right-handed coordinate system.

Of the particles produced in the target, charged particles were swept out by a set of sweeping magnets located downstream of the target. A Pb absorber at z = 18.5 m converted photons into e^+e^-, and the electrons were removed by the sweeping magnets. After charged particles and photons were removed, two nearly parallel neutral beams were defined with a primary collimeter with two square holes, placed at z = 19.8 m. A steal slab collimeter at z = 38.8 m prevented particles from crossing to the other beam. At z = 85 m, a steel collimeter defined the final dimensions of the beams. Each beam had square dimensions of 0.5 mrad $\times$ 0.5 mrad. A schematic view of the elements used to produce the neutral beam are shown in Fig. 2.1, and their functions and locations are listed in Table 2.1.

After passing through these elements, two neutral beams entered the KTeV decay region starting at z=93 m. At this point, the beam composition was 3:1 neutron to K_L with small fractions of remaining K_S, Λ^0, and Ξ^0 [10]. The neutral hadron rate was between 25 MHz

Table 2.1: A list of elements for the KTeV neutral beam line. (for *winter '97*)

Element	+z (m)	Purpose or description
Target sweeper	0.6-4.4	To deflect residual protons in to a beam dump (475 MeV/c).
Primary proton dump	4.5-	Water-cooled copper.
μ sweep1	12.3-17.8	3806 MeV/c transverse momentum kick.
Pb absorber	19-	To convert photons into e^+e^- pairs.
Primary collimator		To make two neutral beams.
Titanium window	21.8	Beginning of the vacuum region.
μ sweep2		To deflect charged particles created in Pb absorber, primary collimator, and the titanium window with a 3135 MeV/c transverse momentum kick.
Spin rotator dipole	30.5-36.5	used only for hyperon studies.
Slab collimator	38.8-40.8	To prevent crossover between the two beams.
Iron beam stop	46.4-52.4	To stop neutral beam during beam access and calibration runs with muon.
Defining collimator	85m-	Final shaping of the K_L beams.
Final sweeper		To remove charged particles from the defining collimator and upstream.

and 50 MHz.

2.4 The KTeV Detector

2.4.1 Overview of The KTeV Detector

Figure 2.2 shows a schematic 3D drawing of KTeV detector, and Fig. 2.3 shows the z-x plan view.

KTeV detector was designed to collect decays in a 70 m vacuum region. Following a thin vacuum window at the end of the vacuum region was a drift chamber spectrometer. The spectrometer had two pairs of drift chambers separated by an analysis magnet. A set of transition radiation detectors (TRD) [11] behind the drift chambers was used for π-e rejection. Farther downstream, there were a trigger hodoscope, a pure CsI electromagnetic calorimeter, and a muon system. Particles escaping the detector were vetoed by the photon vetoes positioned around the vacuum decay region, the spectrometer, and the calorimeter. We present a brief explanation for each part of apparatus in the following sections.

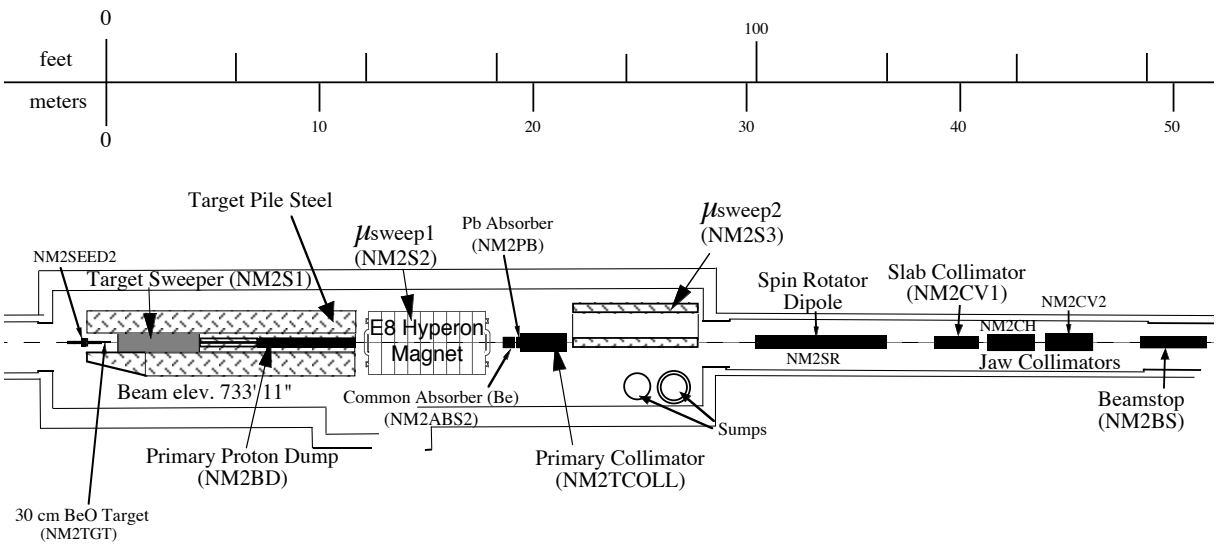

Figure 2.1: Secondary beamline components at the downstream of the KTeV target.

2.4.2 The Decay Region

We collected K_L decays in the decay region from z = 93 m to z = 159 m. The vacuum tank started at z=22 m, and ended at 159 m with a 1.8 m diameter *Vacuum window* made of Kevlar laminated with Mylar (a total of 0.0015 radiation lengths) to keep 10^{-6} Torr vacuum. There were five stages of ring-shaped veto counters inside the tank to detect particles escaping this region. These veto counters are discussed in Section 2.4.7.

2.4.3 The Spectrometer

In order to measure the momenta of charged particles and to trace their trajectories, the KTeV spectrometer was placed immediately downstream of the Vacuum window. The spectrometer consisted of two pairs of drift chambers separated by an analysis magnet. The analysis magnet had an aperture of 3×2 m^2 and provided a 0.205 GeV/c transverse momentum kick in '97 experiment deflecting the charged particles in the x-z plane. The polarity of the magnetic field was reversed every 1– 2 days, to cancel out any possible left/right systematic effects. The magnet made a non-negligible *fringe field* which extended past chamber 2 and 3 and slightly displaced the hit positions in those chambers. The magnitude of the *fringe field* was less than 1% of the analysis magnetic field.

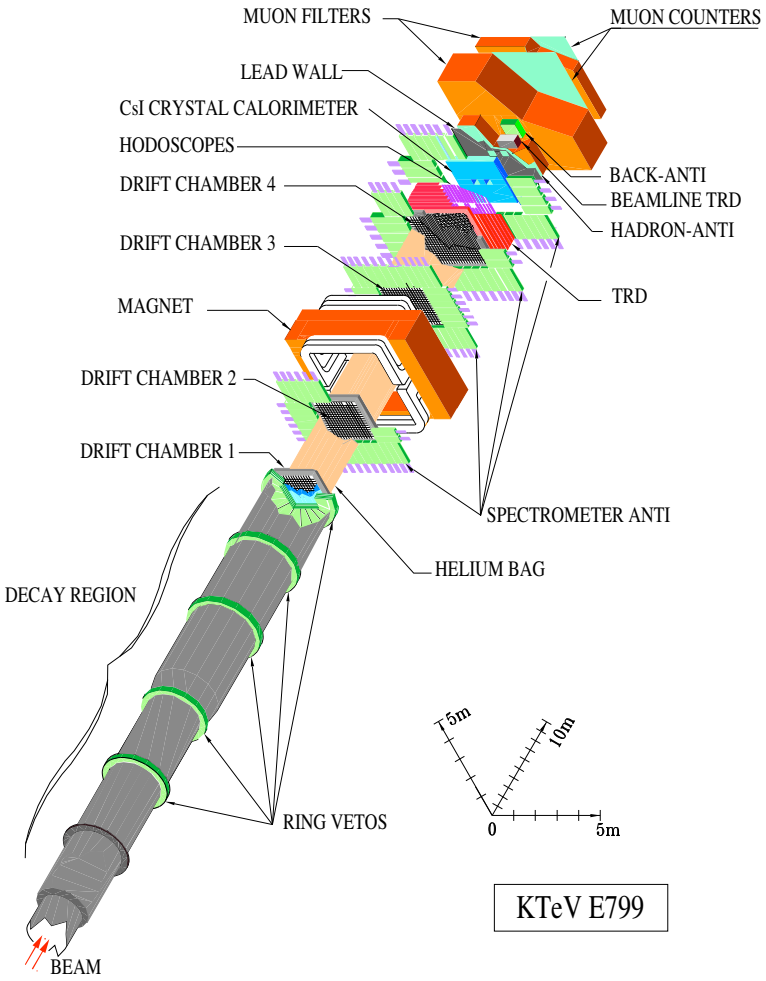

Figure 2.2: The KTeV detector. The axis parallel to the beam defines z and is compressed by a factor of 2 relative to the transverse directions.

Each drift chamber was composed of a set of a horizontal wire chamber (to measure the y position) and a vertical wire chamber (to measure the x position). The chamber in each view consisted of two sense wire planes. As shown in Fig. 2.4, each sense wire (25 μm diameter gold-plated tungsten) was centered in a hexagonal cell structure of the cathode field wires (100 μm diameter gold-plated alminum). The cathode field wires were supplied with a high negative voltage typically between 2450 V and 2600 V. Each cell was 12.7 mm wide and the adjacent sense plane was staggered by 6.35 mm.

The chambers were filled with Argon/Ethan gas mixture (Ar : Ethane : iso-propanol = 49.75 : 49.75 : 0.5). When a charged particle passed through the drift chamber and ionized the gas inside, the electrons by ionizations drifted to the closest anode sense wire. The

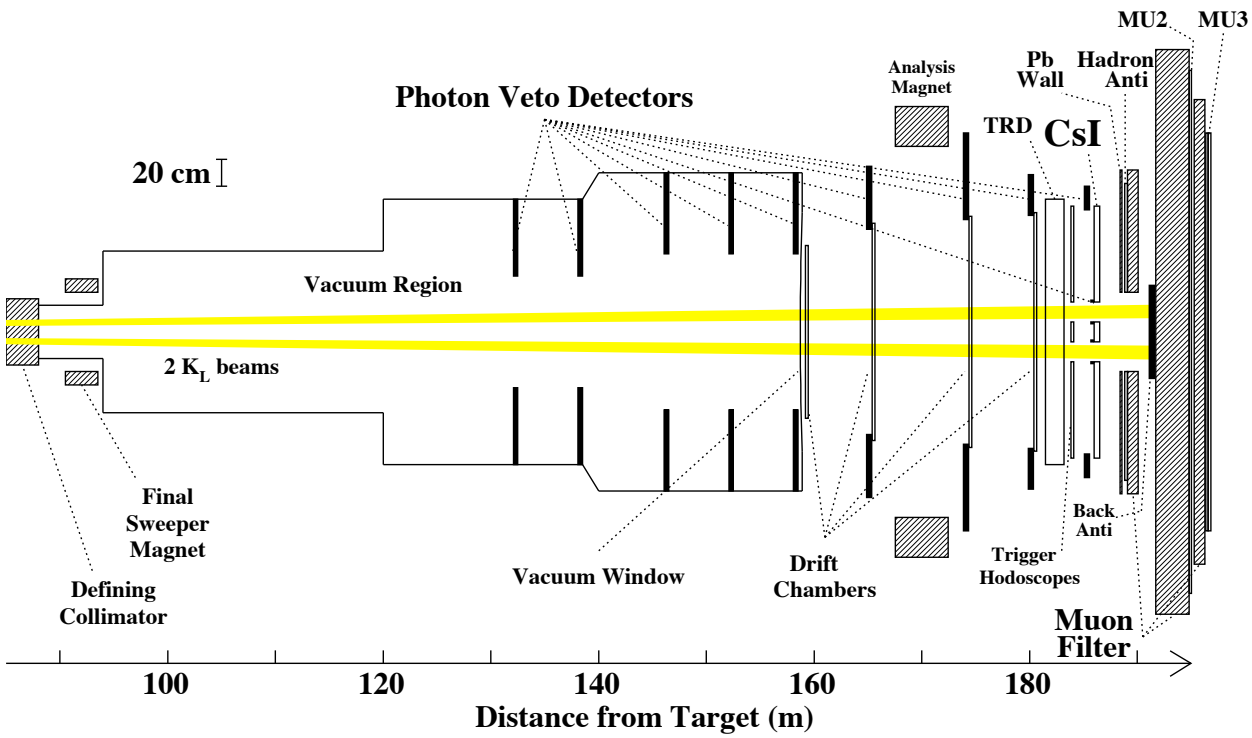

Figure 2.3: Plan view of the KTeV detector. The horizontal scale along the z direction is compressed.

number of drifting electrons were amplified near the wire and produced a pulse on the sense wire. The electron drift velocity was typically 50 μm/ns, and the maximum drift time across the cell was 150 ns. The analog signals from the chambers were amplified and discriminated. The discriminated signal was split between the trigger and Lecroy 3373 time-to-digital converter modules (TDC's) operated in a common stop mode. The incoming signal from the sense wire started the TDC counting and all running TDC's were stopped by a common signal from Level 1 trigger discussed in Sec. 2.5. A typical TDC time distribution is shown in Fig. 2.5. The in-time window is defined between 115 ns and 350 ns.

Each measured drift time t was converted into drift distance x with a nonlinear $x(t)$ map. The maps were measured separately for each of the sixteen planes using the uniform hit-illumination across each cell. The $x(t)$ calibrations were performed in the 1-2 day time periods between each magnet polarity reversal.

A charged-particle track produced a hit in each sense wire plane. The two x hits (or two y hits) in the staggered planes are referred to as a *hit-pair*. For a track that is perpendicular

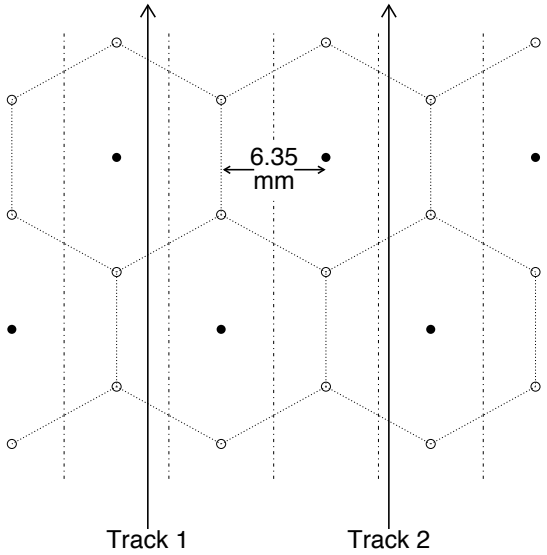

Figure 2.4: A hexagonal cell geometry of drift chamber showing six field wires (open circles) around each sense wire (solid dots).

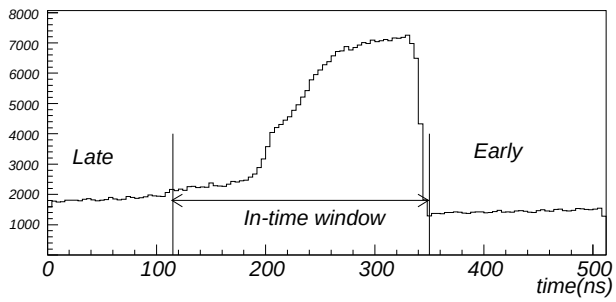

Figure 2.5: TDC time distribution of drift chamber. The in-time window is defined as 115 ns $< t <$ 350 ns. The sharp edge at 350 ns is short drift time near the sense wire.

to a drift chamber, the sum of drift distances (SOD) from each *hit-pair* is equal to the cell width of 6.35 mm. The measured SOD distribution is shown in Fig. 2.6. For inclined tracks, an angular correction is applied to the SOD. From the SOD distribution, the resolution of SOD is 150 μm, then the position resolution of each plane is estimated as 110 μm. The exact position resolution of each plane was monitored throughout the run.

After determination of trajectory by the spectrometer, the momentum p for each track was calculated based on the bending angle of the trajectory in the magnet. The momentum

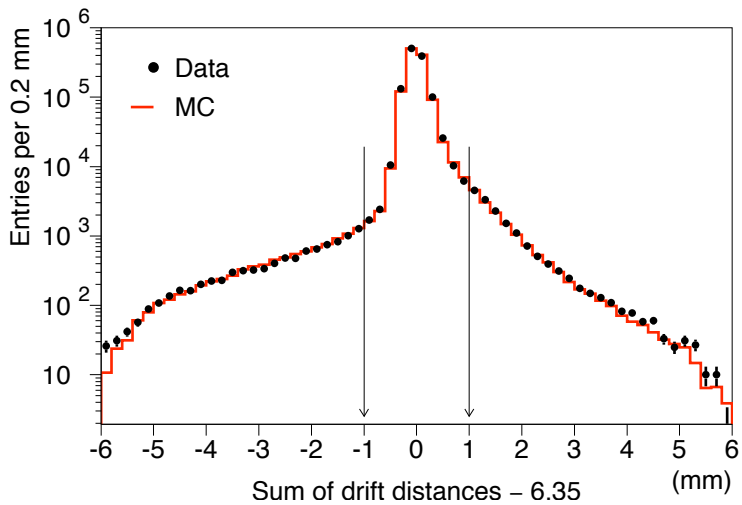

Figure 2.6: Deviation of the sum of drift distances (SOD) from the nominal cell size of 6.35 mm. The arrows indicate the ± 1 mm requirement for a good hit-pair. The data are shown as dots and the Monte Carlo prediction as a histogram.

resolution of the KTeV spectrometer was measured to be a quadratic sum,

$$\frac{\sigma_p}{p} = 0.016\% \times p \oplus 0.38\%, \tag{2.1}$$

where p is the momentum of a charged particle in GeV/c, and σ_p is its deviation. The constant term is due to a multiple scattering. The term linear in momentum is due to a finite position resolutions of the drift chambers, whose contribution becomes larger for tracks with smaller bending angle.

2.4.4 The Transition Radiation Detector

We used a set of transition radiation detectors (TRD's) located downstream of DC4, between z=181.2 m and 138.5 m, to distinguish electrons from pions.

The KTeV TRD system was composed of eight modules. Figure 2.7 shows a schematic view of a module. Each module consisted of a radiator composed of polypropylene fibers. The X-rays are emitted by transition radiation which occurs when a charged particle transverses a boundary of two media with different dielectric properties. These X-rays were detected by a Xe-filled, dual planed, multi-wire proportional counter (MWPC) located downstream of the radiator. The total yield of X-rays by transition radiation depends on the Lorentz factor, γ,

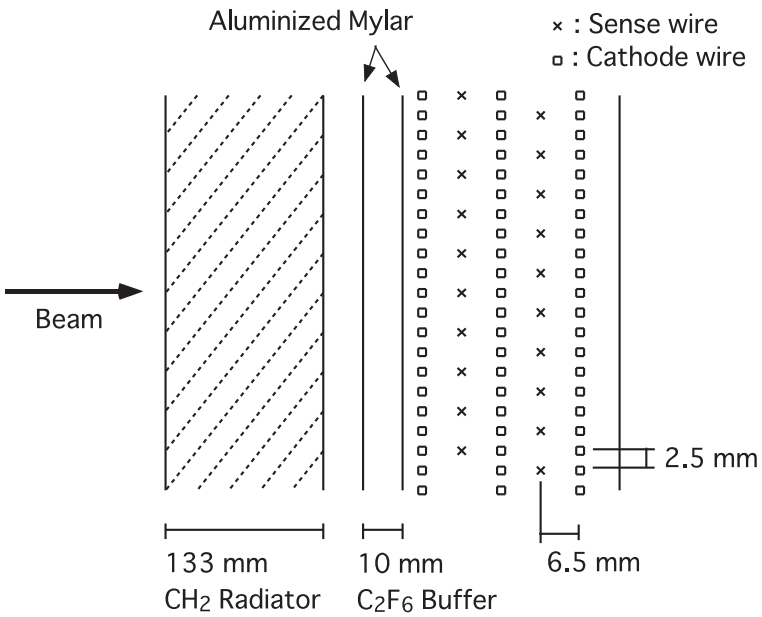

Figure 2.7: Plan view of one of the KTeV TRD modules.

of the particle. Therefore, there is a clear difference in the distribution of deposited energy in the sense plane between for electrons and for pions.

2.4.5 The Trigger Hodoscopes

In order to make trigger signals, the KTeV detector had two planes of scintillator hodoscopes (the Trigger Hodoscopes) downstream of the TRD's. The upstream scintillator plane is called V bank, and the downstream one is called V' bank. As shown in Fig. 2.8, each plane was composed of 31 scintillation counters with a 5 mm thickness, wrapped in a black sheet individually.

There were small gaps between the counters, representing 1.1% of the area of each scintillation plane, but the scintillators were made not to have overlapping gaps between the two planes. Each plane had two 14×14 cm^2 holes to allow the neutral beams to pass through.

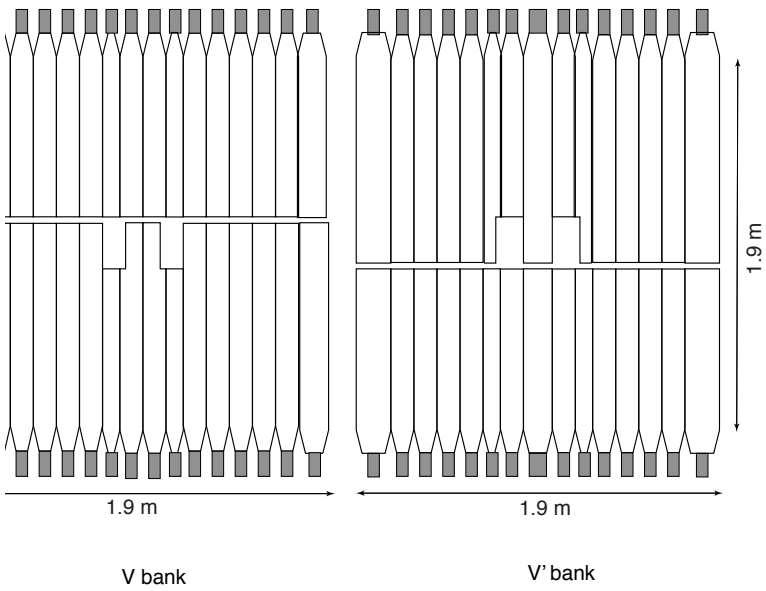

Figure 2.8: The V and V' trigger hodoscope planes. Both banks had dimensions of 1.9 m × 1.9 m and a thickness of 5 mm. There were no overlapping gaps between V and V' banks.

2.4.6 The CsI Calorimeter

The KTeV electromagnetic calorimeter consisted of 3100 pure cesium iodide (CsI) crystal as shown in Fig. 2.9.

There were 2232 2.5×2.5 cm^2 (small) crystals in the central region. Each crystal was viewed by a 1.9 cm diameter Hamamatsu R5364 photomultiplier tube (PMT). Outside this region, there were 868 5×5 cm^2 (large) crystals, each viewed by a 3.8 cm diameter Hamamatsu R5330 PMT. The transverse size of the calorimeter was 1.9×1.9 m^2 and the length of each crystal was 50 cm (27 radiation lengths). Two 15×15 cm^2 carbon fiber beam pipes allowed the few MHz of beam particles to pass through the calorimeter without striking any materials.

Digitizing electronics were placed directly behind the PMT's to minimize electronic noise ($<$ 1MeV). Each PMT was equipped with a custom made 8-range digitizer to integrate the charge delivered by the PMT. This device, digital PMT (DPMT) [12], had 16 bits of dynamic range with 8-bit resolution, and allowed the measurement of energies from a few MeV to 100 GeV. The digitization and readout operated at the Tevatron RF frequency of

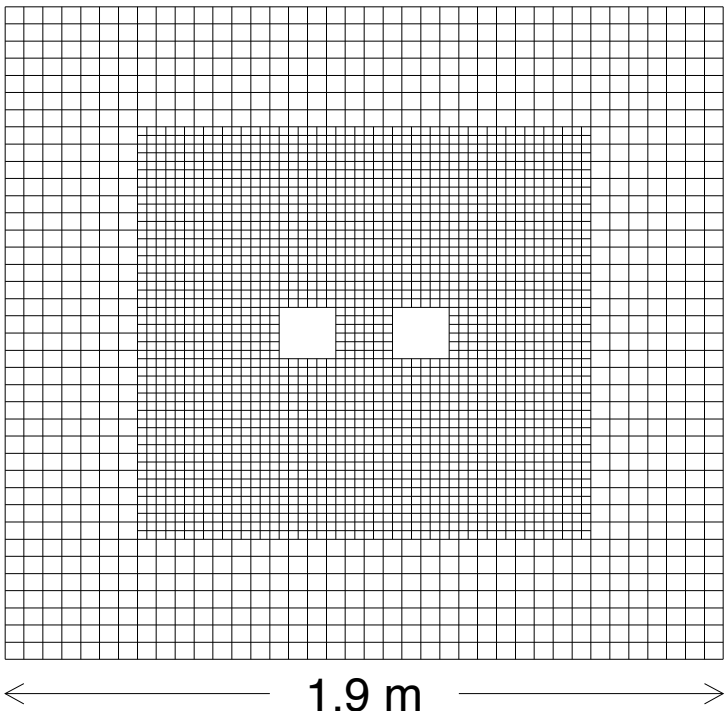

Figure 2.9: Beamline view of the KTeV CsI calorimeter, showing the 868 larger outer crystals and the 2232 smaller inner crystals. Each beam hole size is 15 $\times$ cm^2 and the two beam hole centers are separated by 0.3 m.

53 MHz, and PMT signal integration time was 114 ns (6 RF buckets), which permitted collection of approximately 96% of the fast scintillation component.

To first calibrate the response of each DPMT, a laser system was used. The energy scale of each channel was calibrated with momentum analyzed electrons from the $K_L \to \pi^{\pm} e^{\mp(}\bar{\nu}^{)}$ decays. The calibration constants were produced every 2-3 days with a precision of 0.03%. The electron energy was determined by summing the energies from a 3$\times$3 cluster of large crystals or a 7$\times$7 cluster of small crystals centered on the crystal with the maximum energy. The cluster energy was corrected for shower leakage outside the cluster region, leakage at the beam holes and calorimeter edges, and for channels with energies below the $\sim$4 MeV readout threshold.

Figure 2.10 shows the ratio of cluster energy measured in the calorimeter to the momentum measured in the spectrometer (E/p) for the electrons [13]. To avoid pion shower leakage into the electron shower, the $\pi^{\pm}$ was required to be at least 50 cm away from the $e^{\mp}$ on the

calorimeter.

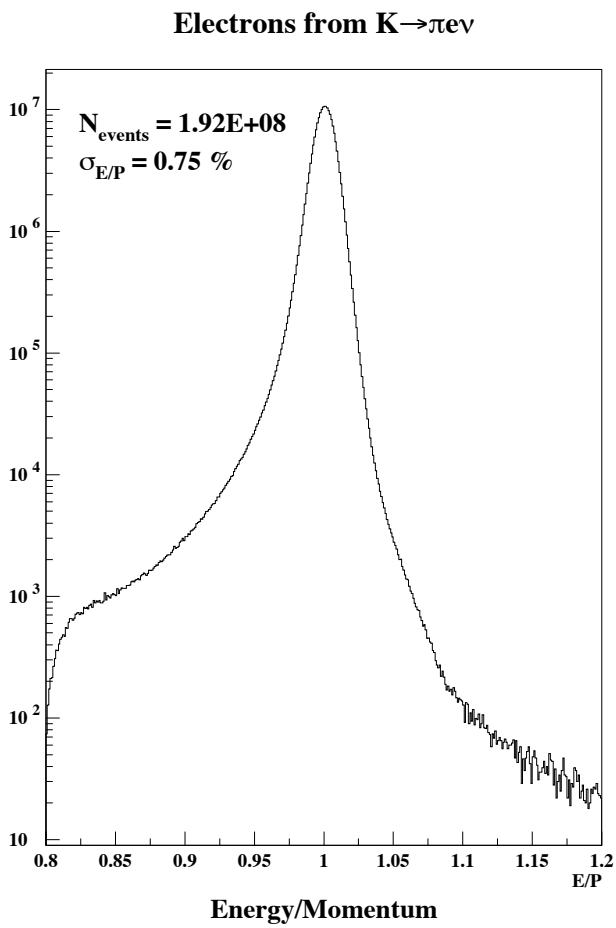

Figure 2.10: The ratio of calorimeter energy to track momentum, E/p, for electrons from $K_L \to \pi^{\pm} e^{\mp} \overset{(-)}{\nu}$ decays [13].

The Energy resolution of calorimeter was estimated by subtracting the momentum resolution from the E/p resolution. The energy resolution depending on the momentum is shown in Fig. 2.11, and parameterized as $\sigma_E/E = 2\%/\sqrt{E} \oplus 0.45\%$, where E is in GeV [13].

The cluster positions were determined from the fraction of energy in neighboring columns and rows. The conversion from energy fraction to position was done using a map based on a MC study using GEANT program [14]. The average position resolution for electrons was 1 mm for clusters in small crystals, and 1.8 mm for large crystals.

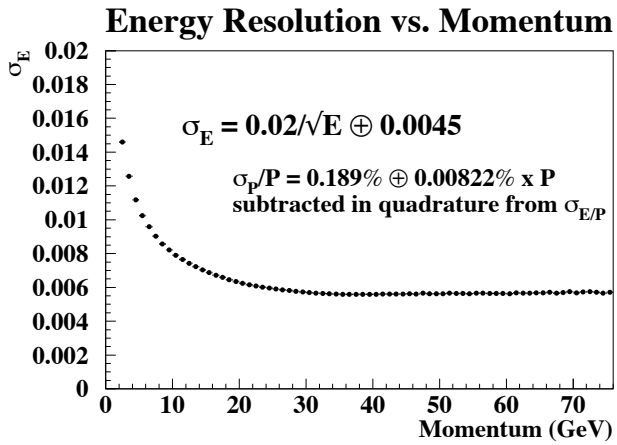

Figure 2.11: The resolution of the calorimeter as a function of energy, measured using electrons. The momentum resolution due to the spectrometer has been subtracted [13].

2.4.7 The Photon Veto System

The veto system was used in order to reduce trigger rates, to reduce backgrounds, and to define sharp apertures and edges that limit the detector acceptance.

Nine lead-scintillator ($16X_0$) photon veto counters were positioned along the beam-line. Five of them were located in the vacuum decay region (Ring Counters: RC6-RC10) and four were located in the spectrometer and calorimeter region (Spectrometer Antis: SA2-SA4, and CsI Anti: CIA). RC's, composed of 16 overlapping paddles ad a round outer perimeter to fit against the inner wall of vacuum tank, and a rectangular inner perimeter, as shown in Fig. 2.12,. SA's and CIA had also rectangular inner and outer perimeters. Another photon veto counter ($10X_0$) was placed at the end of the beam-holes (BA) to detect photons.

The CsI crystals around the beam-holes were partially covered by 8.7 X_0 tungsten-scintillator (Collar Anti: CA). This counter defined a sharp edge of the beam-holes. Consequently, the CA rejected events in which more than 10% of a cluster's energy was lost in a beam hole.

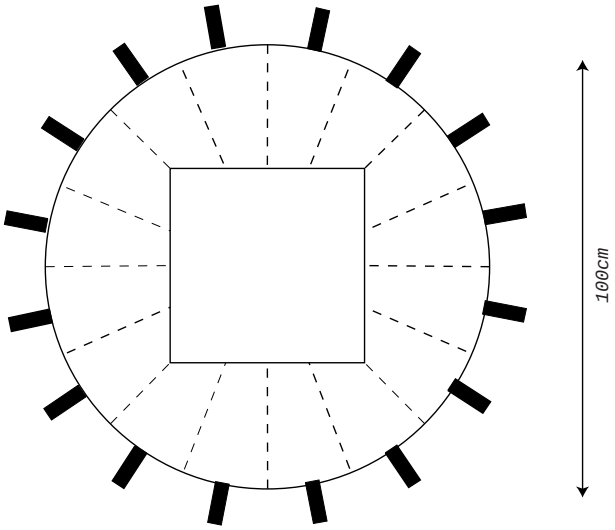

Figure 2.12: The schematic view of RC6, facing downstream. The beam passed through the inner aperture. The perimeter of outer circle fit right the vacuum pipe.

2.4.8 Hadron Anti

Following the CsI calorimeter, a 10 cm thick lead wall was located to obstruct any electromagnetic shower leakage out of the back of the calorimeter, and to induce the hadronic showers for detection by the hadron anti (HA). The HA was a single plane of 28 scintillator paddles, having a rectangular 2.24 m $\times$2.24 m outer perimeter and a 0.64 m $\times$ 0.34 m beam-hole. The HA was not used in this analysis.

2.4.9 The Muon System and Other Components

Muons with the momentum larger than 7 GeV/c were identified by detecting charged particles passing through 4 m of steel (24 nuclear interaction lengths) located downstream of BA. The probability that a hadronic shower from a 20 GeV/c pion leak through the steel was 1.4% [15]. There were two layers of 1 cm thick scintillator hodoscopes (MU2) without overlapping gaps at the downstream of the steel to veto muons.

2.5 Trigger system

KTeV had three levels of trigger system. The level 1 trigger (L1) made a decision every 19 ns (corresponding to the beam RF-structure) using fast signals from the detector. The events accepted by L1 were passed to the level 2 trigger (L2). L2 was based on more sophisticated processors.When an event passed L2, the entire detector was read out with an averaged dead time of 15 μs. Each event was then sent to one of twenty-four 200-MHz SGI processors running a level 3 (L3) software filter. Events passing L3 were written to a Digital Linear Tape. An independent set of ten 150-MHz processors was used for online monitoring and calibration.

The trigger elements used for the $K_L \to \pi^{\pm} e^{\mp(}\bar{\nu}^{)} e^{+} e^{-}$ analysis, the 4-track triggers, are listed in Table .2.2, and we will explain them in succeeding subsections.

2.5.1 Level 1 Requirements

At L1, the 4-track trigger vetoed events with particles leaving fiducial volume of the detector and events with muons which pass through the muon filters. The 4-track trigger also required that there were enough hits in the drift chambers and trigger hodoscopes, and the total energy deposited in the calorimeter was larger than 11 GeV. The individual elements required in L1 are the followings :

- Beam timing (GATE)

  This trigger element is turned on when the proton beam is being delivered to the KTeV target.

- Trigger hodoscope (3V_TIGHT)

  This trigger element requires at least three scintillators are hit in V bank and three scintillators are hit in V' bank of the trigger hodoscopes.

- Drift chamber 1 and 2 (2DC12_MED)

The first signal from a drift chamber was less than 100 ns after a charged particle goes through a drift chamber, because the particle must go through two adjacent sense wire planes. We used such signals from DC1 and DC2 for a fast trigger source. The sense wires in both x- and y-views of the drift chambers were grouped in the "paddles". A "paddle" spanned 16 wires (8 wires in each of the adjacent planes) of the chamber view. 2DC12_MED required that at least two paddles were hit in three out of four available views. The fourth view was required to have at least one paddle hit.

- Total energy on the calorimeter (ET_THR1)

  The analog signals from all the calorimeter photomultipliers were summed to be used as the total in-time energy deposited in the entire CsI calorimeter. ET_THR1 required that this total energy to be higher than 11 GeV.

- Muon veto (!MU2)

  Our signal mode and normalization mode do not include any muons. Therefore, with !MU2, we vetoed any events that hit the MU2 veto counter.

- Photon veto (PHBAR1 and !CA)

  PHBAR1 trigger element vetoed events with $\geq$ 500 MeV energy deposit in the ring counters (RC6-10), or $\geq$ 400 MeV energy deposit in the spectrometer antis (SA2-4). !CA vetoed events with $\geq$ 14 MeV energy deposit in the collar antis.

2.5.2 Level 2 Requirements

The elements of the L2 utilized hardware processors to analyze the topology of an event and reduced the event rate to approximately 10 kHz. The events were read out only if all the required L2 processors accepted the events. There were following level 2 trigger elements.

- Drift chamber activity (34_HCY)

  The signals from the drift chambers were analyzed by the sophisticated hit-counting system called 34_HCY. The system verified hit timing information and counted the number of *in-time hit pairs* of complementary wires (see Sec. 2.4.3) in each chamber.

Considering the isolated in-time hit, N sequential in-time hit wires in a plane were counted as $N-1$ *in-time hit pairs* (see Fig. 2.13). The 34_HCY required at least three *in-time hit pairs* in y-view of each upstream drift chamber, DC1 and DC2, and at least four *in-time hit pairs* in y-view of each downstream drift chambers, DC3 and DC4.

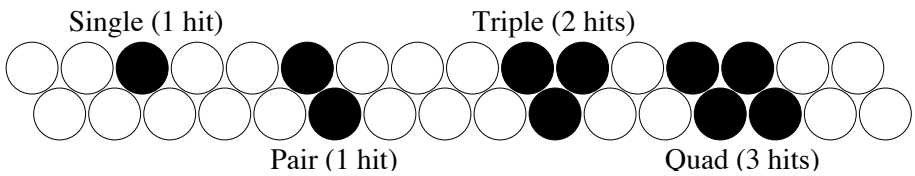

Figure 2.13: Possible wire hit patterns in a drift chamber plane pair, and the corresponding 'in-time hit pair' counts.

- Sum of distance correlation (3HC2X)

  This DC Hit Counters required additional condition for chamber timing. Using flash TDCs, the SOD (see Fig. 2.6 from a hit pair was required to be within 1 mm of the cell width (6.35 mm) to be recognized as an in-time hit pair. 3HC2X required that at least three such hits in the x-view of DC2.

- Y Track Finder (YTF_UDO)

  The function of Y Track Finder (YTF) [16] trigger made a simple y track reconstruction by looking at the hit-patterns in the drift chamber, using the fact that y tracks do not cross $y = 0$ within the chamber system. For the momentum balance, we required the tracks in both upper and lower halves of chambers. YTF_UDO required simultaneous one upper and one lower half good tracks, or one central track, or that the hit-counting system had not finished counting yet.

- Hardware cluster counter (HCC_GE2)

  The hardware cluster counter (HCC) counted the number of in-time clusters in the CsI calorimeter, which consisted of block with the deposit energy greater than 1 GeV. The logic to count the hardware cluster is discussed in [17]. HCC_GE2 required two or more such hardware clusters on the calorimeter.

Table 2.2: The E799 4-track trigger elements.

Element	Trigger level	Description
3V_TIGHT	1	$\geq$ 3 hits in both V and V' banks.
2DC12_MED	1	3 out of 4 DC1 and DC2 planes with $\geq$ 2 hits and 1 plane with $\geq$ 1 hit.
ET_THR1	1	Total energy in CsI $\geq$ 11 GeV.
!MU2	1	To veto events with $\geq$ 1 hit (15 mV, 0.2 mip) in MU2.
PHBAR1	1	To veto events with $\geq$ 0.5 GeV in the ring counters (CAs) or events with $\geq$ 0.4 GeV in the Spectrometer antis (SAs).
!CA	1	To veto events with $\geq$ 14 GeV in the collar antis (CAs).
34_HCY	2	$\geq$ 3 hits in DC1Y, $\geq$ 3 hits in DC2Y and $\geq$ 4 hits in DC3Y, $\geq$ 4 hits in DC4Y.
3HC2X	2	$\geq$ 3 hits in DC2X.
YTF_UDO	2	Simultaneous upper and lower half good track or central good track.
HCC_GE2	2	$\geq$ 2 hardware clusters.

2.5.3 Level 3 Requirements

The level 3 trigger is a software filter. For our study, L3 required three reconstructed tracks from a common vertex. The reconstruction technique will be discussed in Sec. 3.1, because that technique was also used in offline analysis.

2.6 Monte Calro simulation

The Monte Carlo simulation (MC) consisted of three main steps. The first step was kaon generation at the BeO target and propagation along the beamline to a decay point. The second step was kaon decay into an appropriate final state, and tracing of the decay products through the detector. The last step was to simulate the detector response including digitization of the detector signals. The simulated event format and analysis were the same as the data.

2.6.1 K^0 and $\bar{K^0}$ production and decay

The kaon energy spectrum and the relative flux of K^0 and $\bar{K^0}$ states produced at the target were based on a parameterization, [18].

The differential cross section was parameterized as a function of kaon momentum and its transverse momentum respect to the incoming protons, in the laboratory frame. The z position of each kaon decay was chosen based on the calculated z distribution for the initial K^0 or $\bar{K^0}$ state, and accounted for on interference between K_L and K_S.

If the kaon trajectory intersected the primary beam collimator, tracing was terminated, and a new kaon was generated. Kaons striking the defining collimator was either terminated or allowed to scatter. Scattering was also simulated though the beam absorbers shown in Fig. 2.1.

In the Monte Carlo, kaons were generated in a momentum range between 15 and 225 GeV/c, and over a decay range between 90 and 160 m downstream of the target. Consequently, except for very high energy kaons, the contribution of K_S is negligible within the allowed decay region. The detector acceptance for decays outside of these ranges was negligible.

The kaon energy distribution was tuned by two steps. In first step, the kaon energy distribution of MC was tuned to match $K_L \to \pi^+\pi^-$ data acquired by KTeV E832 experiment, then some changes due to differences between E832 experiment and E799 experiment were added to MC for E799 analysis. After these treating on MC for E799, a slope of fitted linear line to data-MC ratio was appeared for the $K_L \to \pi^+\pi^-\pi^0_D$ data acquired by E799 experiment, $(-3.39 \pm 0.86) \times 10^{-4}$/GeV. Therefore, as the second step, the kaon energy distribution was weighted by this slope of linear line.

2.6.2 $K_L \to \pi^\pm e^{\mp(}\bar{\nu}^{)} e^+ e^-$ decay generator

The $K_L \to \pi^\pm e^{\mp(}\bar{\nu}^{)} e^+ e^-$ decay was generated in two steps. First, events were generated according to a flat phase space (see Appendix B. For each events, the matrix element was

calculated for its kinematic variables, and events were selected to statistically follow the differential cross sections calculated from the matrix elements.

The absolute square of matrix element of $K_L \to \pi^{\pm} e^{\mp(}\bar{\nu}^{)} e^+ e^-$ decay with the next to leading order was calculated by the routine created by Tsuji [7].

We also simulated an additional inner bremsstrahlung from the electrons and pions using PHOTOS program. [19, 20] The real photon radiation by this process is discussed in Sec. 4.3.

2.6.3 Other decay generators for normalization and backgrounds

The generators for other decays were created and used by KTeV collaboration. We briefly explain those generators.

$K_L \to \pi^+\pi^-\pi^0_D$, $K_L \to \pi^+\pi^-\pi^0_{4e}$, and $K_L \to \pi^+\pi^-\pi^0_{\gamma\gamma}$ decays generator

For the $K_L \to \pi^+\pi^-\pi^0$ decay, we used the matrix element:

$$|\mathcal{M}|^2 \propto 1 + gu + hu^2 + jv + kv^2, \tag{2.2}$$

where

$$u = \frac{s_3 - s_0}{M_\pi^2}, \qquad v = \frac{s_1 - s_2}{M_\pi^2}, \tag{2.3}$$

and

$$s_i = (P_K - P_i)^2, \qquad s_0 = \frac{1}{3}\sum_{i=1}^{3} s_i, \tag{2.4}$$

P_K and P_i are the four-momenta of the kaon and the three pions, respectively. The values of g, h, and k in this analysis were taken from the KTeV analysis of $K_L \to \pi^+\pi^-\pi^0$ decay by Barrio [21]. The coefficient j is related to CP-violating effects, and was fixed at zero.

Because the lifetime of the neutral pion is short, we assumed that the π^0 promptly decays at the same position as the parent kaon decay. For the $K_L \to \pi^+\pi^-\pi^0_D$ decay, π^0's were forced to decay into $\pi^0 \to e^+e^-\gamma$ or $\pi^0 \to e^+e^-\gamma\gamma$. The first order virtual radiative corrections were applied to the generator, and the $\pi^0 \to e^+e^-\gamma\gamma$ events were generated with the invariant mass of two-photon system above 1 MeV [22].

To generate the $K_L \to \pi^+\pi^-\pi^0_{4e}$ decays, the neutral pions were forced to decay into four electrons. The matrix element of the $\pi^0 \to e^+e^-e^+e^-$ decay was calculated using the complete lowest-order QED amplitudes ([23], Caution that there are many errors in this paper.).

To generate the $K_L \to \pi^+\pi^-\pi^0_{\gamma\gamma}$ decays, the neutral pions were forced to decay into two photons with a simple two body phase space.

$K_L \to \pi^\pm e^{\mp(}\bar{\nu}^{)}\gamma$ decay generator and photon conversion in detector

We generated both the $K_L \to \pi^\pm e^{\mp(}\bar{\nu}^{)}$ and $K_L \to \pi^\pm e^{\mp(}\bar{\nu}^{)}\gamma$ events. The decay rate of the $K_L \to \pi^\pm e^{\mp(}\bar{\nu}^{)}\gamma$ relative to the $K_L \to \pi^\pm e^{\mp(}\bar{\nu}^{)}$ decay was derived from the NA31 result [24]. The $K_L \to \pi^\pm e^{\mp(}\bar{\nu}^{)}\gamma$ events were generated using the soft photon theorem and the current algebra technique by Fearing *et. al.*, [5].

$K_L \to \pi^\pm e^\mp \nu \pi^0_D$ decay generator

The generator for $K_L \to \pi^\pm e^\mp \nu \pi^0$ used its form factor defined in [25] for the decay $K^+ \to \pi^\pm e^\mp \nu \pi^+$ and measured for $K_L \to \pi^\pm e^\mp \nu \pi^0$ in the experiment E731, precedent experiment of KTeV [26]. Neutral pions were forced to decay into the $\pi^0 \to e^+e^-\gamma$.

2.6.4 MC for tracing of decay products

After a kaon decay was generated, the decay products were boosted to the lab frame and traced through the detector. Charged pions were allowed to decay into $\mu\nu$ in flight.

2.6.5 MC for detector responses

In the MC, charged particles passing through the detector materials received multiple scatterings according to a parameterization of the Molière theory [27]. This also accounted for a non-Gaussian tail in the scattering angle distribution caused by the single scattering. For

electrons, in addition to the scattering, radiative bremsstrahlung was allowed to happen according to the Bethe-Heitler cross-section. A photon can be converted in materials with a probability, $1 - \exp^{-\frac{7}{9}(X/X_0)}$, where X/X_0 is the amount of the material measured in radiation lengths [1]. The energy spectrum of the converted e^+e^- pair was defined by Bethe-Heitler formula. The routines in EGS4 electromagnetic shower library [28] was imported to define the opening angle of the e^+e^- pair.

Particles generated in these interactions were also traced as well as daughter particles of the decay.

Particles were not traced after they escaped from the fiducial volume of the detector.

Photon veto

The energy deposits in photon veto were smeared with Gaussian distribution. The parameters of the energy deposit distribution were determined with calibration constants acquired in the calibration runs. When charged particles except for electrons passed through photon veto counters, they were treated as minimum ionizing particles and were scattered there.

For electrons and photons, the particles were stopped when they entered a photon veto, and all of their energies were deposited in the detector after Gaussian smearing.

A trigger was vetoed, if the total energy deposit in one of the photon veto counters exceeded its veto threshold. The energy deposit was digitized to ADC counts based on the gain determined in calibration runs.

Drift chamber

The Monte Carlo simulation traced each charged particle through the drift chambers, and the hit position at each drift chamber plane was converted into a TDC value. The position

[1] For the $K_L \to \pi^{\pm} e^{\mp(}\bar{\nu}^{)} \gamma$ decay and the $K_L \to \pi^+\pi^-\pi^0_{\gamma\gamma}$ decay, the conversion probability of photon was increased by a factor 10, and then the number of conversion events were scaled to have default conversion ratio.

resolutions measured in data were used to smear the hit positions, and the inverse of the $x(t)$ map was used to convert the smeared hit position into a drift time.

The detection inefficiencies studied with data were included in the simulation [8].

TRD

TRD responses were simulated using the data base of calibration constants which gives the simulated ADC readout of the transition radiation as the function of a TRD plane, a cross section regions and a particle type passing through. The calibration were obtained as the wire-by-wire gain by $\pi^{\pm}$s found in the $K_L \to \pi^{\pm} e^{\mp(}\bar{\nu})$ decays.

Particle propagations in the TRD were simulated as that the particle passed through 0.14 X_0 amount of material and 0.04 X_0 for the beam region. The multiple scattering by the TRD wires and the photon conversion in the TRD were simulated.

The ratio of lost pions by the π-hadron interaction was investigated using *GEANT* [14]. The ratio was translated into a function of the pion energy, E_π and the path length in the TRD, L_{path}:

$$\delta(\pi) = [I \exp(-E_\pi/\lambda) + C] L_{\text{path}}, \tag{2.5}$$

where I, λ, and C are fitting parameters. Every pion in MC is weighted by $1-\delta(\pi)$. Seeking this function will be discussed in Appendix C.

CsI calorimeter

When a particle hit the calorimeter, the MC generated an energy deposit in each crystal. The MC also simulated the energy leakage around the beam-holes and at the outer edges of the calorimeter. The energy sharing by two or more clusters also can be an aim to study by MC.. A large sample of *GEANT*-based [14] electron and photon showers were used to simulate electromagnetic showers in the calorimeter. The shower samples were generated with electron or photon incident on the central crystal of a 13×13 array of small crystals (32.5×32.5 cm^2). The showers were generated in 6 energy bins from 2 to 64 GeV, and in x

and y position bins. The position bin spacing varied from 7 mm at the crystal center, to 2 mm at the edge. This binning matched the variation in reconstructed position resolution, which was better for particles incident near the edge of a crystal. Outside the 13×13 array, a *GEANT*-based shower shape parameterization was used. This parameterization modeled energy deposits in a 27×27 array. Energy leakage across the beam holes was modeled based on electron data from $K_L \to \pi^{\pm} e^{\mp(} \bar{\nu}^{)}$ decays.

To simulate the DPMT response, the energy deposit in each crystal was distributed among six consecutive RF buckets according to the measured time profile of the scintillation light output. In each 19 ns wide RF bucket, the energy was smeared to account for photo-statistics, and random activity from an accidental trigger was added. Each channel was digitized using the calibration constants obtained from data. Thus a DPMT response was started, if the digitized signal exceeded the 4 MeV readout threshold that was applied during data-taking.

In addition to simulating electromagnetic showers, we also simulated calorimeter response to charged pions and muons. The energy deposits from charged pions were based on a library of *GEANT*-based showers using a 50×50 array of small crystals. A continuous energy distribution was generated in x, y position bins with 4 mm separation. For muons, the energy deposit was simulated using the Bethe-Block energy loss formula with the average of 320 MeV.

Chapter 3

Analysis

We have collected 70 million events that passed the 4-track triggers. In this chapter, we will select $K_L \to \pi^{\pm} e^{\mp(}\bar{\nu}^{)} e^{+} e^{-}$ decays by reconstructing four well-measured tracks in the spectrometer, and reduce the number of backgrounds events with particle identification and kinematic requirements. In Section 3.1 We first explain the reconstruction, including tracking, vertexing and particle identification. In Section 3.2, we discuss the backgrounds and add some more requirements to reduce the backgrounds. In Section 3.3, we give a summary for the $K_L \to \pi^{\pm} e^{\mp(}\bar{\nu}^{)} e^{+} e^{-}$ analysis. To determine the branching fraction of $K_L \to \pi^{\pm} e^{\mp(}\bar{\nu}^{)} e^{+} e^{-}$ decay, and to estimate the number of background events in data, the total number of kaon decays, kaon flux, is required. In Section 3.4, the normalization mode analysis to estimate the kaon flux is described.

3.1 Event reconstruction and selection

3.1.1 The clustering, tracking, and vertexing

In the CsI calorimeter, the cluster energy was defined as a sum of energy deposits in a 7×7 array of small crystals or 3×3 array of large crystals centered on a crystal with the local maximum deposit energy, which is called *seed crystal*. Energy clusters in the CsI calorimeter were classified into two categories, *hardware cluster* and *software cluster*. The only difference was the determination of the seed crystal in the cluster. The hardware

cluster was formed around a seed crystal with the energy > 1 GeV that was counted by the HCC (see Sec. 2.5.2). The software cluster used crystals with a deposit energy of > 0.1 GeV thate were not used by the HCC. The software cluster was required to have the total energy of 0.25 GeV or more.

A sequence of corrections were made to these cluster energies. These processes included the cluster overlap correction, boundary correction between small and large crystal region, and the missing crystal correction around the beam holes and outer perimeter.

In order to determine the x position of the cluster, the sum of energies in the central column and adjacent columns were calculated. The energy ratio between the adjacent column with larger energy and the central column and the central column was used to get the cluster position within the central crystal, by looking up a table generated with GEANT. The y position was determined in the same way by using the energy sum in rows.

The event reconstruction in spectrometer began by finding tracks in y view (y-tracks), using the four drift chambers. Because we allowed two tracks to share one y-track, at least two y-tracks were required for an event. In the x-view, four separate segments were required upstream of the magnet using DC1 and DC2, and downstream of the magnet using DC3 and DC4. The extrapolated upstream and downstream x-track segments typically matched to within 0.5 mm at the center of the magnet. We call the distance between the segments at the center of magnet as X_{offmag}. To allow for multiple-scattering and magnetic fringe field between the drift chambers, only a loose match of 6 mm was required at the magnet.

To determine the full trajectory, the x and y tracks were matched each other by requiring the tracks to match the CsI clusters within 7 cm.

Before the vertexing, each track position was applied detail corrections, and the position resolution was determined based on the quality of the hit-pair and the multiple scattering, in DC1 and DC2.

We defined the z of the decay vertex as the position in z where four tracks came closest to

each other in the x-y plane at the z-position. To be more precise, projected position of i-th track, (x_i, y_i), was calculated for a given z. We defined a vertex χ^2 as:

$$\chi^2_{vtx} \equiv \sum_i (\Delta x_i/\sigma_{\Delta x_i})^2 + \sum_i (\Delta y_i/\sigma_{\Delta y_i})^2, \tag{3.1}$$

where Δx_i (Δy_i) was the distance of x_i (y_i) from the weighted average of x_i's (y_i's), and $\sigma_{\Delta x_i}$ ($\sigma_{\Delta y_i}$) was the resolution of Δx_i (Δy_i) at z, which was calculated based on the position resolutions of the chambers and the effect of multiple scattering. The wights to require the weighted average of x_i's (y_i's) were the inverses of Δx_i's (Δy_i's). The z-position that gave the smallest χ^2_{vtx} was defined as the z of the decay vertex, and the weighted average of x_i's and y_i's were defined to be x- and y-position of the decay vertex. At last, the tracks were adjusted to originate from the vertex. The 4-momentum of each track is determined by using this trajectory.

The χ^2_{vtx} was required to be less than 125. This requirement is loose to remain insensitive to the tails in the multiple scattering distribution.

Selection criteria introduced in this subsection:

- $X_{offmag} < 6$ mm,
- Cluster-track matching < 7 cm, and
- $\chi^2_{vtx} < 125$.

3.1.2 The particle identification

. To identify the particles, the ratio of cluster energy measured in the CsI calorimeter to momentum measured in the spectrometer (E/p) was used. Figure 3.1 shows the E/p distributions for pions and electrons.

We required $E/p < 0.9$ for pion tracks and $0.93 < E/p < 1.15$ for electron tracks. With these criteria, 0.81% of pions and 1.84% of electrons were lost in data. We also used the transition radiation detector (TRD) for π-e identification. A parameter to indicate the likelihood of pion by TRD for the track were defined as $Prob_\pi$ (see Appendix D). We

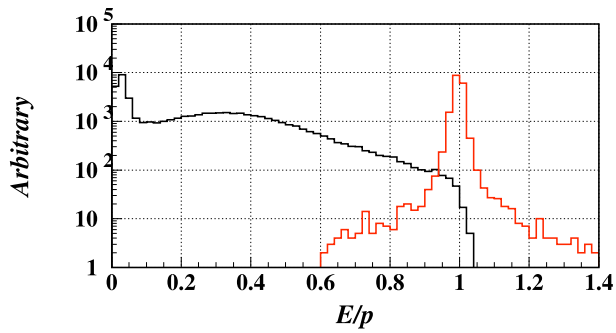

Figure 3.1: The ratio of cluster energy measured in the CsI calorimeter to momentum measured in the spectrometer (E/p). Black histogram: for pion candidates selected from the data collected as the $K_L \to \pi^+\pi^-\pi^0_{\gamma\gamma}$ decay without a cut on E/p. Red histogram: for electron candidates selected from the data collected as the $K_L \to \pi^+\pi^-\pi^0_D$ decay with a loose cut on E/p for electron.

required $Prob_\pi < 0.06$ for only tracks identified as electrons by E/p. With these criteria, 7.9% of pions were lost in data.

Differences in the detection efficiency between data and MC have to be taken into account. The ratios of the efficiencies, $1 + \delta_{i,j} = \epsilon_{data\ i,j}/\epsilon_{MC\ i,j}$ are listed in Table 3.1. The details of the estimation are described in Appendix E.

Table 3.1: Correction factors for particle identifications. Errors are only statistical.

Correction factor	Value
$\delta_{\mathrm{e},E/p}$	$(3.4 \pm 0.9) \times 10^{-3}$,
$\delta_{\pi,E/p}$	$(2.43 \pm 0.27) \times 10^{-3}$, and
$\delta_{\mathrm{e,TRD}}$	$(3.5 \pm 0.6) \times 10^{-3}$.

If two tracks cross with each other in the x-view of TRD, the hits overlap, and radiations from these tracks cannot be distinguished from each other. To reject such a case, the events were required not to have any crossing tracks within TRD in the x-view.

In order to reject muons identified as pions, we required the energy of pion candidate to be greater than 10 GeV. This was to ensure that if they were the muons, they would penetrate the 25 nuclear interaction lengths of the muon filter (The muons with energy larger than 7 GeV can penetrate 31 nuclear interaction lengths muon filter [15]).

Selection criteria introduced in this subsection:

- $E/p < 0.9$ for pion tracks,
- $0.93 < E/p < 1.15$ for electron tracks,
- $E_\pi > 10$ GeV,
- TRD $Prob_\pi < 0.06$ for electron candidate tracks, and
- No crossing tracks in the x view within TRD.

3.1.3 Cuts on the kaon energy, the squared longitudinal momentum of neutrino in the kaon rest frame, and the Z-vertex

In a general full reconstruction analysis, the kaon energy is the total sum of energies of all the decay particles. However, in the $K_L \to \pi^\pm e^{\mp(}\bar{\nu}^{)} e^+ e^-$ analysis, since the neutrino is unobservable, the reconstructed kaon energy has two-fold ambiguity, a maximum solution and a minimum solution ($E_K$max and $E_K$min). The maximum and minimum solution of kaon energy are calculated using the following kinematic observables:

- The energy of $\pi^\pm e^\mp e^+ e^-$ system in the kaon rest frame: $E^*_{\pi eee}$,
- The longitudinal momentum of $\pi^\pm e^\mp e^+ e^-$ system in the kaon rest frame: $P^*_{\pi eee||}$,
- The energy of $\pi^\pm e^\mp e^+ e^-$ system in the laboratory frame: $E_{\pi eee}$, and
- The longitudinal momentum of $\pi^\pm e^\mp e^+ e^-$ system in the laboratory frame: $P_{\pi eee||}$.

The observables in kaon rest frame, $E^*_{\pi eee}$ and $P^*_{\pi eee||}$, are:

$$E^*_{\pi eee} = \frac{m_K^2 + m_{\pi eee}^2}{2m_K} \tag{3.2}$$

$$P^*_{\pi eee||} = \sqrt{\frac{(m_K^2 - m_{\pi eee}^2)^2 - 4m_K^2 p_t^2}{4m_K}}, \tag{3.3}$$

where m_K is kaon mass, $m_{\pi eee}$ is the invariant mass of all the observed track system, i.e., $\pi^\pm e^\mp e^+ e^-$ system, and p_t^2 is the transverse momentum of $\pi^\pm e^\mp e^+ e^-$ system.

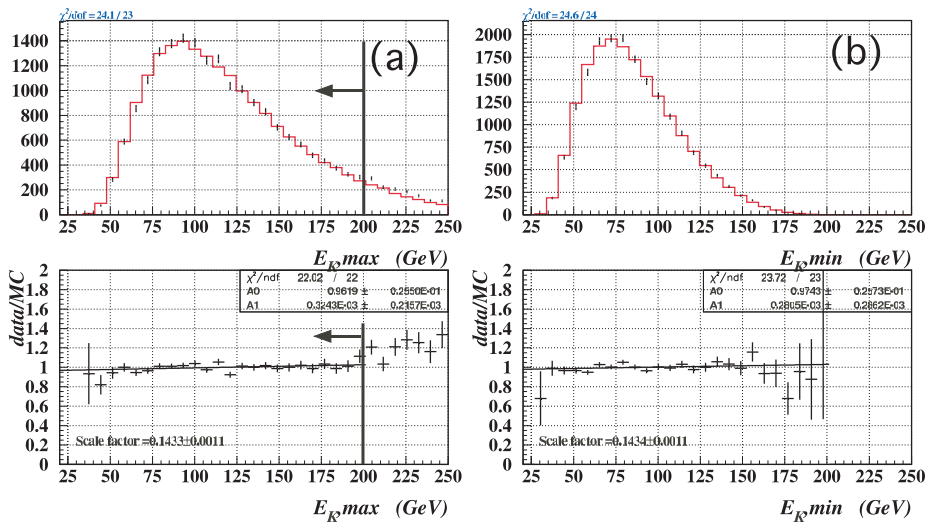

Figure 3.2: Data (dots) and MC (histogram) comparison of the distributions of kaon energy, (a) $E_k max$, and (b) $E_k min$, of $K_L \to \pi^{\pm} e^{\mp} \overset{(-)}{\nu} e^+ e^-$ decays. The MC includes signal and background events. Both MC and data were collected with the final selection cuts listed in Table 3.2 except for the cut on the relevant distribution. For each distribution, the data-to-MC ratios shown below are fit to a straight line. There are good agreements between data and MC. The vertical line and arrow show the accepted regions for $K_L \to \pi^{\pm} e^{\mp} \overset{(-)}{\nu} e^+ e^-$ candidates ($E_K$max < 200 GeV) .

The Lorentz transformation parameter, β, can be obtained as two solutions:

$$\beta_{\pm} = -\frac{(E^*_{\pi eee} \pm P^*_{\pi eee||})^2 - (E_{\pi eee} + P_{\pi eee||})^2}{(E^*_{\pi eee} \pm P^*_{\pi eee||})^2 + (E_{\pi eee} + P_{\pi eee||})^2}, \tag{3.4}$$

where $+$ and $-$ correspond to the neutrino going upstream and downstream, respectively, in the kaon rest frame. Consequently, the maximum (minimum) solution of kaon energy is:

$$E_K max(min) = m_K / \sqrt{1 - \beta^2_{-(+)}}. \tag{3.5}$$

Figure 3.2 shows the data-MC [NLO(p^4)] comparisons of $E_k$max(min) spectra for $K_L \to \pi^{\pm} e^{\mp} \overset{(-)}{\nu} e^+ e^-$. There are good agreements between data and MC. We required $E_K$max $<$ 200 GeV to avoid simultaneous two $K_L \to \pi^{\pm} e^{\mp} \overset{(-)}{\nu}$ decays and K_S decay.

The $P^*_{\pi eee||}$ has the same magnitude as the longitudinal momentum of neutrino in the kaon rest frame, $P^*_{\nu||}$. The squared longitudinal momentum of neutrino in the kaon rest frame, $P^{*2}_{\nu||} = P^{*2}_{\pi eee||}$, is often investigated for the study of $K_L \to \pi^{\pm} e^{\mp} \overset{(-)}{\nu}$.

Figure 3.10 shows the distribution of $P^{*2}_{\nu||}$. There is a good agreement between data and MC. We required $P^{*2}_{\nu||} > 0$, because negative $P^{*2}_{\nu||}$ is unphysical for the signal decay mode.

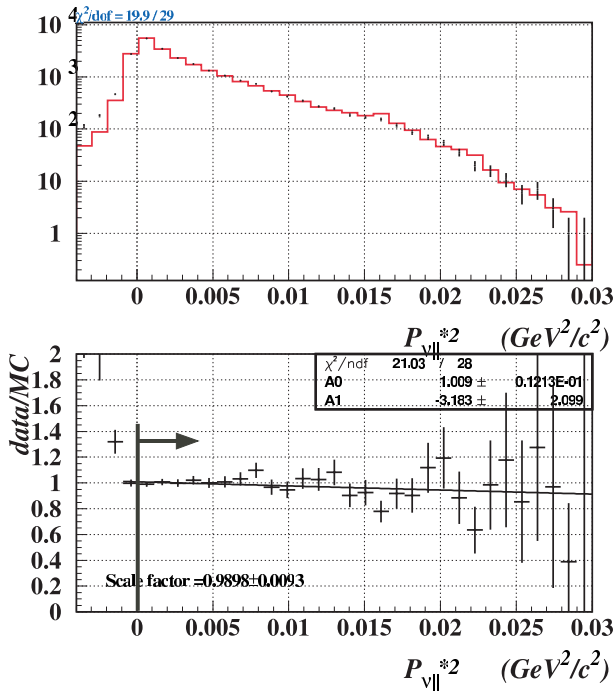

Figure 3.3: Comparison of the distributions of $P^{*2}_{\nu||}$ for data (dots) and MC (histogram). The MC includes signal and background events. Both MC and data were collected with the final selection cuts listed in Table 3.2 except for the cut on $P^{*2}_{\nu||}$ distribution. The data-to-MC ratios on the bottom are fit to a straight line. The vertical line and arrow show the accepted region for $K_L \to \pi^{\pm} e^{\mp} \overset{(-)}{\nu} e^{+} e^{-}$ candidates ($P^{*2}_{\nu||}$ GeV^2/c^2).

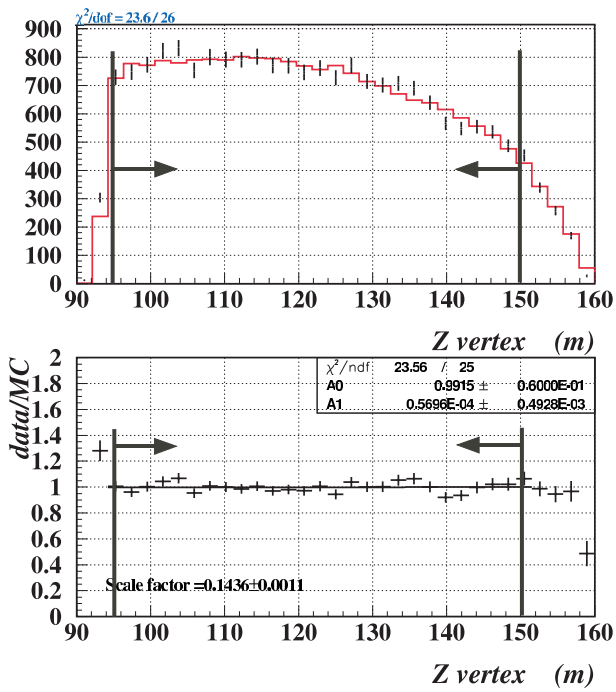

Figure 3.4: Comparison of the distributions of the decay vertex Z positions for data (dots) and MC (histogram). The MC includes signal and background events. Both MC and data were collected with the final selection cuts listed in Table 3.2 except for the cut on the Z-vertex distribution. The data-to-MC ratios on the bottom are fit to a straight line. The vertical lines and arrows show the accepted region for $K_L \to \pi^{\pm} e^{\mp(}\bar{\nu}^{)} e^{+} e^{-}$ candidates (95m < Z-vertex < 150 m).

Figure 3.4 shows the comparison of the distributions of z position of vertex (Z-vertex) between data and MC[NLO(p^4)]. There is a good agreement between data and MC in the region of 95 m - 158 m. We required 95 m < Z-vertex < 150 m. The cut at 150 m with $M_{e^+e^-}$ cut rejected the background from $K_L \to \pi^{\pm} e^{\mp(}\bar{\nu}^{)} \gamma$ decays with an external conversion at the vacuum window.

Selection criteria introduced in this subsection:

- $E_K$max < 200 GeV,
- $P^{*2}_{\nu||}$> 0 GeV^2/c^2, and
- 95 m < Z-vertex < 150 m.

3.1.4 The energy of observed particles in the laboratory frame

The $K_L \to \pi^{\pm} e^{\mp(}\bar{\nu}^{)} e^{+} e^{-}$ decay mode has three electrons. We separated three electrons in two categories based on the invariant mass of e^+e^- pair. For three electrons, $e^{\mp}e^{+}e^{-}$, there are two candidates for the e^+e^- pairs. We define a 'e^+e^- pair' as a pair which has the smaller invariant mass, and call these constituents as 'e^+ and e^- from pair' ($e^{\pm}_{\rm pair}$), and the other electron as '$e^{\pm}$ from k_{e3}' ($e^{\pm}_{ke3}$). These are just notations. To calculate the decay amplitude, we made no such distinctions. According to Fermi statistics of electrons, we added two amplitudes for both larger mass candidate and smaller mass candidate of e^+e^- pair with opposite sing to each other.

The energy of $e^{\pm}_{ke3}$ were required to be greater than 10 GeV, while the energy of each e^+ and e^- from the 'pair' was required to be greater than 3 GeV. This energy requirement on $e^{\pm}_{ke3}$ suppressed pion contamination, because pion tended to leave a small energy deposit on the CsI calorimeter. Figure 3.5 shows the data-MC [NLO(p^4)] comparison of the energy distribution of observed particles. With regard to $e^{\pm}_{\rm pair}$, we show the energy distribution for only positrons. The distributions agree well between data and MC for both electrons and positrons

Selection criteria introduced in this subsection:

- $E^{\pm}_{\pi} > 10$ GeV,
- $E_{e^{\pm}_{ke3}} > 10$ GeV, and
- $E_{e^{\pm}_{\rm pair}} > 3$ GeV.

3.1.5 The invariant masses of some particle systems

Figure 3.6 shows the data-MC comparisons of three invariant masses, (a) $M_{\pi^{\pm}e^{\mp}e^{+}e^{-}}$, (b) $M_{e^{\pm}e^{+}e^{-}}$, and (c) $M_{e^{+}e^{-}}$. We required the invariant mass of $\pi^{\pm}e^{\mp}e^{+}e^{-}$ system to be less than 0.5 GeV/c^2. As shown in Fig. 3.6 (a), the number of events that failed this cut was negligible. For $e^{\pm}e^{+}e^{-}$ system, we did not require any restrictions. As shown in Fig. 3.6 (b),

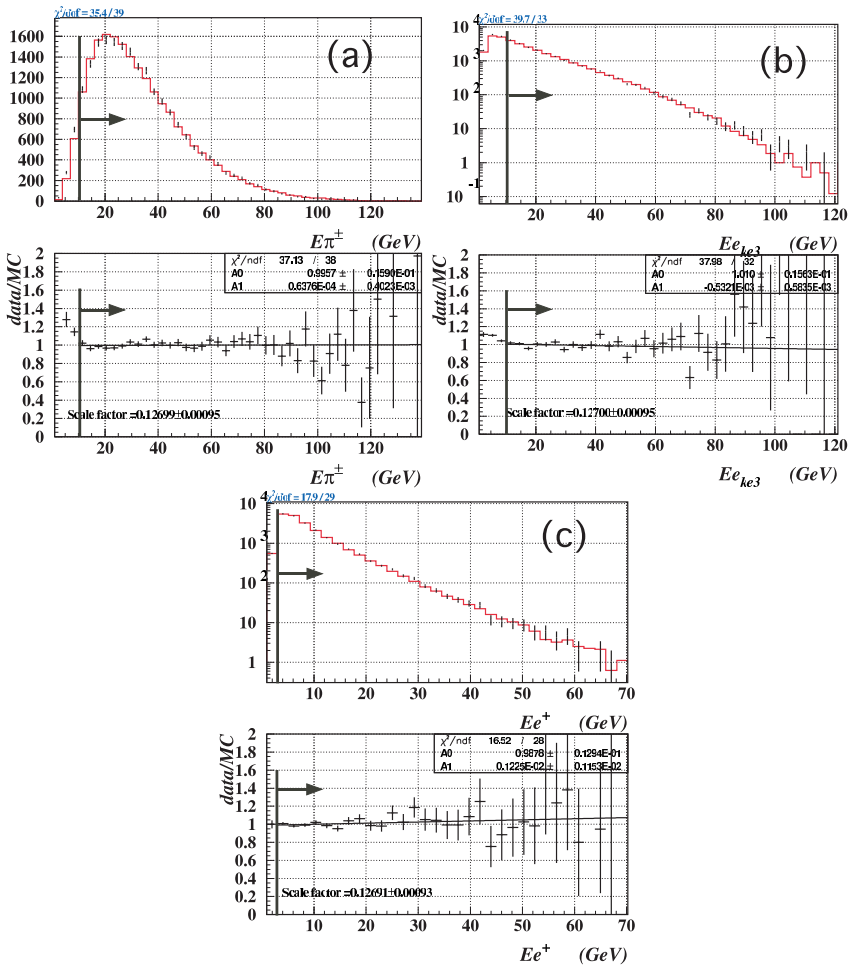

Figure 3.5: Comparison of the distributions of observed particle energy for (a) $\pi^{\pm}$, (b) $e^{\pm}_{ke3}$, and (c) e^{+} in the $e^{\pm}_{\rm pair}$, for data (dots) and MC (histogram). The MC includes signal and background events. Both MC and data were collected with the final selection cuts listed in Table 3.2 except for the cuts on the relevant distributions. The data-to-MC ratios on the bottom are fit to a line. There are good agreements between data and MC for every particle. The vertical lines and arrows show the accepted retions for $K_L \to \pi^{\pm}e^{\mp}\overset{(-)}{\nu}e^{+}e^{-}$ candidates ($E^{\pm}_{\pi} > 10$ GeV, $E_{e^{\pm}_{ke3}} > 10$ GeV, and $E_{e^{\pm}_{\rm pair}} > 3$ GeV). The e^{-} in the $e^{\pm}_{\rm pair}$ had the same energy spectrum as the e^{+}.

there is a peak at 0.13 GeV/c^2 in the $M_{e^\pm e^+ e^-}$ spectrum, and the peak is simulated well by MC. This peak is composed of backgrounds from the $K_L \to \pi^+\pi^-\pi^0_D$ and $K_L \to \pi^+\pi^-\pi^0_{4e}$ decays. Both distributions of $M_{\pi^\pm e^\mp e^+ e^-}$ and $M_{e^\pm e^+ e^-}$ have good agreements with data and MC.

The invariant mass of e^+e^- pair system was required to be greater than 0.005 GeV/c^2 to separate the $K_L \to \pi^\pm e^{\mp(}\bar{\nu}^{)}\gamma$ events from external conversion backgrounds. The data-to-MC ratio of the invariant mass of e^+e^- pair has a significant slope of 2.8σ. The effect of this discrepancy between data and MC on the branching fraction of $K_L \to \pi^\pm e^{\mp(}\bar{\nu}^{)}e^+e^-$ decay is discussed in Sec. 4.3. The data-MC discrepancy in $M_{e^+e^-}$ is of our most interest to study the K-π structure. We will discuss it in 5.4.

Selection criteria introduced in this subsection:

- $M_{\pi^\pm e^\mp e^+ e^-} < 0.5$ GeV/c^{2}and
- $M_{e^+e^-} > 0.005$ GeV/c^2.

3.1.6 A kinematic requirement to reduce $K_L \to \pi^+\pi^-\pi^0_D$ background

The primary background for the $K_L \to \pi^\pm e^{\mp(}\bar{\nu}^{)}e^+e^-$decay is $K_L \to \pi^+\pi^-\pi^0_D$, where π^0_D denotes the $\pi^0 \to e^+e^-\gamma$ decay, and one of the charged pions is misidentified as an electron, or the photon converts to e^+e^- pair and a charged pion and an electron are lost.

To suppress $K_L \to \pi^+\pi^-\pi^0_D$ backgrounds, we use an additional kinematic variable, k_{+-0}. The k_{+-0} is the square of the longitudinal momentum of the π^0 from $K_L \to \pi^+\pi^-\pi^0$ decay, in the reference frame in which the sum of the charged pion momenta is orthogonal to the kaon momentum. In our $K_L \to \pi^\pm e^{\mp(}\bar{\nu}^{)}e^+e^-$ analysis, the track identified as $e^\pm_{ke3}$ is treated as a $\pi^\pm$. The k_{+-0} is expressed as:

$$k_{+-0} = \frac{(m_K^2 - m_{\pi\pi}^2 - m_{\pi^0}^2)^2 - 4m_{\pi\pi}^2 m_{\pi^0}^2 - 4m_K^2 p_t^2}{4(m_{\pi\pi}^2 + p_t^2)}, \tag{3.6}$$

where m_K and m_{π^0} are the masses of kaon and π^0, respectively, and $m_{\pi\pi}$ is the π^+-π^- invariant mass. The p_t is the squared transverse momentum of whole of observed track system.

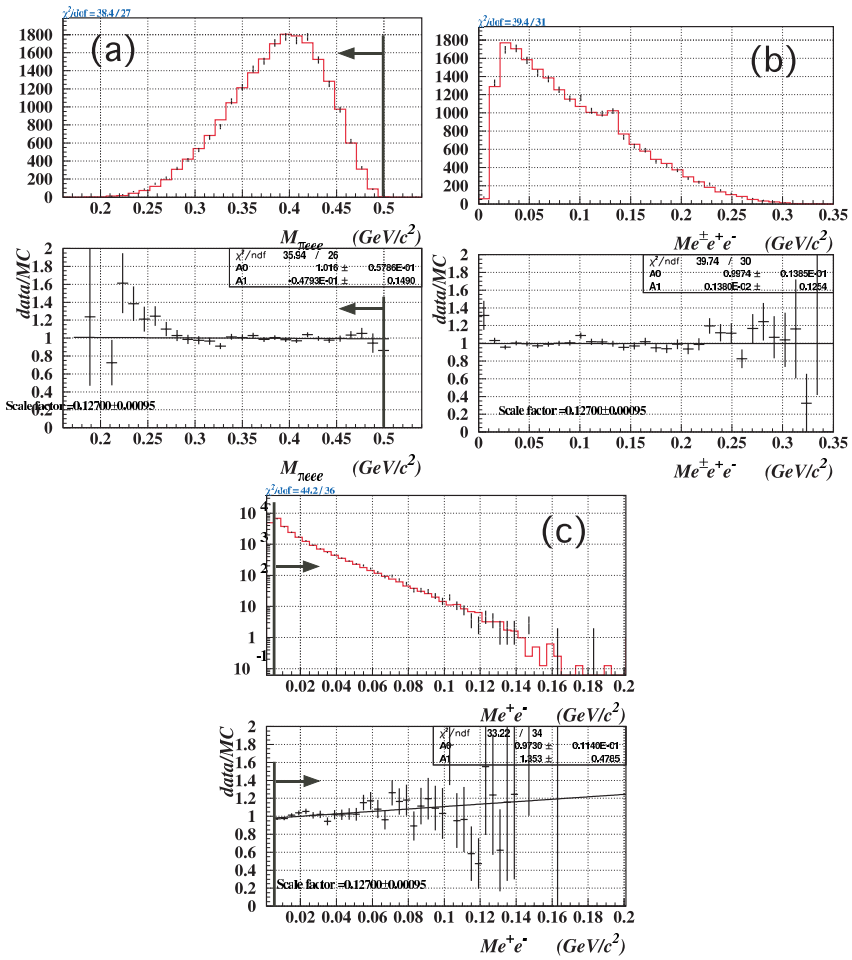

Figure 3.6: Comparison of the distributions of invariant mass systems, (a) $M_{\pi^{\pm}e^{\mp}e^{+}e^{-}}$, (b) $M_{e^{\pm}e^{+}e^{-}}$, and (c) $M_{e^{+}e^{-}}$, for data (dots) and MC (histogram). The MC includes signal and background events. Both MC and data were collected with the final selection cuts listed in Table 3.2 except for the cuts on the relevant distributions. The vertical lines and arrows show the accepted regions for $K_L \to \pi^{\pm}e^{\mp}\overset{(-)}{\nu}e^{+}e^{-}$ candidates ($M_{\pi^{\pm}e^{\mp}e^{+}e^{-}} < 0.5$ GeV/c^2, $M_{e^{+}e^{-}} < 0.005$ GeV/c^2). The data-to-MC ratios on the bottom are fit to a straight line. A peak in $M_{e^{\pm}e^{+}e^{-}}$ spectrum at 0.13 GeV/c^2 is composed of backgrounds from $K_L \to \pi^{+}\pi^{-}\pi^{0}_{D}$ and $K_L \to \pi^{+}\pi^{-}\pi^{0}_{4e}$ (See Sec. 3.2.1 and 3.2.3), and is well simulated by MC. Only $M_{e^{+}e^{-}}$ has a 2.8σ slope in the data-MC ratio.

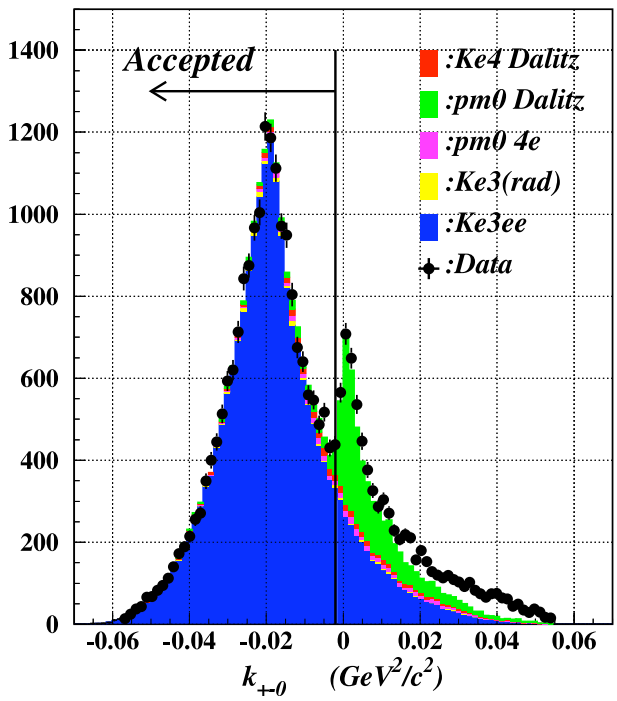

Figure 3.7: the k_{+-0} distributions of data and MC's after all analysis requirements except 'k_{+-0}'. Ke4 Dalitz, pm0 Dalitz, pm0 4e, Ke3(rad), and Ke3ee denote $K_L \to \pi^{\pm}e^{\mp}\nu\pi^0_D$, $K_L \to \pi^+\pi^-\pi^0_D$, $K_L \to \pi^+\pi^-\pi^0_{4e}$, $K_L \to \pi^{\pm}e^{\mp}\overset{(-)}{\nu}\gamma$, and $K_L \to \pi^{\pm}e^{\mp}\overset{(-)}{\nu}e^+e^-$, respectively. The vertical line and arrow show the accepted region for $K_L \to \pi^{\pm}e^{\mp}\overset{(-)}{\nu}e^+e^-$ candidates (k_{+-0}< 0.002 GeV^2/c^2).

Figure 3.7 shows the k_{+-0} distributions for data and MC's after all analysis requirements except k_{+-0}. The events from $K_L \to \pi^+\pi^-\pi^0$ decays have positive k_{+-0} values, while most of the events from the $K_L \to \pi^{\pm}e^{\mp}\overset{(-)}{\nu}$ including the $K_L \to \pi^{\pm}e^{\mp}\overset{(-)}{\nu}e^+e^-$, have the negative k_{+-0}. We can see that the largest background from the $K_L \to \pi^+\pi^-\pi^0_D$ decays. We thus required k_{+-0}< -0.002 GeV^2/c^2.

Selection criterion introduced in this subsection:

- k_{+-0}< -0.002 GeV/c^2.

3.1.7 Summary of the selection criteria

Table 3.2 summaries the selection cuts for the signal mode. With these selection criteria, 20225 signal candidates remained, including backgrounds estimated in the next section.

Table 3.2: Selection cuts for the signal mode

Cut
$X_{offmag} < 6$ mm
Cluster-track matching < 0.07 m
$\chi^2_{vtx} < 125$
$E_{\text{kaon}}\text{max} < 200\text{GeV}$
95 m $<$ Z-vertex $<$ 150 m
E/p for pion track < 0.90
$0.93 < E/p < 1.15$ for electron track
TRD $Prob_\pi$ for electron track < 0.06
$E_\pi > 10$ GeV
$E_{e^\pm_{ke3}} > 10$ GeV
$E_{e^\pm_{\text{pair}}} > 3$ GeV
$M_{e^+e^-} > 0.005$ GeV/c^2
$M_{\pi^\pm e^\mp e^+ e^-} < 0.5$ GeV/c^2
$k_{+-0} < -0.002$ GeV^2/c^2
$P^{*2}_{\nu\|} > 0$ GeV^2/c^2
No crossing tracks in the x view within TRD

3.2 Background estimation

The number of background events from the decay i remaining after all selection cuts is estimated with MC as:

$$N_{\text{BG}i} = A_{\text{BG}i} \cdot B_{\text{BG}i} \cdot \prod_j (1+\delta_j)^{-1} \cdot K_{flux}, \tag{3.7}$$

where

$N_{\text{BG}i}$	:	the number of estimated background events caused by decay mode i,
$A_{\text{BG}i}$	:	acceptance for background i determined by MC,
$B_{\text{BG}i}$	:	the branching fraction of background decay mode i,
δ_j	:	correction factor for the data-MC discrepancy j for each particle and each particle identification method,
K_{flux}	:	the number of total kaon decays.

For each decay mode i, the acceptance is defined as:

$$A_{\text{BG}i} = N_{\text{MC}i}/G_{\text{MC}i}, \tag{3.8}$$

where $N_{\text{MC}i}$ is the number of accepted events in the final analysis cuts in MC, and $G_{\text{MC}i}$ is the number of generated MC events. Table 3.3 lists the acceptances of background decay modes.

Table 3.3: A list of acceptance for background modes.

Decay mode	Acceptance
$K_L \to \pi^+\pi^-\pi^0_D$	$(1.01 \pm 0.04) \times 10^{-6}$
$K_L \to \pi^\pm e^\mp \nu \pi^0_D$	$(3.09 \pm 0.06) \times 10^{-3}$
$K_L \to \pi^+\pi^-\pi^0_{4e}$	$(2.79 \pm 0.14) \times 10^{-4}$
$K_L \to \pi^\pm e^{\mp(}\bar{\nu}^{)}(\gamma)$	$(2.29 \pm 0.25) \times 10^{-9}$
Double $K_L \to \pi^\pm e^{\mp(}\bar{\nu}^{)}$	$(1.51 \pm 0.35) \times 10^{-8}$
$\Xi \to \Lambda(\to p\pi^-)\pi^0_D$	$(1.1 \pm 0.5) \times 10^{-6}$

3.2.1 $K_L \to \pi^+\pi^-\pi^0_D$

There are following two ways for the $K_L \to \pi^+\pi^-\pi^0_D$ decays to fake $\pi^\pm e^\mp e^+ e^-$ events:

(i) An electron is lost and a pion is misidentified as an electron.

(ii) A photon from $K_L \to \pi^+\pi^-\pi^0_D$ decay converts to a e^+e^- pair in the detector materials, and an electron and a pion are lost.

To reject the background (i), the π-e rejection is crucial. Our π-e rejection was done by cutting on E/p and TRD $Prob_\pi$ parameter. As discussed in Sec. 3.1.2, the fraction that $\pi^\pm$ track have $E/p > 0.9$ is 0.81% in data, but 0.57% in MC. This discrepancy is crucial for the background estimation. Figure 3.8 shows E/p for $e^\pm_{ke3}$ in the events collected with positive k_{+-0}, to enhance the background from $K_L \to \pi^+\pi^-\pi^0_D$ decay. The estimated E/p distribution of $e^\pm_{ke3}$ from $K_L \to \pi^\pm e^{\mp(}\bar{\nu}^{)} e^+ e^-$ decays is subtracted from data. There is a large discrepancy between data and MC. We estimate that the amount of background from $K_L \to \pi^+\pi^-\pi^0_D$ decays with $0.93 < E/p < 1.15$ should be multiplied by 1.760 ± 0.009 ($f_{\pi e:E/p}$).

The π-e separation by TRD also has a similar problem. We estimate the number of pions having $Prob_\pi < 0.06$ for data and MC, using pions in $K_L \to \pi^+\pi^-\pi^0_D$ decays selected by $E/p < 0.6$. The discrepancy between data and MC becomes 1.087 ± 0.004 ($f_{\pi e:\mathrm{TRD}}$). This value also should be multiplied to the MC estimation for the amount of background from (i).

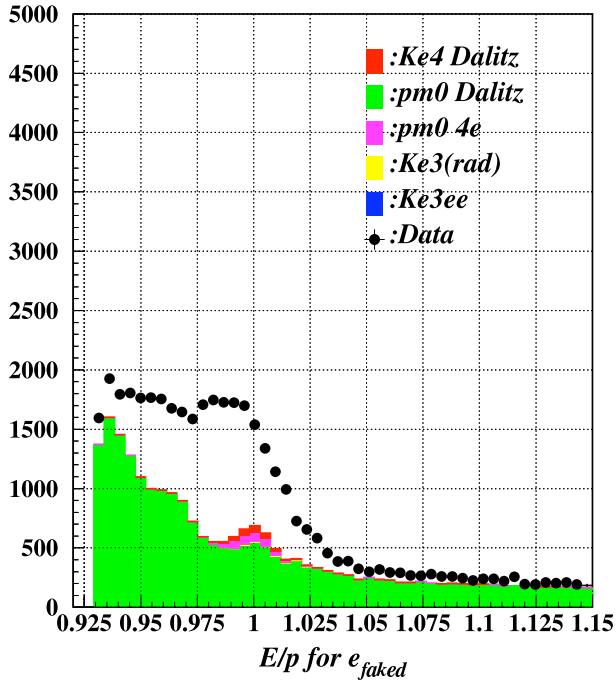

Figure 3.8: The E/p distribution of $e^{\pm}_{ke3}$ for data (dots) and MC (histogram). To enhance the $K_L \to \pi^+\pi^-\pi^0_D$ decays, events were required to have positive k_{+-0}. From data, the estimated E/p distribution of $e^{\pm}_{ke3}$ from $K_L \to \pi^{\pm}e^{\mp}\overset{(-)}{\nu}e^+e^-$ decays been subtracted. Ke4 Dalitz, pm0 Dalitz, pm0 4e, Ke3(rad), and Ke3ee denote $K_L \to \pi^{\pm}e^{\mp}\nu\pi^0_D$, $K_L \to \pi^+\pi^-\pi^0_D$, $K_L \to \pi^+\pi^-\pi^0_{4e}$, $K_L \to \pi^{\pm}e^{\mp}\overset{(-)}{\nu}\gamma$, and $K_L \to \pi^{\pm}e^{\mp}\overset{(-)}{\nu}e^+e^-$, respectively.

The details of estimations of these factors are discussed in Appendix F.

In order to correct the number of background from (i) by $f_{\pi e:E/p}$ and $f_{\pi e:\mathrm{TRD}}$, we need to know the ratio of (i) to the all the $K_L \to \pi^+\pi^-\pi^0_D$ background events in MC.

Figure 3.9(a) shows the three electron invariant mass distributions after all the selection cuts. We can see a peak at 0.13 GeV/c^2. The MC shows that one of the dominant component of this peak is from the $K_L \to \pi^+\pi^-\pi^0_D$ decays.

We made a small sample of MC for the $K_L \to \pi^+\pi^-\pi^0_D$ background, and separated them between (i) and (ii). Figure 3.9(b) shows the $M_{e^\pm e^+ e^-}$ distribution of such samples. In case of (ii), one of the four electrons was kicked out by the analysis magnet due to its small momentum. The remaining three-electron system has the invariant mass near (but just small) the π^0 mass, because it carries most of the momentum of the parent π^0. From Fig. 3.9(b), the ratio of background (i) to the whole of $K_L \to \pi^+\pi^-\pi^0_D$ background in MC is $0.422 \pm 0.024_{stat}$ (R_{fakeMC}).

Finally, we estimated a correction factor, f_{+-0}, to be multiplied the total number of $K_L \to \pi^+\pi^-\pi^0_D$ background of default MC as:

$$f_{+-0} = 1 - R_{\mathrm{fake}} + R_{\mathrm{fake}} \cdot f_{\pi-e\mathrm{fake}}, \tag{3.9}$$

where $f_{\pi-e\mathrm{fake}} = f_{\pi e:E/p} \cdot f_{\pi e:\mathrm{TRD}}$. First two terms express the fraction of (ii) in MC, and the last term is the corrected fraction for (i) in MC.

After all the analysis requirements and corrections on the π-e rejection, the estimated number of background events from $K_L \to \pi^+\pi^-\pi^0_D$ is 350 ± 14. This is 1.7% of the number of signal events.

3.2.2 $K_L \to \pi^\pm e^\mp \nu \pi^0_D$

The background from $K_L \to \pi^\pm e^\mp \nu \pi^0_D$ is difficult to suppress because it has the same final state as the $K_L \to \pi^\pm e^\mp \overset{(-)}{\nu} e^+ e^-$ except for an additional photon. The most effective background suppression is the cut on k_{+-0}, reducing the background by 45%. Since the

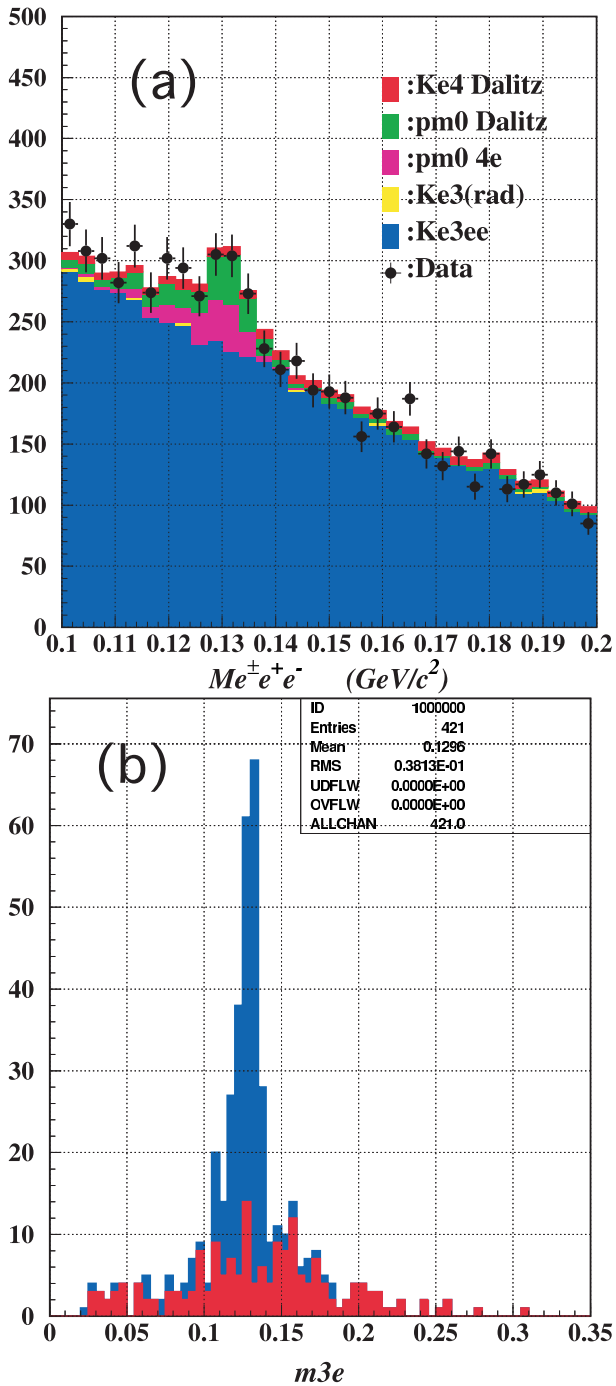

Figure 3.9: (a) The $M_{e^\pm e^+ e^-}$distributions of data and MC's arround 0.13 GeV/c^2. According to MC, the peak at 0.13 GeV/c^2 is composed of $K_L \to \pi^+\pi^-\pi^0_D$ background and $K_L \to \pi^+\pi^-\pi^0_{4e}$ background. (b) shows the $M_{e^\pm e^+ e^-}$distributions for MC $K_L \to \pi^+\pi^-\pi^0_D$ background. The events in red histogram are composed of pion faking electron and the events in blue histogram are made with the external conversion processes followed by missing a pion and an electron. Ke4 Dalitz, pm0 Dalitz, pm0 4e, Ke3(rad), and Ke3ee denote $K_L \to \pi^\pm e^\mp \nu \pi^0_D$, $K_L \to \pi^+\pi^-\pi^0_D$, $K_L \to \pi^+\pi^-\pi^0_{4e}$, $K_L \to \pi^\pm e^{\mp(-)}\gamma$, and $K_L \to \pi^\pm e^{\mp(-)} e^+ e^-$, respectively.

branching ratio of $K_L \to \pi^{\pm}e^{\mp}\nu\pi^0_D$ is small, BR($K_L \to \pi^{\pm}e^{\mp}\nu\pi^0$)]= $(5.20 \pm 0.11) \times 10^{-5}$ and BR($\pi^0 \to e^+e^-\gamma$) = $(1.198 \pm 0.032) \times 10^{-2}$ [29], the estimated number of background events from $K_L \to \pi^{\pm}e^{\mp}\nu\pi^0_D$ is 321.0 ± 6.5. This is 1.6% of the number of signal events.

3.2.3 $K_L \to \pi^+\pi^-\pi^0_{4e}$

Figure. 3.9 shows that the $K_L \to \pi^+\pi^-\pi^0$ decay followed by $\pi^0 \to e^+e^-e^+e^-$ ($K_L \to \pi^+\pi^-\pi^0_{4e}$) is also a large component of the peak at 0.13 GeV/c^2. The mechanism that the $K_L \to \pi^+\pi^-\pi^0_{4e}$ background makes 0.13 GeV/c^2 peak is similar as in the case of (ii) of the $K_L \to \pi^+\pi^-\pi^0_D$ background. Without any additional cuts, the estimated number of $K_L \to \pi^+\pi^-\pi^0_{4e}$ events is 183.7 ± 8.9. This is 0.91% of the number of signal events.

3.2.4 $K_L \to \pi^{\pm}e^{\mp(}\bar{\nu}^{)}\gamma$

The radiative decay, $K_L \to \pi^{\pm}e^{\mp(}\bar{\nu}^{)}\gamma$ with the photon converting into a e^+e^- pair in material, is suppressed by the cut on $M_{e^+e^-}$, and the track separation requirement at the vacuum window. Our cut-off value of the invariant mass of e^+e^- pair, 0.005 GeV/c^2, reduces the $K_L \to \pi^{\pm}e^{\mp(}\bar{\nu}^{)}\gamma$ background to 155 ± 17 events. This is 0.77% of the number of signal events. We did not use the track separation cut because the requiring > 0.01 m for the the track separation at the vacuum window reduces only 2 events from above results.

This is 0.72% of signal events.

3.2.5 $K_L \to \pi^{\pm}e^{\mp(}\bar{\nu}^{)}$ double decays

Two $K_L \to \pi^{\pm}e^{\mp(}\bar{\nu}^{)}$ decays in the same RF bucket with misidentifying a pion as an electron gives the same charged particles as $K_L \to \pi^{\pm}e^{\mp(}\bar{\nu}^{)}e^+e^-$. The number of such double $K_L \to \pi^{\pm}e^{\mp(}\bar{\nu}^{)}$ decays is estimated as:

$$N_{\mathrm{double}K_{e3}} = \frac{K_{flux}B^2_{K_{e3}}K_F}{R_F}, \tag{3.10}$$

where K_{flux} is the number of total kaon decays, $B_{K_{e3}}$ is the branching fraction of $K_L \to \pi^{\pm}e^{\mp(}\bar{\nu}^{)}$ decay mode, K_F is the kaon decay rate, and R_F is the frequency of the RF bucket.

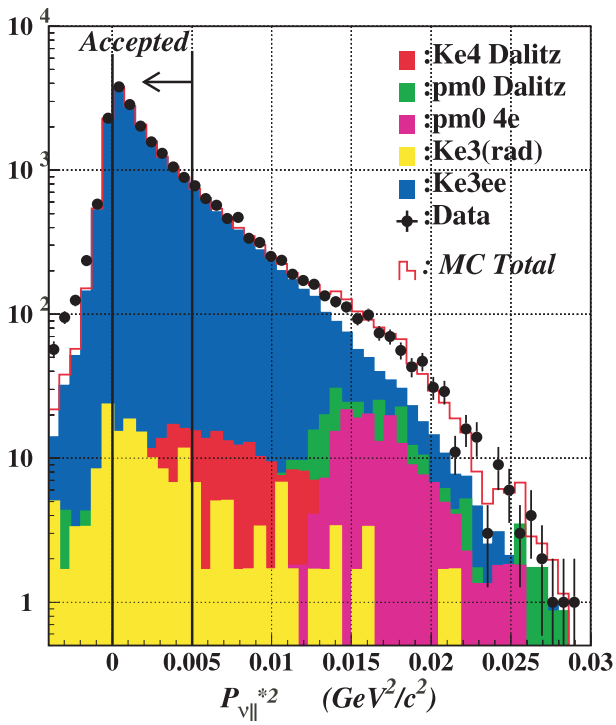

Figure 3.10: The $P^{*2}_{\nu||}$ distribution of data and MC. The low background sub-sample is between two vertical lines. Ke4 Dalitz, pm0 Dalitz, pm0 4e, Ke3(rad), and Ke3ee denote $K_L \to \pi^{\pm}e^{\mp}\nu\pi^0_D$, $K_L \to \pi^+\pi^-\pi^0_D$, $K_L \to \pi^+\pi^-\pi^0_{4e}$, $K_L \to \pi^{\pm}e^{\mp}\overset{(-)}{\nu}\gamma$, and $K_L \to \pi^{\pm}e^{\mp}\overset{(-)}{\nu}e^+e^-$, respectively. The vertical lines and arrow show the accepted region for the low background sample of $K_L \to \pi^{\pm}e^{\mp}\overset{(-)}{\nu}e^+e^-$ candidates (0 GeV^2/c^2 $< P^{*2}_{\nu||} <$ 0.005 GeV^2/c^2)

The estimated number of this background events is 7.9 ± 1.8, which is 0.04% of signals.

3.2.6 $\Xi \to \Lambda(\to p\pi^-)\pi^0_D$

The $\Xi \to \Lambda(\to p\pi^-)\pi^0_D$ decay could be a background source, if a proton is misidentified as a pion and a pion is misidentified as an electron.The number of the cascade decays (cascade flux) is estimated based on [30]. The estimated number of this background is 1.2 ± 0.5 events. This is 0.006% of signal events.

3.2.7 A confirmation of background estimation using $P^{*2}_{\nu||}$

The semileptonic kaon decays have a unique $P^{*2}_{\nu||}$ distribution, as shown in Fig. 3.10. The distribution has a good agreement between data and MC. A tighter requirement of $P^{*2}_{\nu||}<$

0.005 GeV^2/c^2 reduces total backgrounds from 5.0% of the signal to 1.7%.

As we can see in Table 3.4, the number of $K_L \to \pi^\pm e^{\mp(}\bar{\nu}^{)} e^+ e^-$ decays after acceptance correction is consistent with and without the $P^{*2}_{\nu||}$< 0.005 GeV^2/c^2 cut.

3.3 Summary of the signal analysis

The number of signal events and the estimated number of background events after these cuts are listed in Table 3.4. We observed 20225 signal candidate events, including 1019±25 background events.

The MC to estimate the acceptance of $K_L \to \pi^\pm e^{\mp(}\bar{\nu}^{)} e^+ e^-$ reproduces kinematic distributions, except for the invariant mass of e^+e^- pair.

Table 3.4: The number of observed events in data and the estimated number of backgrounds by MC. The errors for the 'Estimated $K_L \to \pi^\pm e^{\mp(}\bar{\nu}^{)} e^+ e^-$ after acceptance correction' are only statistical.

Decay mode	Full sample	Low BG sample
Data		
Signals including BG	20225	14605
MC		
$K_L \to \pi^+\pi^-\pi^0_D$	350.3±13.5	32.8±4.1
$K_L \to \pi^\pm e^\mp \nu \pi^0_D$	320.8±6.5	108.7±3.8
$K_L \to \pi^+\pi^-\pi^0_{4e}$	183.7±8.9	3.0±1.1
$K_L \to \pi^\pm e^{\mp(}\bar{\nu}^{)}\gamma$	155.2±17.5	99.6±13.9
Double $K_L \to \pi^\pm e^{\mp(}\bar{\nu}^{)}$	7.9±1.8	5.8±1.6
$\Xi \to \Lambda(\to p\pi^-)\pi^0_D$	1.2±0.5	0.2±0.2
Total BG ratio	5.04±0.12%	1.71±0.10%
Generated $K_L \to \pi^\pm e^{\mp(}\bar{\nu}^{)} e^+ e^-$ ($M_{ee} > 5$ MeV/c^2, $E_{ee} > 30$ GeV)	16839585	16839585
Accepted MC $K_L \to \pi^\pm e^{\mp(}\bar{\nu}^{)} e^+ e^-$	151318	113943
Estimated $K_L \to \pi^\pm e^{\mp(}\bar{\nu}^{)} e^+ e^-$ after acceptance correction	$(2.137 \pm 0.016) \times 10^6$	$(2.121 \pm 0.019) \times 10^6$

3.4 Kaon flux

We use the $K_L \to \pi^+\pi^-\pi^0_D$ decay as a normalization mode to measure the number of K_L decays. We do not use the photon information to reconstruct the $K_L \to \pi^+\pi^-\pi^0_D$ events, because photons are ignored in $K_L \to \pi^\pm e^{\mp(}\bar{\nu}^{)} e^+e^-$ analysis. Therefore, we use the $\pi^+\pi^-e^+e^-$ four-track events accepted by the same "four-track" trigger as the $K_L \to \pi^\pm e^{\mp(}\bar{\nu}^{)} e^+e^-$ analysis.

The Kaon flux is estimated as:

$$K_{flux} = \frac{N_{\rm nrm}(1+\delta_{e,E/p})^2(1+\delta_{\pi,E/p})^2(1+\delta_{e,TRD})^2}{A_{\rm nrm}B_{\rm nrm} + \sum_i A_{{\rm BG}i}\ B_{{\rm BG}i}} f_G, \quad \text{and} \tag{3.11}$$

$$K'_{flux} = \frac{N_{\rm nrm}}{A_{\rm nrm}B_{\rm nrm} + \sum_i A_{{\rm BG}i}\ B_{{\rm BG}i}}, \tag{3.12}$$

where

K_{flux}	:	the number of total K_L decays in the analyzed data,
$N_{\rm nrm}$	:	the number of observed normalization mode events after all selection cuts for normalization analysis,
δ_j	:	correction factor$_j$ for the discrepancy between data and MC in the E/p and TRD separation (see Sec. 3.1.2),
$A_{\rm nrm}$	:	the acceptance for normalization mode,
$B_{\rm nrm}$	:	the branching fraction of the normalization mode,
$A_{{\rm BG}i}$	:	the acceptance for background decay i,
$B_{{\rm BG}i}$	:	the branching fraction of background decay i, and
f_G	:	a factor to adjust the range of kaon energy, and
K'_{flux}	:	K_{flux} without corrections by δ_j and adjusting the kaon energy region.

The acceptance of each decay mode is determined with MC.

In many previous studies by KTeV, the kaon flux has been defined in the kaon energy range between 20 and 220 GeV. The factor f_G is applied to adjust the energy range of kaon flux, because we generated K_L in the energy range between 15 and 225 GeV.

K'_{flux} will be used to estimate the $K_L \to \pi^\pm e^{\mp(}\bar{\nu}^{)} e^+e^-$ branching fraction.

3.4.1 Event selection for $K_L \to \pi^+\pi^-\pi^0_D$

The event selection cuts for the $K_L \to \pi^+\pi^-\pi^0_D$ events were made similar as possible as the $K_L \to \pi^\pm e^{\mp(}\bar{\nu}^{)} e^+e^-$ analysis. The kaon energy has a two-fold ambiguity, just as in the

$K_L \to \pi^{\pm} e^{\mp(}\bar{\nu}^{)} e^+ e^-$ analysis, because we do not use photon information. Table 3.5 lists the cuts for the $K_L \to \pi^+\pi^-\pi^0_D$ analysis.

Table 3.5: Selection cuts for the normalization mode

Cut
$\chi^2_{vtx} < 125$
E_{kaon} max < 200GeV
95 m $<$ Z-vertex 150 m
$0.93 < E/p < 1.15$ for electron track
E/p for pion track < 0.90
TRD $Prob_\pi$ for electron track < 0.06
$E_\pi > 10$ GeV
$E_{e^\pm} > 3$ GeV
$M_{e^+e^-} > 0.005$ GeV/c^2
$M_{\pi\pi ee} < 0.5$ GeV/c^2
$P^*_{\gamma\|} > 0$ GeV^2/c^2
$k_{+-0} > -0.002$ GeV^2/c^2
No crossing tracks in the x view within TRD
For full reconstruction sample
0.492 GeV/c$^2 < M_{\pi\pi ee\gamma} <$ 0.508 GeV/c^2
0.127 GeV/c$^2 < M_{ee\gamma} <$ 0.143 GeV/c^2

Here, we describe only the differences between signal and normalization mode analyses. For the normalization mode analysis, first, we required two charged pions with opposite charges, and two electrons with opposite charges, instead of one charged pion and three electrons. Next, we required $k_{+-0} > -0.002$ GeV^2/c^2 instead of $k_{+-0} < -0.002$ GeV^2/c^2 to select $K_L \to \pi^+\pi^-\pi^0$ decays. Third, we defined the square of the longitudinal momentum of the photon in the kaon rest frame ($P^*_{\gamma\|}$) in the similar way as for $P^{*2}_{\nu\|}$, and required $P^*_{\gamma\|} > 0$. Figure 3.11 shows a data-MC comparison for the two kaon energy solutions. Figure 3.12 shows data-MC comparison for the Z-vertex distribution. Figure 3.13 shows data-MC comparisons of energy distributions of both electrons and charged pions in the laboratory frame. The data-MC comparisons for the invariant mass distribution of $\pi^+\pi^-e^+e^-$ and e^+e^- pair are shown in Fig 3.14 and Fig 3.15, respectively.

These comparisons show good agreements in the cut for cut regions for $K_L \to \pi^{\pm} e^{\mp(}\bar{\nu}^{)} e^+ e^-$.

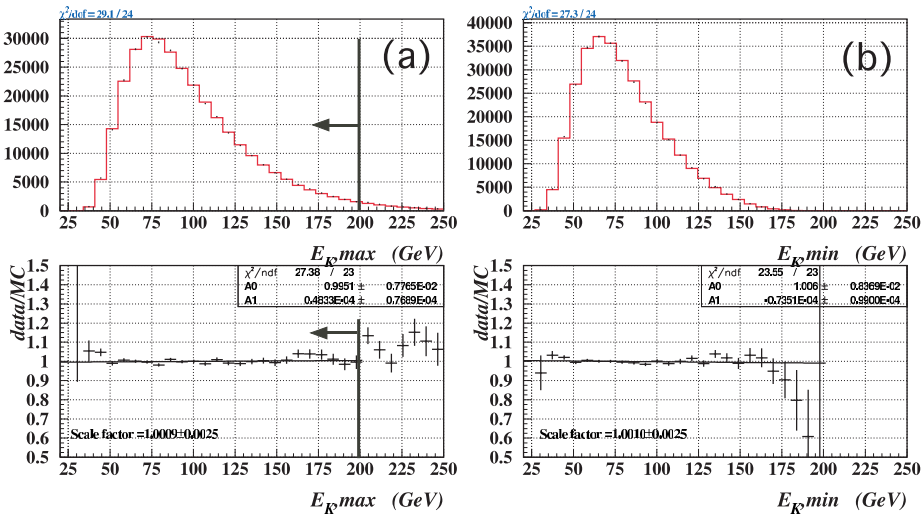

Figure 3.11: The distribution of (a) maximum of the kaon energy solution, and (b) minimum of the kaon solution, for data (dots) and MC (histogram). The MC includes signal and background events. Both MC and data were collected with the final selection cuts listed in Table 3.5 except for the cuts on the relevant distributions. The data-to-MC ratios on the bottom are fit to a straight line. There are good agreements between data and MC. The vertical line and arrow show the accepted region for $K_L \to \pi^+\pi^-\pi^0_D$ candidates ($E_K max >$ 200 GeV) .

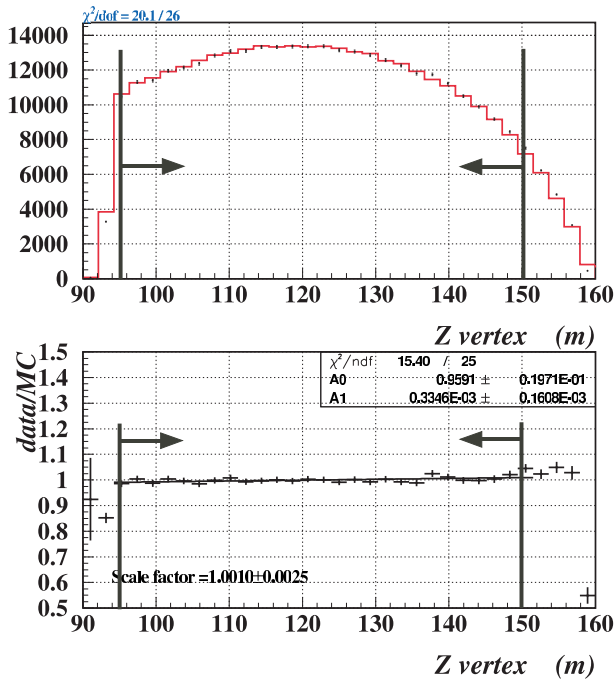

Figure 3.12: Comparison of the $Z - vertex$ distributions of the normalization mode for data (dots) and MC (histogram). The MC includes signal and background events. Both MC and data were collected with the final selection cuts listed in Table 3.5 except for the cuts on the Z-vertex distributions. The data-to-MC ratios on the bottom are fit to a straight line. There is a good agreement between data and MC. The vertical lines and arrows show the accepted region for $K_L \to \pi^+\pi^-\pi^0_D$ candidates (95 m < Z-vertex < 150 m) .

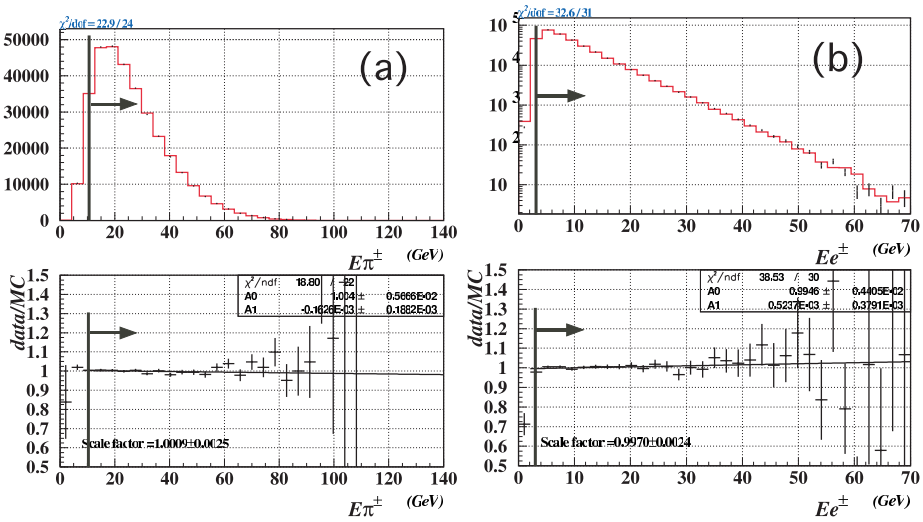

Figure 3.13: The distribution of (a) $\pi^{\pm}$ energy distribution, and (b) $e^{\pm}$ energy distribution , for data (dots) and MC (histogram). The MC includes signal and background events. Both MC and data were collected with the final selection cuts listed in Table 3.5 except for the cuts on the relevant distributions. The data-to-MC ratios on the bottom are fit to a straight line. There are good agreements between data and MC. The vertical lines and arrows show the accepted regions for $K_L \to \pi^+\pi^-\pi^0_D$ candidates ($E^{\pm}_{\pi} > 10$ GeV and $E^{\pm}_{e} > 3$ GeV) .

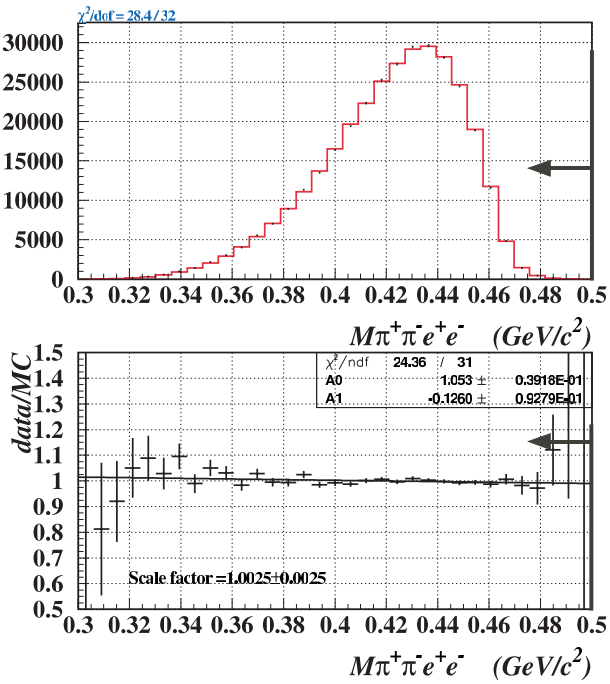

Figure 3.14: Comparison of the invariant mass distributions; $M_{\pi\pi ee}$, for data (dots) and MC (histogram). The MC includes signal and background events. Both MC and data were collected with the final selection cuts listed in Table 3.5 except for the cuts on the $M_{\pi\pi ee}$ distributions. The data-to-MC ratios on the bottom are fit to a straight line. There is a good agreement between data and MC. The vertical line and arrow show the accepted region for $K_L \to \pi^+\pi^-\pi^0_D$ candidates ($M_{\pi\pi ee} < 0.5$ GeV) .

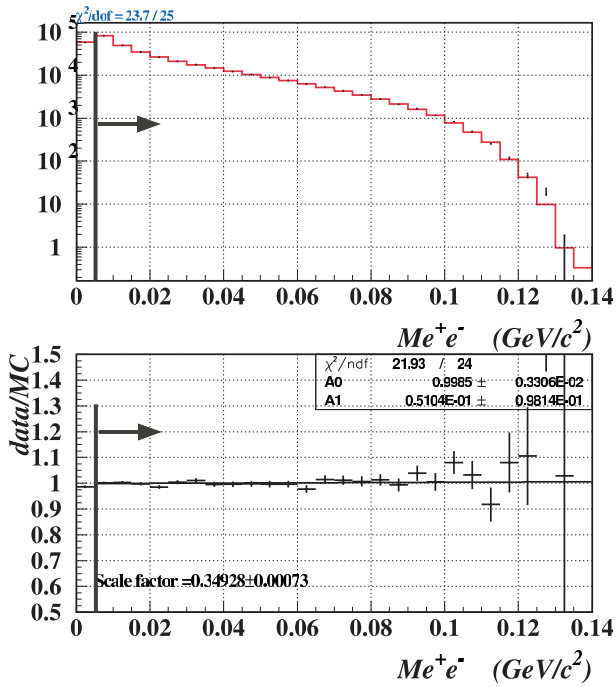

Figure 3.15: Comparison of the $M_{e^+e^-}$distribution for data (dots) and MC (histogram). The MC includes signal and background events. Both MC and data were collected with the final selection cuts listed in Table 3.5 except for the cuts on the $M_{e^+e^-}$ distributions. The data-to-MC ratios on the bottom are fit to a straight line. There are good agreements between data and MC. The vertical line and arrow show the accepted region for $K_L \to \pi^+\pi^-\pi^0_D$ candidates ($M_{e^+e^-} > 0.005$ GeV/c^2) .

3.4.2 Background for the normalization analysis

The dominant background for the $K_L \to \pi^+\pi^-\pi^0_D$ comes from the $K_L \to \pi^+\pi^-\pi^0_{\gamma\gamma}$ decay, where the π^0 decays to two photon and one of them converts to a e^+e^- pair. The number of $K_L \to \pi^+\pi^-\pi^0_{\gamma\gamma}$ backgbround decays was estimated using MC. The conversion rate was calculated with the radiation length of the vacuum window and the drift chambers upstream of the analysis magnet. After all the analysis requirements, we estimate that 1744 ± 17 background events remain in the $K_L \to \pi^+\pi^-\pi^0_D$ candidate. This number is 0.56% of $K_L \to \pi^+\pi^-\pi^0_D$ events.

The backgrounds from $K_L \to \pi^\pm e^{\mp(}\bar{\nu}^{)}$ double decays and $\Xi \to \Lambda(\to p\pi^-)\pi^0_D$ decay are negligible.

3.4.3 Result of the kaon flux

Table 4.3 lists the values required by Eq. 3.11 to estimate the kaon flux.

We define the kaon flux as the number of K_L decays in the kaon energy range between 20 and 220 GeV and decay position between 90 and 160 m downstream from the target. After all analysis requirements, we obtained 312707 $K_L \to \pi^+\pi^-\pi^0_D$ event candidates, including an estimated background of 1744 ± 17 events. The kaon flux is $[1.5233 \pm 0.0033(stat)] \times 10^{11}$, where the statistical error includes the error from data and MC.

There are some other kaon flux estimations for the same run period using the $K_L \to \pi^+\pi^-\pi^0_D$ decay. For example in Senyo's thesis [31], the electron and pion inefficiencies in E/p and TRD selection and the effect of π-hadron interaction have not been corrected, because the signal mode and normalization mode had the same numbers of electrons and pions. Our kaon flux without those corrections is $(1.407 \pm 0.013) \times 10^{11}$ [1], consistent with Senyo's kaon flux of 1.421×10^{11}.

[1] The error includes a systematic error discussed in 4.3

Table 3.6: A list of values to determine the kaon flux used in Eq. 3.11.

Element	Value	description
N_{nrm}	312707 $\times 4$	The number of accepted normalization mode events including the backgrounds ($\times$ prescale factor).
A_{nrm}	4.9468×10^{-3}	Acceptance for normalization decay mode. ($K_L \to \pi^+\pi^-\pi^0_D$).
B_{nrm}	1.4999×10^{-3}	BR[$K_L \to \pi^+\pi^-\pi^0$]$= 0.1252 \pm 0.007$ [32] $\times$ BR[$\pi^0 \to e^+e^-\gamma$]$(1.198 \pm 0.032) \times 10^{-2}$ [29].
A_{BGnrm}	3.364×10^{-7}	Acceptance for background $K_L \to \pi^+\pi^-\pi^0_{\gamma\gamma}$.
B_{BGnrm}	0.12370	Branching fraction of background. BR[$K_L \to \pi^+\pi^-\pi^0$] $\times$ BR[$\pi^0 \to \gamma\gamma$]$= 0.98798 \pm 0.00032$ [29]
f_G	0.8919 ± 0.0046	The number of generated events in E_K = 20-220 GeV : 15-225 GeV.
Corrections		Discrepancy of inefficiencies between data-MC.
$\delta_{e,E/p}$	+0.0034	Electron inefficiency in E/p selection.
$\delta_{e,TRD}$	+0.0035	Electron inefficiency in TRD selection.
$\delta_{\pi,E/p}$	+0.00243	Pion inefficiency in E/p selection.

Chapter 4

The branching fraction analysis of $K_L \to \pi^{\pm} e^{\mp(}\bar{\nu}^{)} e^+ e^-$

4.1 Measurement of the branching fraction of $K_L \to \pi^{\pm} e^{\mp(}\bar{\nu}^{)} e^+ e^-$

We measure the branching fraction of $K_L \to \pi^{\pm} e^{\mp(}\bar{\nu}^{)} e^+ e^-$ with cut-offs, $M_{e^+e^-} > 0.005$ GeV/c^2 and $E^*_{e^+e^-} > 0.03$ GeV, using the data summarized in Sec. 3.3, where $E^*_{e^+e^-}$ is the energy of e^+e^- pair in the kaon rest frame. As shown in Fig. 4.1, the acceptance of events with $E^*_{e^+e^-} < 0.03$ GeV is small. Therefore, we require the $E^*_{e^+e^-}$ cut-off.

We use the equation:

$$BR(K_L \to \pi^{\pm} e^{\mp} \nu e^+ e^-) = \frac{N_{\rm sig} - \sum_i N_{{\rm BGsig}i}}{A_{Ke3ee}} \quad K'^{-1}_{flux} \quad (1+\delta_e)(1+\delta_\pi)^{-1}, \tag{4.1}$$

where

$N_{\rm sig}$	:	the number of observed signal events in the final selection criteria for signal mode,
$N_{{\rm BGsig}i}$	:	the number of estimated background events caused by decay mode i,
A_{Ke3ee}	:	the acceptance of $K_L \to \pi^{\pm} e^{\mp} \nu e^+ e^-$ determined by MC,
K'_{flux}	:	uncorrected kaon flux (see Sec. 3.4),
δ_e	:	the electron inefficiency in E/p and TRD separation,
δ_π	:	the pion ineficiency in E/p separation,

Table 4.1 lists the values for the Eq. 4.1 and their descriptions.

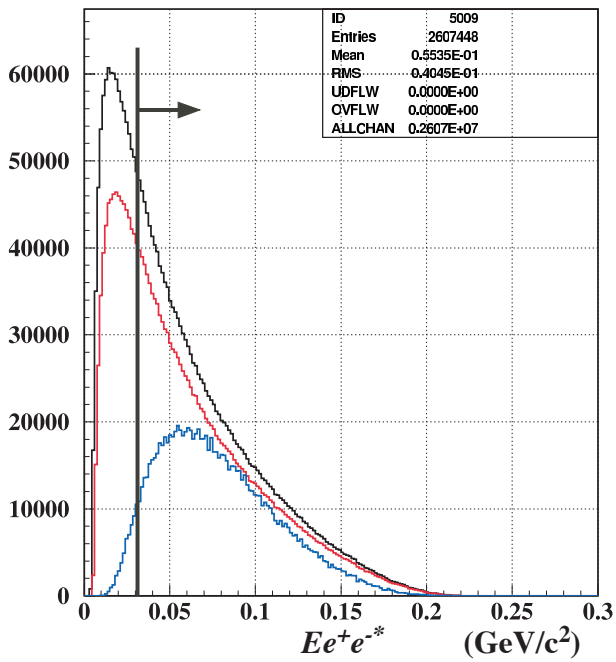

Figure 4.1: The $E^*_{e^+e^-}$ distribution of $K_L \to \pi^{\pm} e^{\mp(}\bar{\nu}^{)} e^+ e^-$ decays by χPT-NLO(p^4). Black histogram: for the events generated with $M_{e^+e^-}$ greater than 0.004 GeV/c^2, red histogram: for events generated with $M_{e^+e^-}$ greater than 0.005 GeV/c^2, and blue histogram: for the accepted events by the final cuts, multiplied by 12. The vertical line shows the 0.03 GeV cut-off boundary.

4.2 Results of branching fraction

The branching fraction is:

$$\begin{aligned} &BR[K_L \to \pi^{\pm} e^{\mp} \nu e^+ e^-; M_{e^+e^-} > 0.005 \text{ GeV/c}^2, E^*_{e^+e^-} > 0.03 \text{ GeV}] \\ &= [1.285 \pm 0.010(\text{stat}_{\text{signal}}) \pm 0.002(\text{stat}_{\text{norm}})] \times 10^{-5}, \end{aligned} \tag{4.2}$$

where $\text{stat}_{\text{signal}}$ and $\text{stat}_{\text{norm}}$ are the statistical errors from the signal mode analysis and the normalization mode analysis, respectively. The systematic errors are discussed in the next section.

4.3 Systematic uncertainties of the branching fraction

Table 4.2 lists the systematic uncertainties that we have considered. In the following subsections, we discuss each uncertainty.

Table 4.1: A list of values to determine the branching fraction. (for *winter '97*)

Element	Value	Section	description
$N_{\rm sig}$	20225	3.3	Accepted signal events including the backgrounds.
$\sum_i N_{{\rm BGsig}i}$	1019.2 ± 24.8	3.3	The number of estimated background.
A_{ke3ee}	$(8.9858 \pm 0.0249) \times 10^{-3}$	3.3	Acceptance of $K_L \to \pi^{\pm} e^{\mp} \overset{(}{\bar{\nu}}{}^{)} e^+ e^-$.
N_{ke3ee}	151318.14		Accepted MC events in final cuts.
G_{ke3ee}	29693160		The number of generated events in $M_{ee} > 4$ MeV/c^2.
R_{cutoff}	0.56712 ± 0.00058		Generated signal event ratio in $M_{ee} > 5$ MeV/c^2, $E^*_{ee} > 30$ MeV to $M_{ee} > 4$ MeV/c^2.
K'_{flux}	$(1.6764 \pm 0.0036) \times 10^{11}$	3.4	Uncorrected kaon flux.
Detecttion inefficiency corrections		Discrepancies of inefficiency between data-MC.	
$\delta_{e,E/p}$	+0.0034	3.1.2	Electron inefficiency in E/p selection.
$\delta_{e,TRD}$	+0.0035	3.1.2	Electron inefficiency in TRD selection.
$\delta_{\pi,E/p}$	+0.00243	3.1.2	Pion inefficiency in E/p selection.

Unobserved photon in the normalization analysis

As discussed in 3.4.3, we have measured the kaon flux without using photon information. To estimate the uncertainty arising from this fact, we also have measured the kaon flux by fully reconstructing the decay including photon.

Figure 4.2 (a) and 4.2 (b) show the data-MC comparison of the invariant mass distribution of $\pi^+\pi^-e^+e^-\gamma$ and $e^+e^-\gamma$, respectively.

There are large discrepancies between data and MC on both $M_{\pi\pi ee\gamma}$ and $M_{ee\gamma}$. To avoid these effects, we widened the acceptable regions and studied how the measured kaon flux depends on the cuts on $M_{\pi\pi ee\gamma}$ and $M_{ee\gamma}$, respectively. The results are shown in Fig. 4.3. In the plots, the number of background events were also re-estimated with the same varied cuts. We estimate that the systematic uncertainty on the kaon flux measured in the full reconstruction is +0.4%.

As summarized in Table 4.3, the measured uncorrected-kaon flux is $(1.6764 \pm 0.0036) \times 10^{11}$

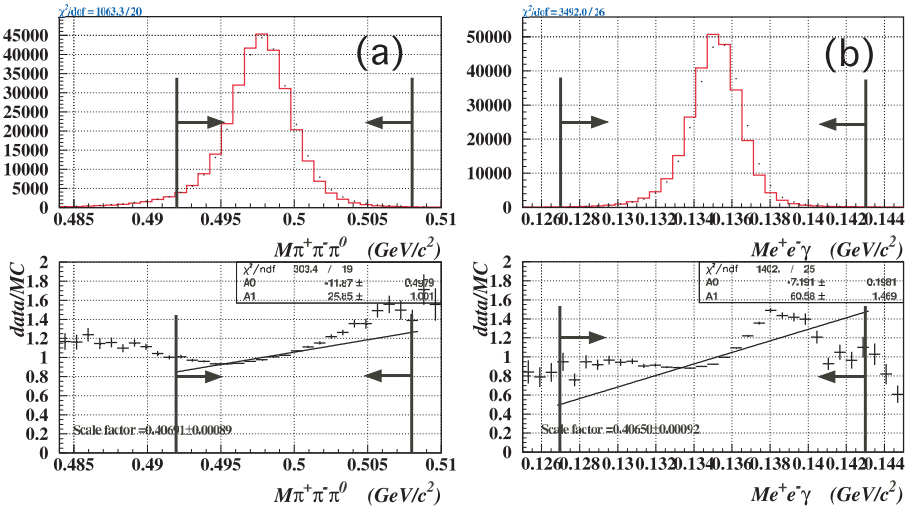

Figure 4.2: Comparison of the invariant mass distributions of $\pi^+\pi^-e^+e^-\gamma$ system (a) and $e^+e^-\gamma$ system (b) in the normalization mode analysis. Dots are data and histogram is MC. The data-to-MC ratios shown below are fit to a straight line. The vertical lines and arrows show the accepted regions for $K_L \to \pi^+\pi^-\pi^0_D$ candidates (0.492 GeV/c^2 $< M_{\pi\pi ee}\gamma <$ 0.508 GeV/c^2, 0.127 GeV/c^2 $< M_{e^+e^-}\gamma <$ 0.143 GeV/c^2) .

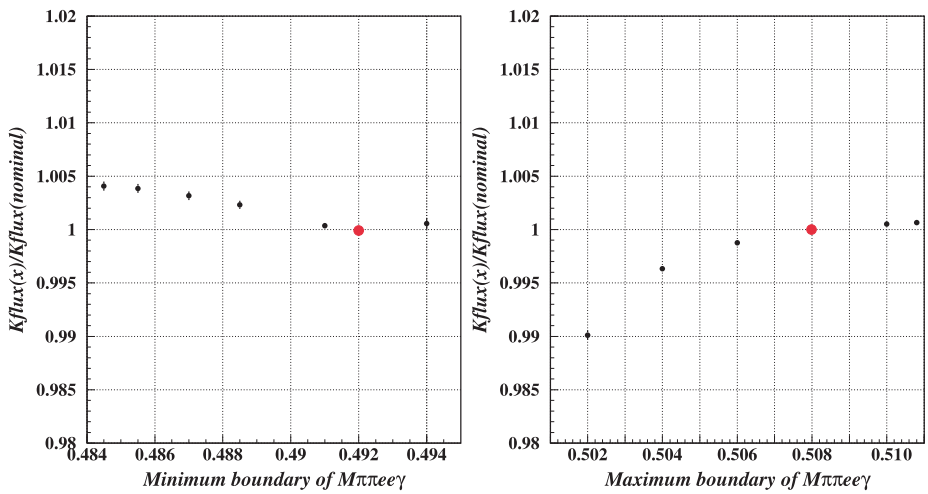

Figure 4.3: For the fully reconstructed normalization analysis, left (right) plot shows the deviations of estimated kaon flux as a function of the lower (higher) boundary of the invariant mass of $\pi^+\pi^-e^+e^-\gamma$ system. The kaon flux on the vertical axis is normalized by the kaon flux with final cut value of $M_{\pi\pi ee\gamma}$.

Table 4.2: Systematic uncertainties in the $K_L \to \pi^{\pm} e^{\mp(}\bar{\nu}^{)} e^+ e^-$ branching fraction.

Source of uncertainty	Uncertainty on BR($K_L \to \pi^{\pm} e^{\mp(}\bar{\nu}^{)} e^+ e^-$)(%)
Unobserved photon in normalization analysis	$\pm$ 1.03
vertex $\chi^2 cut$	$\pm$ 0.7
Radiative corrections	$\pm$ 0.51
$\pi^{\pm}$ loss in TRD	$\pm$ 0.45
E_K distribution	$\pm$ 0.35
Cut-off on the $M_{e^+e^-}$	$-$ 0.18
$e^{\pm}$ inefficiency in E/p	$\pm$ 0.09
$e^{\pm}$ inefficiency in TRD	$\pm$ 0.06
$\pi^{\pm}$ inefficiency in E/p	$\pm$ 0.03
Background estimation	
- $K_L \to \pi^{\pm} e^{\mp(}\bar{\nu}^{)} \gamma$ background	$\pm$ 0.04
- $K_L \to \pi^+ \pi^- \pi^0_D$ background	$\pm$ 0.02
- $K_L \to \pi^+ \pi^- \pi^0_{\gamma\gamma}$ BG for normalization	$\pm$ 0.03
MC statistics	
- $K_L \to \pi^{\pm} e^{\mp(}\bar{\nu}^{)} e^+ e^-$	$\pm$ 0.27
- Normalization mode	$\pm$ 0.12
- Backgrounds	$\pm$ 0.13
Total of internal uncertainties	$\pm$ 1.51
External uncertainty	$\pm$ 2.73
Total of systematic uncertainties	$\pm$ 3.21

with $\pi^+\pi^-e^+e^-$ sample, and $(1.6517 \pm 0.0077) \times 10^{11}$ with the full-reconstruction sample.

There is a 0.88% discrepancy on the estimated kaon flux between $\pi^+\pi^-e^+e^-$ analysis and Full-reconstruction analysis. With the cut variations on the $M_{\pi\pi ee\gamma}$ and $M_{ee\gamma}$, we estimate that the systematic error on the kaon flux based on the full-reconstruction study is $\pm$0.97%. With the influence of this uncertainty on the ratio of the number of signal events and the background events, we assign $\pm$1.03% as a systematic error of the $K_L \to \pi^{\pm} e^{\mp(}\bar{\nu}^{)} e^+ e^-$ branching fraction due to the uncertainty in the kaon flux.

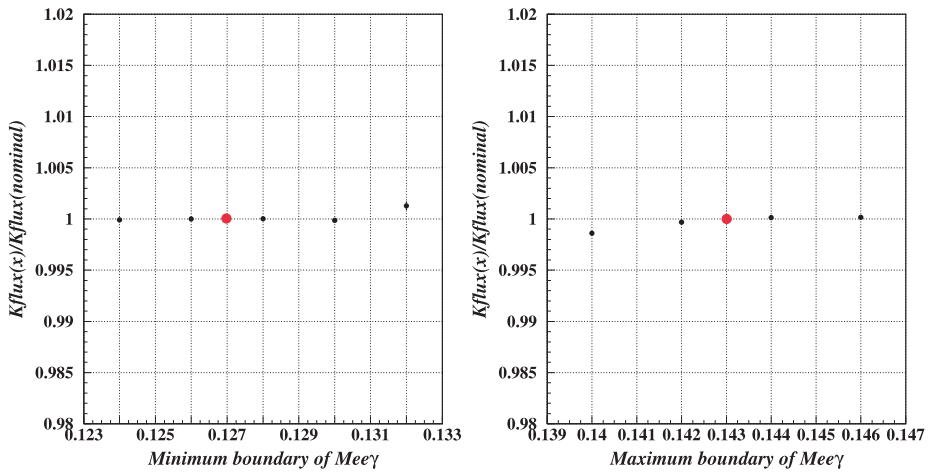

Figure 4.4: For the fully reconstructed normalization analysis, left (right) plot shows the deviations of estimated kaon flux as a function of the lower (higher) boundary of the invariant mass of $e^+e^-\gamma$ system. The kaon flux on the vertical axis is normalized by the kaon flux with final cut value of $M_{ee\gamma}$.

Table 4.3: The number of $K_L \to \pi^+\pi^-\pi^0_D$ events and background event for $\pi^+\pi^-e^+e^-$ analysis and full-reconstruction analysis

Decay mode	$\pi^+\pi^-e^+e^-$ sample	Fully reconstructed sample
$K_L \to \pi^+\pi^-\pi^0_D$ including BG	312707	274473
Acceptance of $K_L \to \pi^+\pi^-\pi^0_D$	$(4.9468 \pm 0.0088) \times 10^{-3}$	$(4.3868 \pm 0.0084) \times 10^{-3}$
Acceptance of BG	$(3.363 \pm 0.033) \times 10^{-7}$	$(2.190 \pm 0.026) \times 10^{-7}$
K'_{flux}	$(1.6764 \pm 0.0036) \times 10^{11}$	$(1.6617 \pm 0.0077) \times 10^{11}$

The vertex χ^2 cut

The tail in the vertex χ^2 distribution is not simulated well. Figure 4.5 (a) shows that the tail is not from either the $\Xi \to \Lambda(\to p\pi^-)\pi^0_D$ decay nor the double $K_L \to \pi^{\pm}e^{\mp(}\bar{\nu}^{)}$ decay. Remaining possibility for this tail is caused by the difficulty to simulate the scatterings in the detector [8, 33]. Therefore, we cannot cut-off this tail.

Fig 4.5 (b) shows the variation in the number of signal events after the acceptance correction, and the branching fraction as a function of the cut on vertex χ^2. The variation on the branching fraction is smaller because some of the effects cancel between the signal and normalization decay modes. However, it is not complete, because the signal mode and

normalization mode have different kinematics. Based on this plot, we assign a systematic error of ±0.7% due to the mismatch in vertex χ^2 distribution.

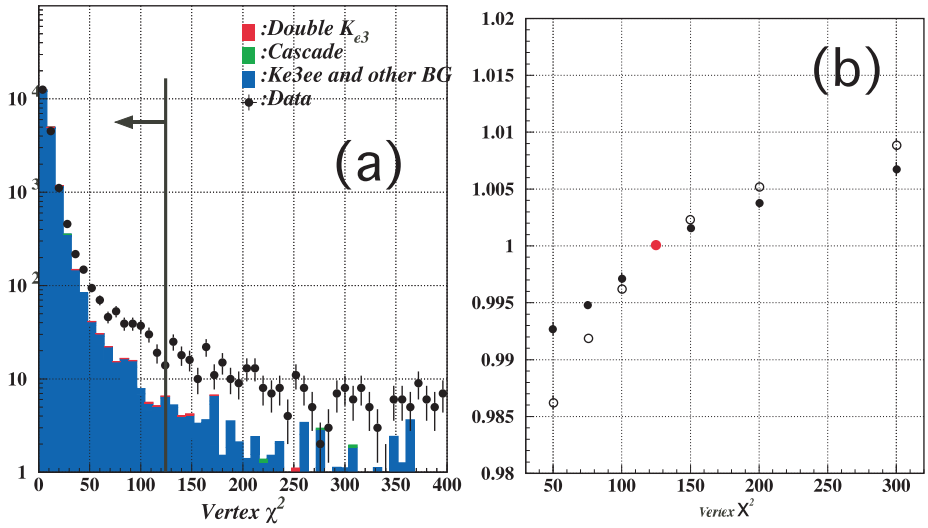

Figure 4.5: (a) The vertex χ^2 distribution. (b) The normalized number of accepted $K_L \to \pi^{\pm}e^{\mp(}\bar{\nu}^{)}e^+e^-$ after the acceptance correction (open circles) and the normalized branching fraction of $K_L \to \pi^{\pm}e^{\mp(}\bar{\nu}^{)}e^+e^-$(closed circles) shown as a fucnction of χ^2_{vtx} cut. The vertical line and arrow show the accepted region for $K_L \to \pi^{\pm}e^{\mp(}\bar{\nu}^{)}e^+e^-$ candidates ($E_K$max < 200 GeV) .

The radiative corrections

The $K_L \to \pi^{\pm}e^{\mp(}\bar{\nu}^{)}e^+e^-$ mode has four charged particles in its final state. The inner bremsstrahlung from these charged particles can affect the signal acceptance. For example, these photons modify the energy of other clusters in the CsI calorimeter, and the radiative photons change the kinematics of charged particles in the decay.

The bremsstrahlung photons were simulated in the MC generator using PHOTOS. In order to evaluate how well the inner bremsstrahlung is simulated with PHOTOS, we studied the events in which real photons were positively identified. The events were selected with cuts listed in Table 4.4. Figure 4.6 (a) and (b) show the distributions of the photon energies, and the angle between the photon and $e^{\pm}_{ke3}$, respectively. These distributions agree between data and MC. Figure 4.6 (c) shows the minimum distance at the CsI ($\Delta R_{\gamma-\mathrm{brem}}$) between the photon candidate, and the projected position of upstream electron tracks that is usually hit by external bremsstrahlung. Although the data/MC ratio of $\Delta R_{\gamma-\mathrm{brem}}$ has a significant

slope (3 σ), the fact that the the reduced χ^2 of data-MC comparison is 1.0 indicates that the distribution totally agrees between data and MC. To reject the events with the external bremsstrahlung occurring upstream of analysis magnet, we required that events have $\Delta R_{\gamma-\mathrm{brem}} > 0.02$ m. However, detailed simulations for such phenomena with materials are difficult.

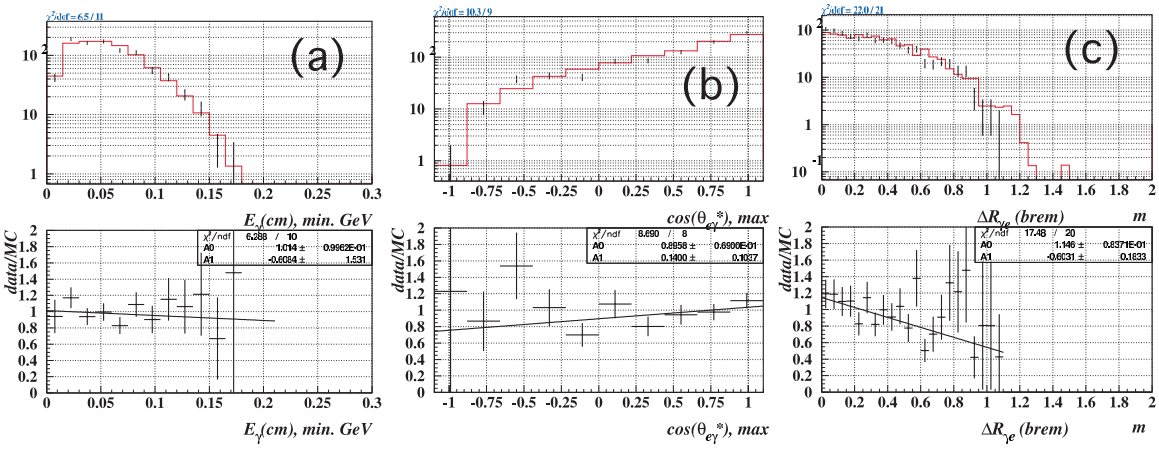

Figure 4.6: Data-MC comparisons for the events in which one photon was detected. (a) The energy distribution of photon candidates in the rest frame of the kaon with the minimum solution. (b) The distribution of $\cos(\theta^*_{e\gamma})$ in the kaon rest frame, where $\theta^*_{e\gamma}$ is the angle between the $e^{\pm}_{ke3}$ and the photon in the rest frame of the kaon with maximum solution. (c) The minimum distance between the photon candidate at the CsI and the projected position of electron track from upstream of the magnet.

The difference in the number of events detected with a photon in MC is $(6 \pm 8)\%$.

Compared to the MC without PHOTOS, the MC with PHOTOS increased the measured $BR(K_L \to \pi^{\pm} e^{\mp} \nu e^{+} e^{-})$ by 3.6%. Assuming that the effect of radiation on the $BR(K_L \to \pi^{\pm} e^{\mp} \nu e^{+} e^{-})$, δ_{rad}, is proportional to the number of observed photons, the deviation of the observed photon between data and MC, $6 \pm 8\%$, provides the 0.51% as a systematic error on the branching fraction.

Pion hadron interactions in TRD

As discussed in Sec. 2.6.5, all pion candidates was weighted by a probability of being lost in TRD due to π-hadron interaction. The weight was given as a function of pion energy and path length through the TRD. We assumed $\delta(\pi) = 10\%$ in Eq. 2.5 as an error from

Table 4.4: Selection criteria for the $K_L \to \pi^{\pm} e^{\mp(} \bar{\nu}^{)} e^{+} e^{-} \gamma$ decay with positively identified a photon.

Criterion	Description
$E_\gamma > 3$ GeV	:the energy of photon in the laboratory.
$E^*_\gamma < 0.18$ GeV	:the energy of photon in the center of kaon mass system.
$\Delta R_{\gamma-\pi} > 0.3$ m	:the distance between photon cluster and pion cluster.
$\Delta R_{\gamma-e^{\pm}} > 0.1$ m	:the distance between photon cluster and nearest cluster of electron.
$\Delta R_{\gamma-\mathrm{brem}} > 0.02$ m	:see text.
Shape $\chi^2 < 20$	:a variable to determine the photon likelihood for the cluster.
Timing $\chi^2 < 10$	:χ^2 of timing of all CsI blocks in the cluster.
Cluster point must be at least 25 mm away from the edge of beam hole.	
Cluster point must be at least 50 mm away from the outside edge of calorimeter.	
Cluster energy deposited before the event must be consistent with pedestal.	
Cluster energy deposited in the first RF bucket must be well above pedestal.	

the GEANT simulation. Consequently, we estimate the ±0.45% of systematic error on the branching fraction, due to the uncertainty of the missing ratio of pions by pion-hadron interaction.

The kaon energy distribution

As discussed in Sec. 2.6.1, the kaon energy distribution was tuned in two steps (E832-tuning and E799-tuning). To measure the branching fraction of the $K_L \to \pi^{\pm} e^{\mp(} \bar{\nu}^{)} e^{+} e^{-}$ decay, we used the kaon energy distribution with the final tuning, i.e., E799-tuning. However, the reason of the deviation of kaon energy distribution by applying E832-tuning to E799-analysis is not understood. Therefore, we also measured the BR($K_L \to \pi^{\pm} e^{\mp(} \bar{\nu}^{)} e^{+} e^{-}$) with the kaon energy distribution by E832-tuning. The branching fraction shifted by 0.35%, and thus we assign ±0.35% as the systematic error on the BR($K_L \to \pi^{\pm} e^{\mp(} \bar{\nu}^{)} e^{+} e^{-}$) due to the deviation of kaon energy between E832-tuning and E799-tuning.

The $M_{e^+e^-}$ cut-off at 0.005 GeV/c^2

We generated the $K_L \to \pi^{\pm} e^{\mp(}\bar{\nu}^{)} e^{+} e^{-}$ MC events with the $M_{e^+e^-}$ greater than 0.004 GeV/c^2. This lower limit is 0.001 GeV/c^2 smaller than the cut-off value in the analysis. If the $M_{e^+e^-}$ resolution is large, the fact that MC does not have events with $M_{e^+e^-}$ less than 0.004 GeV/c^2 affects the $M_{e^+e^-}$distribution above 0.005 GeV/c^2.

According to MC, 1.1% of events generated with $M_{e^+e^-}$ between 0.004 GeV/c^2 and 0.00405 GeV/c^2 are reconstructed in $M_{e^+e^-} >$ 0.005 GeV/c^2. In order to estimate the total number of events coming into signal region ($M_{e^+e^-} >$ 0.005 GeV/c^2) from $M_{e^+e^-} <$ 0.004 GeV/c^2, we extrapolated the $M_{e^+e^-}$ spectrum between 0.004 GeV/c^2 and 0.005 GeV/c^2 linearly to the region $M_{e^+e^-} <$ 0.004 GeV/c^2, and integrated the spectrum of events in the signal region from the $M_{e^+e^-} <$ 0.004 GeV/c^2 region. The shape of integrand in the signal region was estimated as a simple tri-angle approximated by the MC events generated between 0.004 GeV/c^2 and 0.00405 GeV/c^2. From the $M_{e^+e^-} <$ 0.004 GeV/c^2 region, 0.10% of total signal events has come into the signal region.

To determine this error directly from data, we measured the data-MC raito of $M_{e^+e^-}$ distribution focusing around 0.005 GeV/c^2. As shown in Fig. 4.7, the values are normalized by the ratio averaged between 0.005 GeV/c^2 to 0.006 GeV/c^2. The positive slope shown in Fig. 3.6 (c) is negligible for this discussion; change in of $M_{e^+e^-}$from 0.004 to 0.007 GeV/c^2 corresponds to 0.004 in y axis of Fig. 4.7. The effect that MC does not have events in $M_{e^+e^-} <$ 0.004 GeV/c^2 is apparent in the region below 0.005 GeV/c^2. We assume that a down slope from 0.004 to 0.0054 GeV/c^2 on the plot is the effect from events generated with $M_{e^+e^-} <$ 0.004 GeV/c^2. The events which have the $M_{e^+e^-}$ from 0.005 GeV/c^2 to 0.0054 GeV/c^2 are (4.28 ± 0.15)% of whole accepted events, and 4% of uncertainty par $dM_{e^+e^-}$ 0.0004 GeV/c^2 on the plot. Consequently, we estimate the -0.17% systematic error of $BR(K_L \to \pi^{\pm} e^{\mp} \nu e^{+} e^{-})$ due to the fact that there is no event with $M_{e^+e^-} <$ 0.004 GeV/c^{2}in MC.

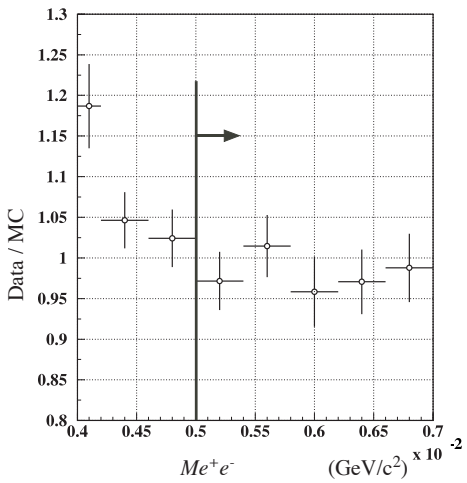

Figure 4.7: The data-MC ratio of the number of accepted events shown as a function of $M_{e^+e^-}$. The values are normalized by the ratio averaged in the region between 0.005 and 0.006 GeV/c^2.

Electron and pion inefficiencies of E/p separation and TRD separation

In Sec. 3.1.2, we have introduced the correction factors caused by the data-MC discrepancy in electron and pion detection inefficiencies in E/p separation, and TRD measurement. The uncertainties on the correction factors for these discrepancies are listed in Table 4.2.

Background estimations

The largest uncertainty in the background estimation comes from the amount of detector materials, which drives the photon conversion probability. According to the previous studies in KTeV E799-II experiment [34, 22], the uncertainty in the conversion rate is 5%. This uncertainty introduces a systematic error on the number of $K_L \to \pi^\pm e^\mp {}^{(}\bar{\nu}^{)} e^+ e^-$ events; $\pm 0.04\%$ for the $K_L \to \pi^\pm e^\mp {}^{(}\bar{\nu}^{)} \gamma$ background, and $\pm 0.02\%$ for the $K_L \to \pi^+\pi^-\pi^0_D$ background. It also introduces $\pm 0.03\%$ uncertainty in the number of $K_L \to \pi^+\pi^-\pi^0_D$ events for the normalization analysis by changing the number of $K_L \to \pi^+\pi^-\pi^0_{\gamma\gamma}$ background events with photon conversion.

The statistical uncertainties from the number of background MC events are listed under another category (MC statistics) in Table 4.2. The uncertainty on $BR(K_L \to \pi^\pm e^\mp \nu e^+ e^-)$

due to the errors on the branching fractions of the background decay modes are categorized as "external uncertainties" in Table 4.5.

Data-MC discrepancy on $M_{e^+e^-}$

If the acceptance of the $K_L \to \pi^{\pm} e^{\mp(}\bar{\nu}^{)} e^+ e^-$ events varies rapidly with $M_{e^+e^-}$, the data-MC discrepancy in the $M_{e^+e^-}$ spectra introduces an uncertainty on the $BR(K_L \to \pi^{\pm} e^{\mp} \nu e^+ e^-)$. To estimate this uncertainty, we divided the $M_{e^+e^-}$ spectrum in ten bins, and calculated the branching fraction as:

$$\begin{aligned} &BR(K_L \to \pi^{\pm} e^{\mp} \nu e^+ e^-) \\ &\quad = \sum_k \frac{N^k_{\rm sig} - \sum_i N^k_{{\rm BGsig}i}}{A^k_{Ke3ee}} K'^{-1}_{flux} (1+\delta_e)(1+\delta_\pi)^{-1}, \end{aligned} \tag{4.3}$$

$$A^k_h = N^k_h / G^k_h, \tag{4.4}$$

where the superscript k represents the bin number for $M_{e^+e^-}$. The rest of the notations are the same as for Eq. 4.1 and 3.8.

The $BR(K_L \to \pi^{\pm} e^{\mp} \nu e^+ e^-)$ estimated with this formula is $(1.286 \pm 0.010) \times 10^{-5}$. Since this is consistent with the result obtained by Eq. 4.1, (1.281×10^{-5}), we do not assign a systematic error due to the data-MC discrepancy on $M_{e^+e^-}$.

External uncertainty

Table 4.5 lists the external uncertainties on the $BR(K_L \to \pi^{\pm} e^{\mp} \nu e^+ e^-)$, caused by the uncertainties on the branching fraction of normalization and backgrounds decay modes.

Table 4.6 lists the value, error and origin of the branching fractions used to calculate the errors on the $K_L \to \pi^{\pm} e^{\mp(}\bar{\nu}^{)} e^+ e^-$ branching fraction. The external systematic error on $BR(K_L \to \pi^{\pm} e^{\mp} \nu e^+ e^-)$ from the branching fractions totally becomes $\pm 2.73\%$.

Table 4.5: External uncertainty from each branching fraction error.

Decay mode	Uncertainty on BR($K_L \to \pi^{\pm}e^{\mp(}\bar{\nu}^{)}e^+e^-$)(%)
$K_L \to \pi^+\pi^-\pi^0_D$	$\pm$ 2.73
$K_L \to \pi^{\pm}e^{\mp}\nu\pi^0_D$	$\pm$ 0.06
$K_L \to \pi^+\pi^-\pi^0_{4e}$	$\pm$ 0.09
$K_L \to \pi^{\pm}e^{\mp(}\bar{\nu}^{)}$	$\pm$ 0.00
$\Xi \to \Lambda(\to p\pi^-)\pi^0_D$	$\pm$ 0.00
Total	$\pm$ 2.73

Table 4.6: The original branching fractions.

Decay mode	Branching fraction	Citation
$K_L \to \pi^+\pi^-\pi^0$	0.1252 ± 0.007	KTeV(2004)[32]
$K_L \to \pi^{\pm}e^{\mp}\nu\pi^0$	$(5.20 \pm 0.11) \times 10^{-5}$	PDG 2006 [29]
$K_L \to \pi^{\pm}e^{\mp(}\bar{\nu}^{)}$	0.4067 ± 0.0011	KTeV(2004)[32]
$\pi^0 \to e^+e^-\gamma$	$(1.198 \pm 0.032) \times 10^{-2}$	PDG 2006 [29]
$\pi^0 \to e^+e^-e^+e^-$	$(3.14 \pm 0.30) \times 10^{-5}$	PDG 2006 [29]
$\pi^0 \to \gamma\gamma$	0.98798 ± 0.00032	PDG 2006 [29]
$\Xi \to \Lambda\pi^0$	0.99523 ± 0.00013	PDG 2006 [29]
$\Lambda \to p\pi^-$	0.639 ± 0.005	PDG 2006 [29]

4.4 Summary of the branching fraction of $K_L \to \pi^{\pm}e^{\mp(}\bar{\nu}^{)}e^+e^-$

To conclude, the $BR(K_L \to \pi^{\pm}e^{\mp}\nu e^+e^-)$ with statistical and systematic errors is:

$$\begin{aligned} &BR[K_L \to \pi^{\pm}e^{\mp}\nu e^+e^-; M_{e^+e^-} > 0.005 \text{ GeV/c}^2, E_{e^+e^-} > 0.03 \text{ GeV}] \\ &\quad = [1.281 \pm 0.010(stat) \\ &\qquad \pm 0.019(syst) \pm 0.035(syst_{external})] \times 10^{-5}. \end{aligned} \tag{4.5}$$

Chapter 5

Evaluation of χPT[NLO(p^4)]

5.1 The branching fraction of $K_L \to \pi^\pm e^{\mp(}\bar{\nu}^{)} e^+ e^-$ by χPT

Tsuji has calculated the ratio:

$$\mathcal{R} \equiv \frac{\Gamma(K_L \to \pi^\pm e^\mp \nu e^+ e^-; M_{e^+e^-} > 0.005\mathrm{GeV}/c^2)}{\Gamma(K_L \to \pi^\pm e^\mp \nu)}, \quad \text{and} \tag{5.1}$$

$$\mathcal{R}_{\mathrm{NLO}} = 4.29 \times 10^{-5} \tag{5.2}$$

with NLO(p^4) correction.

With his amplitude, we calculated the ratio $\mathcal{R}$ without NLO(p^4) as :

$$\mathcal{R}_{\mathrm{LO}} = 4.06 \times 10^{-5}. \tag{5.3}$$

Our measured $\mathcal{R}$ with the BR($K_L \to \pi^\pm e^{\mp(}\bar{\nu}^{)}$)$= 0.4067 \pm 0.0011$ [32] is:

$$\mathcal{R}_{\mathrm{exp}} = (4.54 \pm 0.15) \times 10^{-5}. \tag{5.4}$$

Ignoring any theoretical uncertainties, the measured $\mathcal{R}$ agrees with the NLO(p^4) calculation within 1.7 σ, while it is 3.2 σ larger than the LO calculation.

5.2 Comparisons of spectra

As shown in Sec. 3.1.3 - 3.2.7, NLO(p^4) represents the nature of $K_L \to \pi^{\pm} e^{\mp(}\bar{\nu}^{)} e^+ e^-$ well, except for the $M_{e^+e^-}$ distribution. In this section we will show how the NLO(p^4) correction works on the LO by comparing data with two types of MC; one with LO and the other with NLO(p^4) calculations.

5.2.1 The square of the transition momentum

Spectrum

Figure 5.1 shows the data-MC comparison of the t/M_π^2 distribution for LO and NLO(p^4). The t/M_π^2 has a twofold ambiguity due to the kaon energy ambiguity, so we have two sets of t/M_π^2: t/M_π^2 calculated with the E_K maximum [$t/M_\pi^2(E_K$ max)] and t/M_π^2 calculated with the E_K minimum [$t/M_\pi^2(E_K$ min)]. The discrepancy between data and MC-LO is significant and the NLO(p^4) correction removes this discrepancy for both solutions.

However, we have two questions in Fig. 5.1:

1. Why is the *Slope* of the data / LO-MC ratio smaller than the theoretical NLO(p^4) / LO ratio shown in Fig. 1.4? In Fig. 1.4, the *Slope* corresponds to $\sim 5 \times 10^{-2}$, ~ 2 times larger than the *Slope* in Fig. 5.1 (a).

2. Why are the spectra different between $t/M_\pi^2(E_K$ max) and $t/M_\pi^2(E_K$ min)?

To answer these questions, we investigated further as described in Appendix G, and concluded as follows:

1. The square of the transition momentum t has a two-fold ambiguity due to the two-fold ambiguity of the energy of kaon. For a half of events, incorrect solution is chosen, and in that case, the *Slope* is smaller. Therefore, the *Slope* for the whole events is reduced from the true slope.

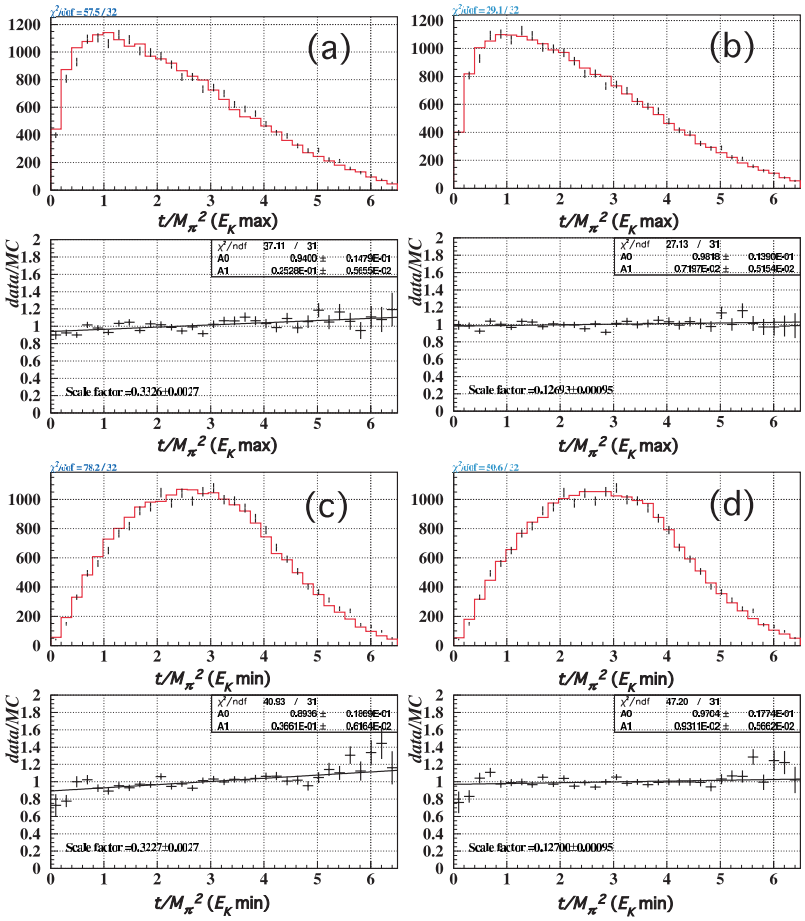

Figure 5.1: Comparisons of the t/M_π^2 distributions for data (dots) and MC (histogram). (a) $t/M_\pi^2(E_K$ max) with MC-LO, (b) $t/M_\pi^2(E_K$ max) with MC-NLO, (c) $t/M_\pi^2(E_K$ min) with MC-LO, and (d) $t/M_\pi^2(E_K$ min) with MC-NLO, The data-to-MC ratios on the bottom are fit to a straight line. The slope of the fitted line is $(2.53\pm0.57)\times10^{-2}$ for $t/M_\pi^2(E_K$ max) with MC-LO, $(0.72\pm0.52)\times10^{-2}$ for $t/M_\pi^2(E_K$ max) with MC-NLO, $(3.66\pm0.61)\times10^{-2}$ for $t/M_\pi^2(E_K$ min) with MC-LO, and $(0.93\pm0.57)\times10^{-2}$ for $t/M_\pi^2(E_K$ min) with MC-NLO. .

2. For the amplitude with virtual photon radiating from π, the transition momentum of the K-π current should be $Q \equiv P_K - P_\pi - q$, and $t = (Q+q)^2$, where P_K, P_π, and q are the 4-momenta of kaon, pion, and the virtual photon, respectively. Most of events have a small opening angle between γ^* and π, and it makes t much larger than Q^2. When the NLO correction has a certain positive dependence on Q^2, t dependence of NLO correction becomes smaller for those events. This effect becomes larger for larger $|\boldsymbol{q}|$, where $\boldsymbol{q}$ is the 3-momentum of q. Since high electron energies in e^+e^- pair are required in the experimental analysis, the t dependence on the NLO correction was reduced.

The other question on the t spectrum is the large difference of shapes of spectra between for E_K maximum solution and for E_K minimum solution. Requiring $E_{e^+}, E_{e^-} > 3$ GeV tends to collect the events having $e^{\pm}_{ke3}$ and the virtual photon going downstream, and pions going upstream in the kaon rest frame. This causes that the events which have neutrino going upstream in kaon rest frame ($P_\nu^{(-)}$), to have larger Q^2 than the events which have neutrino going downstream in the kaon rest frame ($P_\nu^{(+)}$). Consequently, the $P_\nu^{(-)}$ events provide larger t/M_π^2 for the minimum E_K solution, than the $P_\nu^{(+)}$ events providing t/M_π^2 for the maximum E_K solution. These process are also shown in Appendix G.

The low energy coupling constant L_9

The LO calculation for neutral kaon semileptonic decay has constant form factors, $f_+^{(2)} = 1$ and $f_-^{(2)} = 0$. In NLO(p^4) corrections, the higher order term of f_+ is [7]:

$$\begin{aligned} F_0^2 f_+^{(4)}(t) &= 2L_9^r t + 3/8\{A(m_\eta^2) + A(m_\pi^2) + 2A(m_K^2)\} \\ &\quad -3/2\{B_{22}(m_\pi^2, m_K^2, t) + B_{22}(m_\pi^2, m_\eta^2, t)\}. \end{aligned} \tag{5.5}$$

The amplitude has a noticeable t dependence through a low energy coupling constant, L_9^r. Contribution of f_- is small for the $K_L \to \pi^\pm e^{\mp(}\bar{\nu}^{)}$ physics because it is proportional to $M_e/M_k \simeq 10^{-6}$. Figure 5.2 (a) shows a comparison of t/M_π^2 distributions for MC simulations with $L_9^r = 6.9 \times 10^{-3}$ and $L_9^r = 0$. The t/M_π^2 distributions were made from the decay generator directly, the t/M_π^2 distribution does not have the two-fold ambiguity for the kaon energy. The $L_9^r = 6.9 \times 10^{-3}$ is the standard value that we used in our analysis [35]. The ratio of the t/M_π^2 distributions between the ones generated with $L_9^r = 6.9 \times 10^{-3}$ and $L_9^r = 0$ has a simple linear dependence on t.

Figure 5.2 (b) shows the slope of the linear t dependence as a function of L_9^r. The slope is proportional to L_9^r in the region $0 < L_9^r < 10 \times 10^{-3}$.

As shown in Fig. 5.3, the t/M_π^2 distribution with NLO(L_9^r= 0) is consistent with the t/M_π^2 distribution with LO. This fact indicates that the contribution of NLO(p^4) correction on t distribution is dominantly from the L_9^r term in χPT[NLO(p^4)].

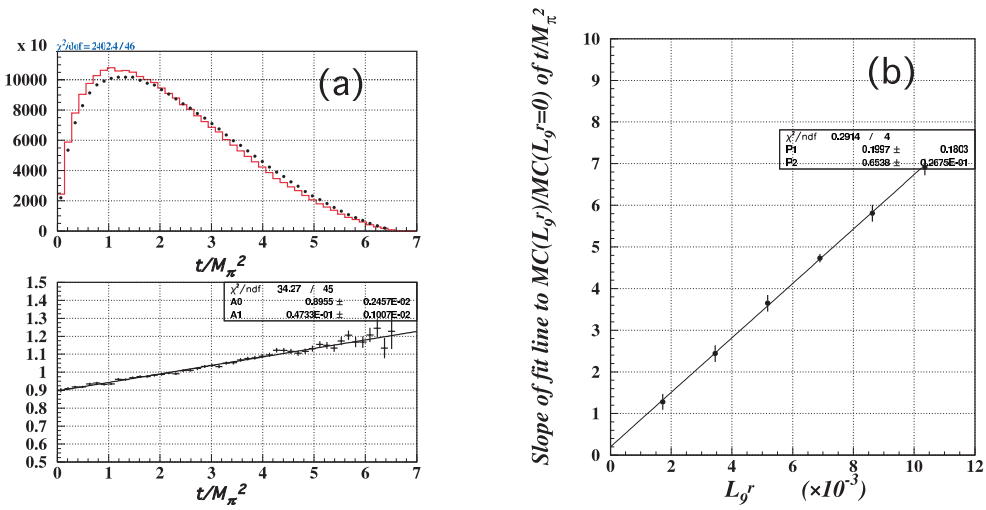

Figure 5.2: (a): A typical MC(L_9^r)/MC($L_9^r = 0$) comparison of t/M_π^2 distribution at L_9^r= 6.9×10^{-3}. The MC/MC ratio at the bottom is fit to a straight line from L_9^r=0 to L_9^r= 8.3×10^{-3}; Slope = $(4.73 \pm 0.10) \times 10^{-2}$. The MC simulations have been calculated without detector simulation. (b): Such slopes are plotted as a function of L_9^r.

Assuming that the linearity in the slope-L_9^r correlation remains in the reconstructed sample, we estimate the best L_9^r from our analysis using the following equation:

$$L_9^r(This\ exp.) = \frac{S^{Exp}_{data/MC(L_9^r=0)}}{S^{Exp}_{MC(L_9^r=6.9\times10^{-3})/MC(L_9^r=0)}} 6.9 \times 10^{-3}, \tag{5.6}$$

where $S_{data/MC(L_9^r=0)}$ is the slope of data/MC(NLO with $L_9^r = 0$) ratio for t/M_π^2 and $S_{MC(L_9^r=6.9\times10^{-3})/MC(L_9^r=0)}$ is the slope of MC(NLO with $L_9^r = 6.9 \times 10^{-3}$)/MC(NLO with $L_9^r = 0$)) ratio for t/M_π^2.

These slopes are listed in Table 5.1 for two kaon energy solutions. Using these slopes, we obtained:

$$L_9^r = (8.6 \pm 2.1) \times 10^{-3} \qquad \text{using the maxmum } E_K, \tag{5.7}$$

$$L_9^r = (8.0 \pm 1.6) \times 10^{-3} \qquad \text{using the minimum } E_K. \tag{5.8}$$

As discussed in the previous part in this Section and Appendix G, the t/M_π^2 distribution for E_K minimum solution is more sensitive to the NLO correction than for E_K maximum solution. Therefore, we choose the value of L_9^r for E_K minimum solution, $(8.0 \pm 1.6) \times 10^{-3}$

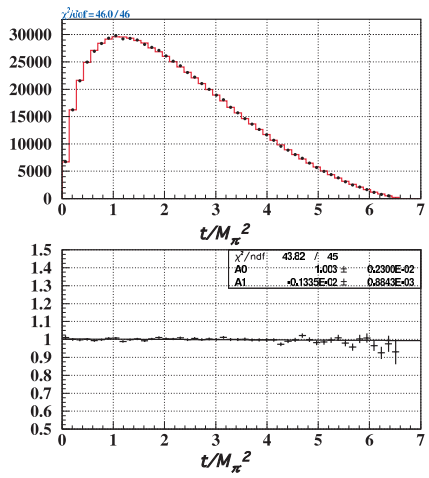

Figure 5.3: MC/MC comparison of $M_{e^+e^-}$ spectra between NLO with $L_9^r = 0$ and LO. The MC/MC ratio on the bottom is fit to a straight line; Slope $= (-0.13 \pm 0.09) \times 10^{-2}$.

Table 5.1: The slopes used to extract the L_9^r.

Slope (10^{-3})	for E_K max	for E_K min
$S_{data/MC(L_9^r=0)}$	2.76 ± 0.54	3.55 ± 0.59
$S_{MC(L_9^r=6.9\times10^{-3})/MC(L_9^r=0)}$	2.21 ± 0.30	3.06 ± 0.33

as our best value. Both values are consistent with the value in [35], $(6.9 \pm 0.7) \times 10^{-3}$.

Except for this section, we always use $L_9^r = 6.9 \times 10^{-3}$ for the NLO(p^4) MC.

5.2.2 The invariant masses

The invariant mass of $\pi^\pm e^\mp_{ke3}$ system is also sensitive to the NLO correction. Figure 5.4 shows the data-MC comparison of $\pi^\pm e^\mp_{ke3}$ spectrum for LO (a) and NLO (b). MC with NLO(p^4) is consistent with data, while the fitted line to the data-MC ratio for the MC with LO has a finite slope of 2.3 σ.

Figure 5.5 shows the significances of the slopes ($slope/\sigma_{slope}$) of data-to-MC ratio for t, and for the invariant masses of several decay product systems. For $M_{\pi^\pm e^\mp e^+e^-}$, $M_{\pi^\pm e^\mp}$. and t, the data disagrees significantly from MC(LO), but not from MC(NLO). The MC(LO) has a constant K-π form factor. The differences in $M_{\pi^\pm e^\mp e^+e^-}$, $M_{\pi^\pm e^\mp}$. and t come from the correction on K-π form factor by NLO(p^4). These phenomena indicate that χPT[NLO(p^4)]

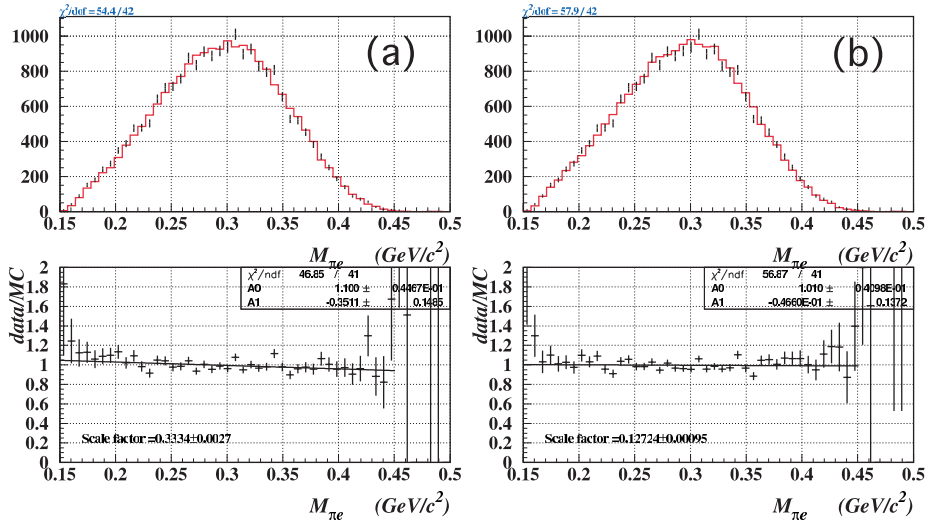

Figure 5.4: Comparison of the $M_{\pi e}$ distribution for data (dots) and MC (histogram) with LO on (a), and with NLO on (b). The data-to-MC ratios on the bottom are fit to a straight line. The slope of the fitted line for LO (NLO) is -0.35 ± 0.15 $(-0.05 \pm 0.14)(\mathrm{GeV/c^2})^{-1}$.

represents the K-π structure of the $K_L \to \pi^{\pm} e^{\mp(}\bar{\nu}^{)} e^+ e^-$ decay well. The invariant mass of the e^+e^- pair has discrepancies between data and MC with both LO and NLO. We will discuss this discrepancy in the following sections.

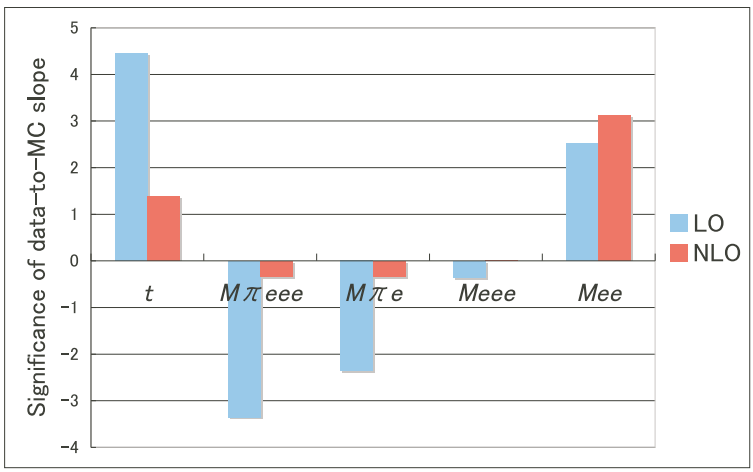

Figure 5.5: Significance of the slope ($slope/\sigma_{slope}$) of data-to-MC ratio for t and invariant masses;$M_{\pi^{\pm}e^{\mp}e^+e^-}$, $M_{\pi^{\pm}e^{\mp}}$, and $M_{e^{\pm}e^+e^-}$, and $M_{e^+e^-}$. Blue bars are for LO and red bars are for NLO .

5.3 Result on the invariant mass: $M_{e^+e^-}$

Figure 5.6 (a) shows a comparison of the $M_{e^+e^-}$ distribution between data and MC(LO), and Fig. 5.6 (b) shows the comparison between data and MC[NLO(p^4)]. We can see that the data to MC ratios have finite slopes for both LO and NLO(p^4). The significance of the slopes are 3 σ, when we fit in the region 0.005-0.1 GeV/c^2.

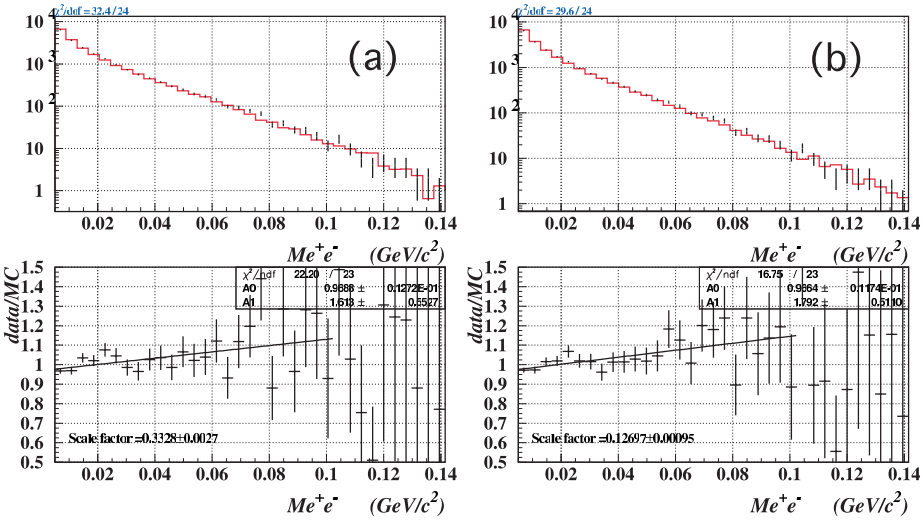

Figure 5.6: Comparison of the $M_{e^+e^-}$ distribution for data (dots) and MC (histogram) with LO (a), and NLO (b). The data-to-MC ratios shown below are fitted to a straight line. The slope of the fitted lines is 1.62 ± 0.55(GeV/c^2)$^{-1}$ for LO, and for NLO is 1.79 ± 0.51(for NLO. GeV/c^2)$^{-1}$.

5.4 Discussions on the $M_{e^+e^-}$

5.4.1 Possibility of a wrong estimation of backgrounds

First, we consider the possibility that the discrepancy of $M_{e^+e^-}$ is from a wrong estimation of background. Figure 5.7 shows that the $M_{e^+e^-}$ slope vanishes, if we double the number of all the background events. Table 5.2 lists the slopes of data-MC ratio, if we double the number of events for individual background.

Although doubling the $K_L \to \pi^+\pi^-\pi^0_D$ background is effective for fixing the $M_{e^+e^-}$ spectrum, we believe that our original background estimation is correct as described below.

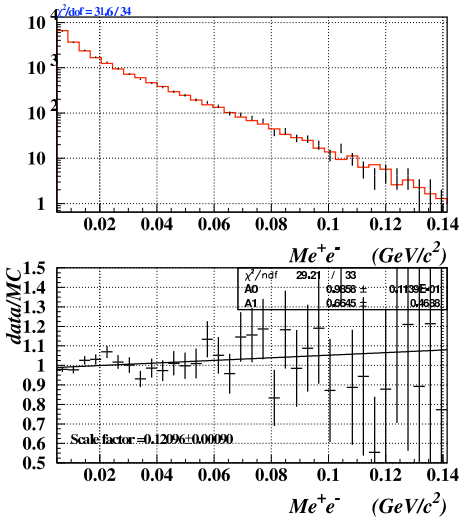

Figure 5.7: The slope of data-MC ratio of $M_{e^+e^-}$ vanishes when all backgrounds are doubled, Slope $= 0.3 \pm 0.5(\mathrm{GeV/c^2})^{-1}$.

Table 5.2: Relaxation of data-MC discrepancy by doubled backgrounds.

Doubled background	Slope (default=1.58 with NLO)
$K_L \to \pi^+\pi^-\pi^0_D$	0.84 ± 0.51
$K_L \to \pi^\pm e^\mp \nu \pi^0_D$	0.84 ± 0.51
$K_L \to \pi^+\pi^-\pi^0_{4e}$	1.20 ± 0.52
$K_L \to \pi^\pm e^\mp \overset{(-)}{\nu} \gamma$	1.59 ± 0.52

Figure 5.8 shows data-MC comparison for $P^{*2}_{\nu||}$ distribution. In this figure, the MC for $K_L \to \pi^+\pi^-\pi^0_D$ background has been doubled. The data-MC agreement remains for the $P^{*2}_{\nu||}$ distribution between 0 GeV^2/c^2 and 0.14 GeV^2/c^2, but the agreement is broken for $P^{*2}_{\nu||}$ greater than 0.14 GeV^2/c^2 due to the excess in background events from the $K_L \to \pi^+\pi^-\pi^0_D$ decays. Also, for $M_{e^\pm e^+e^-}$ distribution, the data-MC agreement on the peak at 0.13 GeV/c^2 [Fig. 3.9 (a)] is broken by doubling $K_L \to \pi^+\pi^-\pi^0_D$ background. Thus, we cannot double the number of background events from the $K_L \to \pi^+\pi^-\pi^0_D$ decays. The same phenomenon occurs by doubling $K_L \to \pi^+\pi^-\pi^0_{4e}$ background decay.

The $K_L \to \pi^\pm e^\mp \nu \pi^0_D$ background cannot be doubled, either. Figure 5.9 shows the distribution of the invariant mass of $e^+e^-\gamma$ system for data and the standard MC. The background MC's are normalized by the kaon flux and their branching fractions. The peak at the π^0

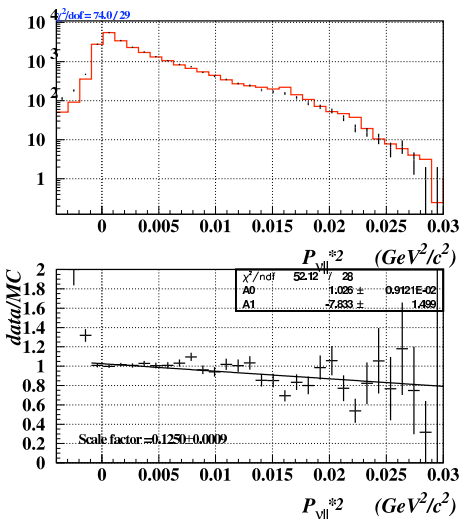

Figure 5.8: Comparison of the squared longitudinal neutrino momentum for data (dots) and MC (histogram). Background from $K_L \to \pi^+\pi^-\pi^0_D$ has been doubled. Doubled $K_L \to \pi^+\pi^-\pi^0_D$ clearly breaks the data-MC agreement especially at $P^{*2}_{\nu||} > 0.014$ GeV^2/c^2, .

mass is dominated by the Dalitz decay, $\pi^0 \to e^+e^-\gamma$ from the $K_L \to \pi^\pm e^\mp \nu \pi^0_D$ decay. Since the standard MC reproduces the height of the peaks, the size of the $K_L \to \pi^\pm e^\mp \nu \pi^0_D$ background is correct.

The remaining dominant background from $K_L \to \pi^\pm e^{\mp(}\bar{\nu}^{)}\gamma$ does not affect the $M_{e^+e^-}$ distribution.

Consequently, it is difficult to consider that the $M_{e^+e^-}$ discrepancy is caused by a wrong estimation of backgrounds. A possibility that the $M_{e^+e^-}$ distribution is caused by an unknown background is also small, because it will most likely to change other kinematical distributions.

5.4.2 Possibility of incorrect detector simulations

Next, we will consider a possibility that the propagation of e^+e^- pair in the detector is not simulated correctly. In Fig. 3.15, we have compared the $M_{e^+e^-}$ distribution for the normalization mode, $K_L \to \pi^+\pi^-\pi^0_D$, between data and MC. The fact that the MC $M_{e^+e^-}$ distribution has a good agreement between data and MC shows that there is no big problem in the simulation. However, we further look into the possibility of errors in the detector

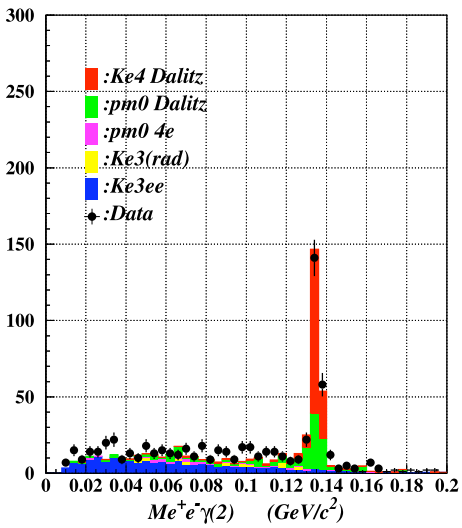

Figure 5.9: Distribution of the invariant mass of $e^+e^-\gamma$ system for the events detected with one photon. This plot shows that the background from $K_L \to \pi^\pm e^\mp \nu \pi^0_D$ is estimated properly.

simulations.

There is a fact that the opening angle of the e^+e^- pair ($\theta_{e^+e^-}$) is measured larger than the actual angle when the vertex is measured with the e^+e^- tracks alone. This phenomenon is caused by a fact that Z-vetex of e^+e^- pair has a tendency to be measured downstream of the actual position, as described in Appendix H. The effect is large when $\theta_{e^+e^-}$ is small, i.e., $M_{e^+e^-}$ is small. Figure 5.10 shows such a phenomenon on data. We consider a possibility that this difference of size of this asymmetry between data and MC remains even after our requirement of $M_{e^+e^-} > 0.005$ GeV/c^2, and causing the $M_{e^+e^-}$ problem.

The $M_{e^+e^-}$ has a range for a opening angle as shown in Fig. 5.11 (a). Therefore, we can investigate the opening angle dependence of $M_{e^+e^-}$ distribution. Figure 5.11 (b) shows the $M_{e^+e^-}$ distributions after requiring of $\theta_{e^+e^-} > 0.0015$ rad. This requirement on the opening angle effectively requires that two tracks are at least 15 mm apart from each other at DC1, so that the tracking has a good quality. Although this cut drastically changes the $M_{e^+e^-}$ distribution around 0.01 GeV/c^2, the slope in the data-MC ratio of $M_{e^+e^-}$ distribution is not affected.

We also investigated how the data-MC ratio of $M_{e^+e^-}$ depends on the Z-vertex. Figure 5.12

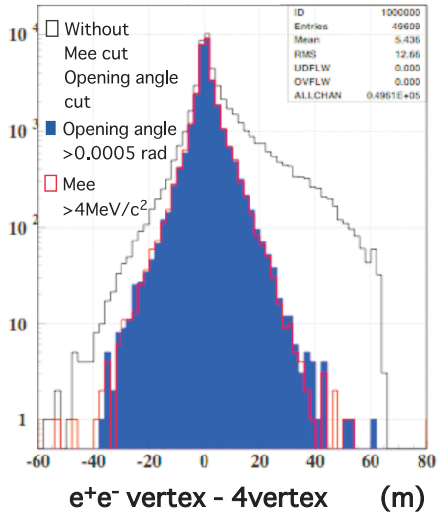

Figure 5.10: Distance between the vertex measured with the e^+e^- tracks and the vertex measured with four tracks. Open black histogram: without requirements on either $\theta_{e^+e^-}$ or $M_{e^+e^-}$. Blue histogram: $\theta_{e^+e^-} > 0.0005$ rad. Open red histogram: $M_{e^+e^-} > 0.004$ GeV/c^2.

(a) and (b) show the $M_{e^+e^-}$ distribution for the events with Z-vertex > 120 m and Z-vertex < 130 m, respectively. We can see that the slope of data-MC ratio remains in both sample.

If there are some unexpected magnetic fields, it can change the $M_{e^+e^-}$ distribution. To test this hypothesis, we separate the events in two categories; *out-bend* : electron and positron tracks separate from each other in the downstream of the analysis magnet, and *in-bend* : electron and positron tracks cross each other in the downstream of the analysis magnet. Figure. 5.13 shows an example case, where a magnetic field opposite to the analysis magnet exists between DC1 and DC2. $M_{e^+e^-}$ of the *in-bend* (*out-bend*) events tend to be measured larger (smaller) than the actual value. However, we will assure that the effects of those events are canceled each other.

Figure 5.14 shows the slopes of data-MC ratio of $M_{e^+e^-}$ distributions for the *out-bend* sample, the *in-bend* sample, and all the samples, under different conditions: i) MC with the default magnetic field, ii) MC with additional magnetic field which KTeV collaboration found for correction [36], and iii) same as ii), but with $\theta_{e^+e^-} > 0.0015$ rad requirement.

We can see that the difference of the slopes between *out-bend and in-bend* samples becomes

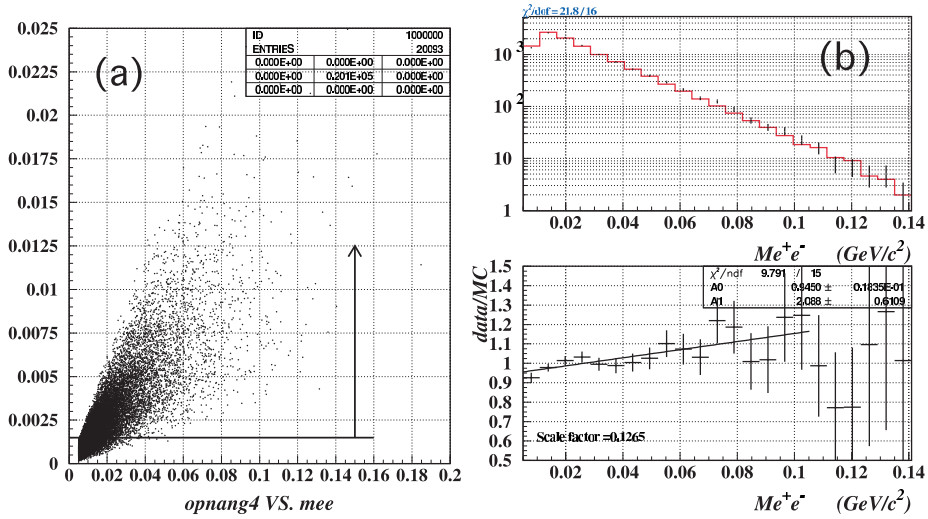

Figure 5.11: (a) Scatter plot of $\theta_{e^+e^-}$vs. $M_{e^+e^-}$ for data. For the events above the horizontal line, $\theta_{e^+e^-} > 0.0015$ rad., the $M_{e^+e^-}$ distribution is compared between data and MC in (b).

smaller with the field correction, and even smaller by requiring a large opening angle. However, the slope for the total sample does not depend on the above conditions. Therefore, there is extra magnetic field, but its effect is cancelled between *out-bend* and *in-bend* events.

Based on these results, we conclude that the discrepancy on the $M_{e^+e^-}$ distribution between data and MC is not caused by the extra magnetic field upstream of the analysis magnet.

5.4.3 Discussions on the theoretical model

We next look into the possibility of a defect in the theory. The positive slope of $M_{e^+e^-}$ may be caused by unknown or lacking term in the decay amplitude. For example, there could be a pole at the mass larger than 0.1 GeV/c^2 for virtual photon propagator. ←

Our $K_L \to \pi^\pm e^{\mp(}\bar{\nu}^{)} e^+e^-$ amplitude in the MC does not have the virtual radiative corrections, i.e., loop diagrams in QED. In case of $\pi^0 \to e^+e^-\gamma$, the virtual radiative corrections enhance the low $M_{e^+e^-}$, as we confirmed with MC. However, the effect on $K_L \to \pi^\pm e^{\mp(}\bar{\nu}^{)} e^+e^-$ decay should be calculated, because there are more charged particles in the $K_L \to \pi^\pm e^{\mp(}\bar{\nu}^{)} e^+e^-$ decay.

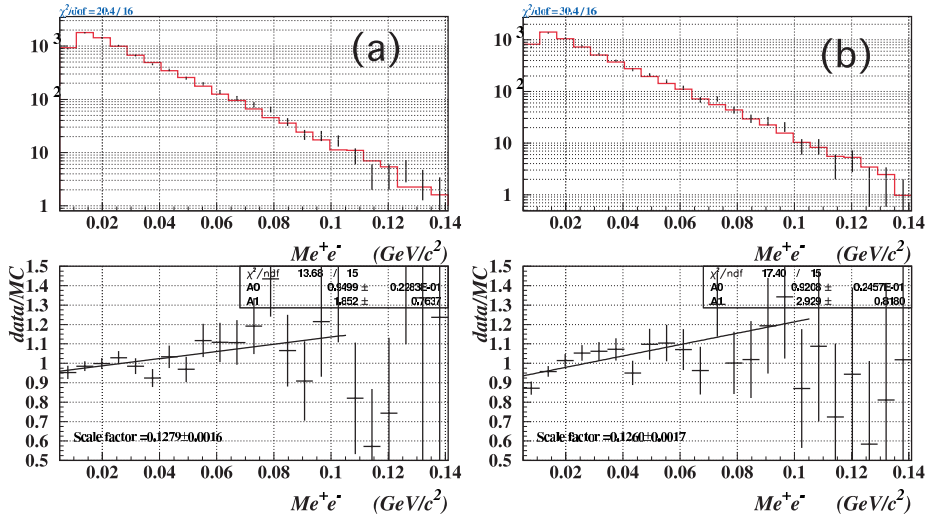

Figure 5.12: Comparison of the $M_{e^+e^-}$ distribution between data and MC for the events (a) with Z-vertex > 120 m and (b) with Z-vertex < 130 m.

The $K_L \to \pi^\pm e^{\mp(}\bar{\nu}^{)}(\gamma)$ decay is studied with χPT up to $\mathcal{O}(p^6)$ with virtual radiative corrections [37]. However, it is difficult to expect that $\mathcal{O}(p^6)$ corrections fix this problem, because there is no modification by NLO(p^4) to LO calculation.

Summary of discussions about $M_{e^+e^-}$

The slope in the $M_{e^+e^-}$ distribution is not caused by:

(a) wrong background estimations, or

(b) wrong particle propagation in the MC, or

(c) extra magnetic field.

Remaining possibility for the cause of the slope of $M_{e^+e^-}$ are:

(a) unknown process that it not included in the χPT, or

(b) missing virtual radiative correction.

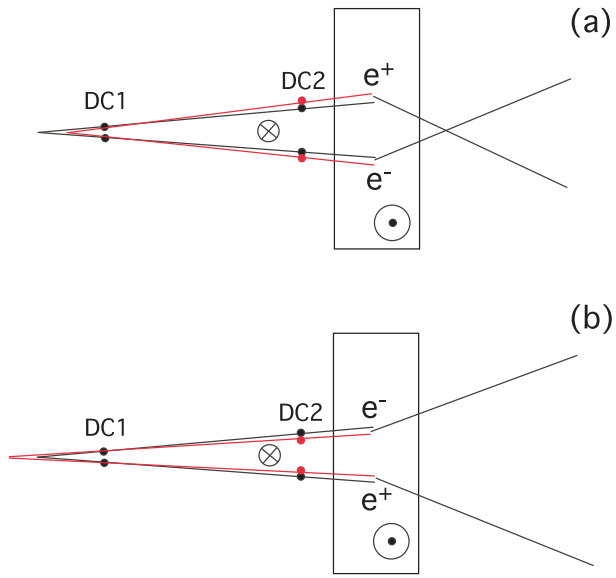

Figure 5.13: Illustration of an example that the $M_{e^+e^-}$ is measured larger than the actual mass [(a), in-bend)], and smaller than the actual mass [(b), out-bend)], by an unexpected field between DC1 and DC2. In this example, the unexpected field expressed by a circle points the opposite direction from the field in the analysis magnet. If there were no extra field, the upstream tracks would go along the black line. However with the extra filed, the field gives a curvature on each track. Consequently, we reconstruct the tracks along red lines.

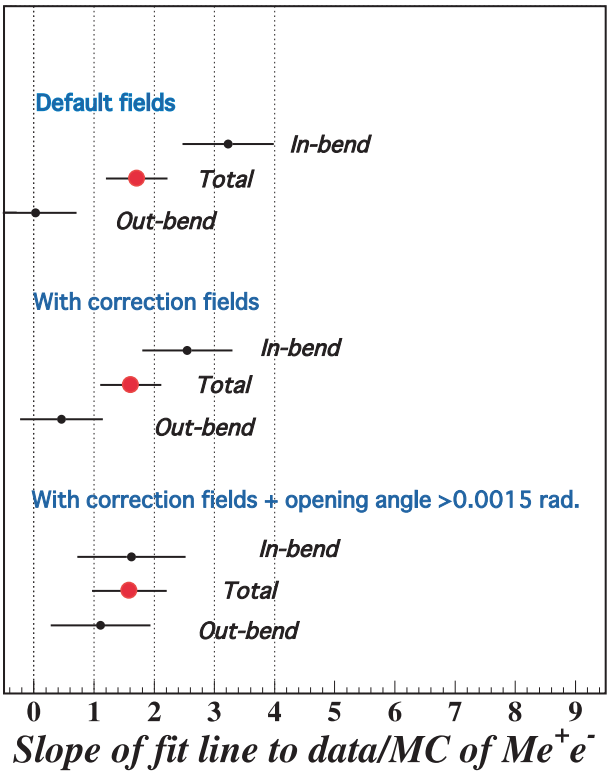

Figure 5.14: Data-MC slopes are different between the "in-bend and out-bend" events. With the extra field correction, the difference becomes smaller. For events with large opening angle, the difference vanishes. Regardless of the difference between the "in-bend and out-bend" events, the slopes with the total sample is unchanged.

Chapter 6

Conclusions

In this thesis, we report a measurement of the branching fraction of $K_L \to \pi^{\pm} e^{\mp(}\bar{\nu}^{)} e^+ e^-$:

$$\begin{aligned} BR[K_L \to \pi^{\pm} e^{\mp} \nu e^+ e^-;\, M_{e^+e^-} > 0.005 \text{ GeV/c}^2, E_{e^+e^-} > 0.03 \text{ GeV}] \\ = [1.281 \pm 0.010(\text{stat}) \pm 0.040(\text{syst})] \times 10^{-5} \\ = (1.281 \pm 0.041) \times 10^{-5}. \end{aligned} \tag{6.1}$$

This is the first world measurement of the branching fraction of $K_L \to \pi^{\pm} e^{\mp(}\bar{\nu}^{)} e^+ e^-$. The acceptance for the decay mode was calculated based on a chiral perturbation theory at order p^4 [χPT-NLO(p^4)] by Tsuji [7]. The 20225 signal events indicates the advantage of NLO(p^4), comparing with the leading order to reproduce the many kinematical variables of the $K_L \to \pi^{\pm} e^{\mp(}\bar{\nu}^{)} e^+ e^-$ decays. Especially, the squared transition momentum t is sensitive to the correction by NLO(p^4). This was expected by the theory and was proved this study.

We measured one of the low energy coupling constants, L_9^r using the slope of data MC ratio of the t distribution. In this study, best value of L_9^r is:

$$L_9^r = (8.0 \pm 1.6) \times 10^{-3} \tag{6.2}$$

This value is consistent with the value, $(6.9 \pm 0.7) \times 10^{-3}$, determined by the electromagnetic charge radius of pion, and this fact indicates the universality of χPT.

A discrepancy between data and theoretical prediction of $M_{e^+e^-}$ is unsolved. This requires more experimental and theoretical studies.

Appendix A

A brief explanation of χPT

Presently the deepest and proven underlying theory of elementary particle physics that has been verified is the standard model. The quantum chromodynamics (QCD) is a part of the standard model, which expresses the strong interaction, i.e., hadron physics. The strong interaction between quarks and gluons represented by QCD is asymptotic. The running coupling constant increases at low energies, confining quarks and gluons. Because of the large coupling constant at low energies, the standard perturbation method is not available for the QCD calculation in a low energy system.

As an effective field theory, chiral perturbation theory (χPT) has been developed for such low energy QCD phenomena, utilizing the chiral symmetry of the quarks. In the world with N_f massless quarks, the QCD Hamiltonian is symmetric under the chiral group $SU(N_f)_L \times SU(N_f)_R$. When this symmetry spontaneously breaks, $N_f^2 - 1$ broken generators appear as the Nambu-Goldstone bosons (NGB) [3, 4]. If the symmetry is broken only spontaneously, there would be massless NGB's, and the Lagrangian of NGB fields could be expanded in powers of the external momenta, p, of NGB using perturbation.

However, in our real world, each type of quarks has its own mass given by the Higgs mechanism. Two lightest quarks, u and d, have masses of $\leq$ 7 MeV/c^2 [29]. Because the masses of u and d are small in the hadron energy scale, the deviations from an exact chiral symmetry due to the quark masses can be corrected for in the Hamiltonian as a perturbation.

Actually, it is natural to consider that the symmetry between u and d in the subgroup $SU(2)_L \times SU(2)_R$ breaks spontaneously and explicitly, because i) no chiral degeneracy is observed; there should be particles with same quantum numbers but with opposite parity, ii) the vacuum expectation values of products of axial currents should be equal to those of vector currents, but those vacuum expectation values have been shown to behave differently in the experiments of semileptonic weak decays. Additionally, we have the three particles of approximately equal masses within the same isospin triplet, pions (π^+, π^-, π^0). This corresponds to $SU(2)_L \times SU(2)_R$ breakdown to the vector isospin symmetry $SU(2)_{L+R}$, producing $N_f^2 - 1 (N_f = 2)$ NGB fields in the system. Pions have the lightest masses in hadrons due to the explicit symmetry breaking by u, d masses, so that they should be called *pseudo*-NGB. The explicit broken symmetry by the quark masses appears in the nonconservative axial currents:

$$\partial^\mu A_\mu^k = F_\pi m_\pi^2 \pi^k + \cdots, \tag{A.1}$$

where $A_\mu^k = \bar{q}\gamma_\mu\gamma_5 T^k q$ is the axial current, T^k are the $SU(2)$ generators, m_π^2 is pion mass, and π^k is the pion field. F_π is the pion decay constant that has been measured in semileptonic process of pion. This relation has been known as the Partial Conservation of the Axial Current (PCAC) by the current algebra method before the establishment of χPT.

For the kaon physics, the strange quark s should be added and the symmetry group should be $SU(3)_L \times SU(3)_R$. In the $N_f = 3$ case, the global rotations are:

$$\begin{aligned} q_L &\to \exp\Big[i\sum_{j=1}^{8}\lambda_j\alpha_j\Big]q_L \equiv Lq_L, \\ q_R &\to \exp\Big[i\sum_{j=1}^{8}\lambda_j\beta_j\Big]q_R \equiv Rq_R, \end{aligned} \tag{A.2}$$

where λ_j's are the Gell-Mann matrices. The nonlinear representation of the NGB fields are:

$$U(x) = \exp\Big[i\sum_{j=1}^{8}\frac{1}{F_0}\,\lambda_j\phi_j\Big], \tag{A.3}$$

where ϕ_j's are the pseudoscalar fields and F_0 is from the coupling constant of the leading order term (F_0^2). Under chiral rotations shown in Eq. A.2, the field U transforms as:

$$U \to RUL^\dagger. \tag{A.4}$$

The basis of the fields can be changed to a field with the quantum numbers of the physical messons:

$$\sum_{j=1}^{8} \lambda_j \phi_j = \sqrt{2} \begin{pmatrix} \frac{1}{\sqrt{2}}\pi^0 + \frac{1}{\sqrt{6}}\eta_8 & \pi^+ & K^+ \\ \pi^- & -\frac{1}{\sqrt{2}}\pi^0 + \frac{1}{\sqrt{6}}\eta_8 & K^0 \\ K^- & \bar{K^0} & -\frac{2}{\sqrt{6}}\eta_8 \end{pmatrix}. \tag{A.5}$$

The important point is that the structure of K-π current is represented in terms of those meson fields, and the dynamics is uniquely derived with chiral Lagrangian having the same symmetry as what QCD has. Although only the low energy coupling constants of every term of Lagrangian of these fields cannot be given by the theory, these coupling constants are common between the decay processes. Therefore, the low energy coupling constants are provided by other experiments.

The coupling constant of the leading order is F_0^2. F_0 is given as F_π, when the system is represented with only leading order. There are ten coupling constants of the next to leading order $L_i (i = 1 \sim 10)$. In present study, we use the matrix element of the $K_L \to \pi^\pm e^{\mp(}\bar{\nu}^{)} e^+ e^-$ decay calculated by χPT to next to leading order [7]. The coupling constants and the kinematics of NGB fields (loops) represent the K-π structure.

To clarify above discussion more, we introduce the Chiral Lagrangian to leading order. With the assumption in χPT that the nonzero quark masses can be involved in the perturbations, we introduce the mass term with the mass matrix:

$$\mathcal{M} = \begin{bmatrix} m_u & 0 & 0 \\ 0 & m_d & 0 \\ 0 & 0 & m_s \end{bmatrix}, \tag{A.6}$$

where m_u, m_d, and m_s are u, d, and s quark masses, respectively. The simplest Lagrangian constructed from U conserving Lorentz and chiral invariance is:

$$\mathcal{L}^{(2)} = \frac{1}{4} F_0^2 \mathrm{Tr}\{\partial_\mu U \partial^\mu U^\dagger + 2B_0 \mathcal{M}(U + U^\dagger)\}. \tag{A.7}$$

B_0 determines the balance between the perturbation expanded by momenta of fields, and by the quark masses. It is a constant that satisfies the Gell-Mann-Oakes-Renner formula [38]:

$$B_0 = -\frac{\langle 0| \bar{q}q |0\rangle}{F_0^2} = \frac{M_\pi^2}{2\hat{m}} = \frac{M_K^2}{\hat{m} + m_s} = \frac{3M_\eta^2}{2(\hat{m} + 2m_s)}, \tag{A.8}$$

where $\langle 0| \bar{q}q |0\rangle$ is the order parameter of spontaneously symmetry braking.

The couplings of other interactions with the electro-magnetic fields, A_μ, and weak fields, W_μ^+, are included in the covariant derivative defined as:

$$D_\mu U \equiv \partial_\mu U - i r_\mu U + i U l_\mu, \tag{A.9}$$

where

$$r_\mu = -eQA_\mu, and \tag{A.10}$$

$$l_\mu = -eQA_\mu - \frac{g}{\sqrt{2}}(W_\mu^+ T_+ + \text{h.c.}). \tag{A.11}$$

Q is the quark charge, and T_+ is the quark mixing matrix including CKM matrix element:

$$Q = \begin{bmatrix} 2/3 & 0 & 0 \\ 0 & -1/3 & 0 \\ 0 & 0 & -1/3 \end{bmatrix}, \quad T_+ = \begin{bmatrix} 0 & V_{ud} & V_{us} \\ 0 & 0 & 0 \\ 0 & 0 & 0 \end{bmatrix}. \tag{A.12}$$

Consequently, the lowest order Lagrangian becomes:

$$\mathcal{L}^{(2)} = \frac{1}{4} F_0^2 \text{Tr}\{D_\mu U D^\mu U^\dagger + U\chi^\dagger + \chi U^\dagger\}, \tag{A.13}$$

where $\chi = 2B_0\mathcal{M}$. We call this Lagrangian the "leading order (LO) Lagrangian" or "order of p^2 of Lagrangian". Tsuji has calculated [7] the amplitude of $K_L \to \pi^\pm e^{\mp(}\bar{\nu}^{)} e^+ e^-$ using this Lagrangian, and the amplitudes from the Lagrangian to next to leading order (p^4) and one-loop diagrams of order of p^2 [NLO(p^4)] [7].

The Lagrangian to next to leading order ($\mathcal{L}^{(4)}$) is composed of ten terms as:

$$\begin{aligned}
\mathcal{L}^{(4)} &= L_1 < D_\mu U D^\mu U^\dagger >^2 + L_2 < D_\mu U D_\nu U^\dagger >< D^\mu U D^\nu U^\dagger > \\
&+ L_3 < D_\mu U D^\mu U^\dagger D_\nu U D^\nu U^\dagger > + L_4 < D_\mu U D^\mu U^\dagger >< \chi U^\dagger + U\chi^\dagger > \\
&+ L_5 < D_\mu U D^\mu U^\dagger (\chi U^\dagger + U\chi^\dagger) > + L_6 < \chi U^\dagger + U\chi^\dagger >^2 \\
&+ L_7 < \chi U^\dagger - U\chi^\dagger >^2 + L_8 < \chi U^\dagger \chi U^\dagger + U\chi^\dagger U\chi^\dagger > \\
&- iL_9 < f_{\mu\nu}^R D^\mu U D^\nu U^\dagger + f_{\mu\nu}^L D^\mu U^\dagger D^\nu U > + L_{10} < U^\dagger f_{\mu\nu}^R U f^{L\mu\nu} >
\end{aligned} \tag{A.14}$$

For the coupling constants, L_i's, we use the experimental values of renormalized low energy coupling constants, L_i^r's, at the scale $\mu = M_\rho$ (mass of ρ messon) [7].

Appendix B

The phase-space generator for $K_L \to \pi^{\pm} e^{\mp} \overset{(-)}{\bar{\nu}} e^{+} e^{-}$

In this Appendix, we describe the phase space generator we made for the $K_L \to \pi^{\pm} e^{\mp} \overset{(-)}{\bar{\nu}} e^{+} e^{-}$ decay mode. The first half of the description almost follows the descliption by [39]

We create the five-body phase space event generator according to Ref. [39]. We define the n-body phase space integral as:

$$R_n = \int \delta^4\Big(P - \sum_{j=1}^{n} p_j\Big) \prod_{i=1}^{n} \delta(p_i^2 - m_i^2) d^4 p_i, \tag{B.1}$$

where P is the total four-vector of the n-body system, p_i are the four-vectors of the individual particles, and m_i are the masses of the particles. If we then consider any kinematic parameter α; a momentum, angle, etc. of the system, its spectrum will be given by

$$f(\alpha) = \frac{d}{d\alpha}(|M.E.|^2 \cdot R_n) \tag{B.2}$$

where $M.E.$ is the matrix element describing the interactions between the particles.

Since Eq. (B.1) is given in the covariant formulation, R_n is allowed to be expressed in any frame of reference. This in turn the (n+1)-body space is allowed to be expressed in terms of the n-body phase space, each one being calculated in its own center of mass. Therefore,

we write, as in Eq. (B.1):

$$R_n(P; m_1 \cdots m_n) = \int \delta^4\Big(P - \sum_{i=1}^{n} p_i\Big) \prod_{j=1}^{n} \delta(p_j^2 - m_j^2) d^4 p_j, \tag{B.3}$$

where we have written explicitly the quantities upon which R_n depends. Actually it depends only on the magnitude of the four-vector P, the total energy in the center of mass, or invariant rest mass, from Lorentz invariance. If we rewrite the argument of the first delta function and split off the last factor in the indicated product, we obtain:

$$R_n(P; m_1 \cdots m_n) = \int \Big\{ \int \delta^4\Big[\sum_{i=1}^{n-1} p_i - (P - p_n)\Big] \prod_{j=1}^{n-1} \delta(p_j^2 - m_j^2) d^4 p_j \Big\} \delta(p_n^2 - m_n^2) d^4 p_n. \tag{B.4}$$

It is seen by inspection that the factor in curly brackets is just $R_{n-1}(P - p_n; m_1 \cdots m_{n-1})$. Using Eq. (B.2), we have the following relation:

$$R_n(P; m_1 \cdots m_n) = \int R_{n-1}(P - p_n; m_1 \cdots m_{n-1}) \frac{d^3 p_n}{2E_n}. \tag{B.5}$$

If repeated use is made of this relation, each R_i may be the same algebraic function since it may be evaluated in its own rest frame.

One of the effective methods to make generator using the recurrence relation (B.5) works essentially with invariant masses as kinematic coordinates.

We first express the four-momentum conservation dalta function in Eq. B.1 as an integral over two delta functions:

$$\delta^4\Big(P - \sum_{j=1}^{n} p_j\Big) = \int \delta^4\Big(P - P_\ell - \sum_{j=\ell+1}^{n} p_j\Big) \delta^4\Big(P_\ell - \sum_{j=1}^{\ell} p_j\Big) d^4 P_\ell. \tag{B.6}$$

The above relation is derived from the following form:

$$\begin{aligned} \delta(x - y) &= \int \delta[(y - c) - z]\ \delta[z - (x - c)] dz \\ &= \delta[(x - c) - (y - c)]. \end{aligned} \tag{B.7}$$

Substitute (B.6) into (B.1), we obtain:

$$\begin{aligned} R_n(P; m_1 \cdots m_n) &= \int \delta^4\Big(P - P_\ell - \sum_{j=\ell+1}^{n} p_j\Big) \prod_{j=\ell+1}^{n} \delta(p_j^2 - m_j^2) d^4 p_j \\ &\quad \times \int \delta^4\Big(P_\ell - \sum_{j=1}^{\ell} p_j\Big) \prod_{j=1}^{\ell} \delta(p_j^2 - m_j^2) d^4 p_j d^4 P_\ell, \end{aligned} \tag{B.8}$$

where P_ℓ is the four momentum of the ℓ-body subsystem within the n-body system. However, the integral is not yet divided into exactly corresponding factors, since there is one delta function missing in the d^4P_ℓ integration, namely $\delta(P_\ell^2 - M_\ell^2)$. Following Hagedorn [40], we introduced the factor one of the form

$$1 = \int_0^\infty \delta(P_\ell^2 - M_\ell^2) dM_\ell^2. \tag{B.9}$$

Applying this relation to Eq. B.10, we get the desired expression:

$$\begin{aligned} R_n(P; m_1 \cdots m_n) &= \int_0^\infty \Big\{ \int \delta^4\Big(P - P_\ell - \sum_{j=\ell+1}^{n} p_j\Big) \prod_{j=\ell+1}^{n} \delta(p_j^2 - m_j^2) \\ &\quad \times \delta(P_\ell^2 - M_\ell^2) d^4p_j d^4P_\ell \int \delta^4\Big(P_\ell - \sum_{j=1}^{\ell} p_j\Big) \\ &\quad \times \prod_{j}^{\ell} \delta(p_j^2 - m_j^2) d^4p_j \Big\} dM_\ell^2 \\ &= \int_0^\infty R_{n-\ell+1}(P; M_\ell, m_{\ell+1} \cdots m_n) R_\ell(P_\ell; m_1 \cdots m_\ell) dM_\ell^2. \end{aligned} \tag{B.10}$$

The last expression is called *splitting* relation in Ref. [39]. From Eq. B.9, we see that M_ℓ^2 is the square or the four momentum of the ℓ particles; their invariant mass. The limits of integration for M_ℓ^2 are:

$$\Big(\sum_{i=1}^{\ell} m_i\Big)^2 \leq M_\ell^2 \leq \Big(M_n - \sum_{i=\ell+1}^{n} m_i)\Big)^2. \tag{B.11}$$

Repeated application of the splitting relation, starting with $\ell = 2$, lead us to the recurrence relation:

$$R_n = \int dM_{n-1}^2 \cdots \int dM_2^2 \prod_{i=1}^{n-1} R_2(M_{i+1}; M_i, m_{i+1}). \tag{B.12}$$

The two-body phase space factor $R_2(M_{i+1}; m_i, m_{i+1})$ is:

$$R_2(M_{i+1}; M_i, m_{i+1}) = \frac{2\pi}{M_{i+1}} \sqrt{M_{i+1}^2 + \Big(\frac{M_i^2 - m_{i+1}^2}{M_{i+1}}\Big)^2 - 2(M_i^2 + m_{i+1}^2)}. \tag{B.13}$$

Substituting Eq. B.13 into Eq. B.12, and transforming from dM^2 to $2MdM$, we get the final form used by M-generators:

$$R_n = \int dM_{n-1} \cdots \int dM_2 \prod_{i=1}^{n-1} \Big[2M_i R_2(M_{i+1}; M_i, m_{i+1})\Big]. \tag{B.14}$$

To use Eq. B.14, we have to determine the limits of integration on M.

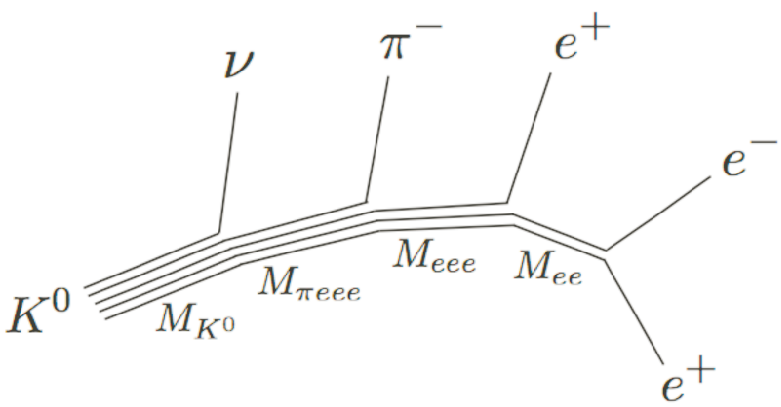

Figure B.1: A diagram for the sequential two-body decays for $K_L \to \pi^{\pm} e^{\mp(}\bar{\nu}^{)} e^{+} e^{-}$ decay. M_{ee}, M_{eee}, and $M_{\pi eee}$ correspond M_1, M_2, and M_3, respectively.

Figure B.1 shows the sequential decay presented in Eq. B.14. We need apply only the two-body phase-space factor at the first vertex (A), but this must be integrated over all possible masses M_{n-1}. Then we apply the two-body factor at (B), integrating all possible masses M_{n-2} and all possible M_{n-1}, because the *initial state energy* at (B) is now variable also. Similarly for the other vertices.

There are the limits of integration of the M in Eq. B.14, physically. For each M_j, we must have

$$M_{j-1} + m_j < M_j < M_{j+1} - m_{j+1}, \tag{B.15}$$

With these methods, the integral space for M_j depends on $M_{j-1} + m_j$ and $M_{j+1} - m_{j+1}$, then the plane random numbers for MC integration can not be used; the narrower integral space has higher density points than the broader integral space. This means that the M_j must be chosen independently on M_{j-1} and M_{j+1}, but must be chosen to satisfy only the less restrictive condition:

$$\sum_{i=1}^{j} m_i < M_j < M_n - \sum_{i=j+1}^{n} m_i, \tag{B.16}$$

where M_n is the mass of decay particle. The integral space for M_j by Eq. B.16 has a uniform density of MC integral points, but has non-physical space on the difference between Eq. B.15 and Eq. B.16. To avoid non-phyisical space, the invariant masses, M_j, are chosen according

to the following:

$$M_j = r_j\Big(M_n - \sum_{i=1}^{n} m_i\Big) + \sum_{i=1}^{j} m_i \tag{B.17}$$

with:

$$0 < r_1 < \cdots < r_j < r_{j+1} < \cdots < r_{n-2} < 1, \tag{B.18}$$

where r_j is a random number between zero and one. When we create $n-2$ random numbers independently, the random numbers may be ordered without biasing the results.

An event has additional $2(n-1)$ degrees of freedom for two angular variables on each two-body vertex, then total degree of freedom becomes $3n-4$. The angular variables $\cos\theta$ and ϕ is isotropic only in the center of mass frame of the two-body decay. We must be in the rest frame of each two-body system to create them, then successively apply Lorentz-transform into the rest frame of the group of particles preceding it.

We used *GENBOD* routine in the *CERNLIB* [39] that follows the above procedure, as a basis for generating $K_L \to \pi^{\pm}e^{\mp}\overset{(}{\bar{\nu}}{}^{)}e^{+}e^{-}$ events. The routine was however, modified to use double precision inside the routine. We additionally modify this program to create especially the $K_L \to \pi^{\pm}e^{\mp}\overset{(}{\bar{\nu}}{}^{)}e^{+}e^{-}$ events in the followings.

A general procedure for generating decays is to throw particles in a uniform phase space, calculate the square of the matrix element (probability) for that kinematics, and accept the events only if another random number is smaller than the probability. However, this general procedure has the following two problem for generating $K_L \to \pi^{\pm}e^{\mp}\overset{(}{\bar{\nu}}{}^{)}e^{+}e^{-}$:

1. The $K_L \to \pi^{\pm}e^{\mp}\overset{(}{\bar{\nu}}{}^{)}e^{+}e^{-}$ decay has two candidates of the $e^{+}e^{-}$ pair. Which pair should be assigned as the $e^{+}e^{-}$ pair invariant mass in phase space coordinate?

2. As shown in Fig. B.2, there are sharp ridges around $M_{e_1^{\pm}e^{\mp}} = 0$ and the diagonal line near $M_{e_1^{\pm}e_2^{\pm}e^{\mp}} = M_{e_1^{\pm}e^{\mp}}$. The diagonal line corresponds to events with a small $e_2^{\pm}e^{\mp}$ mass. With these sharp ridges, most of the events generated in the uniform phase space will be rejected due to their small probabilities. How can we generate the decays more effectively, in a limited computing time?

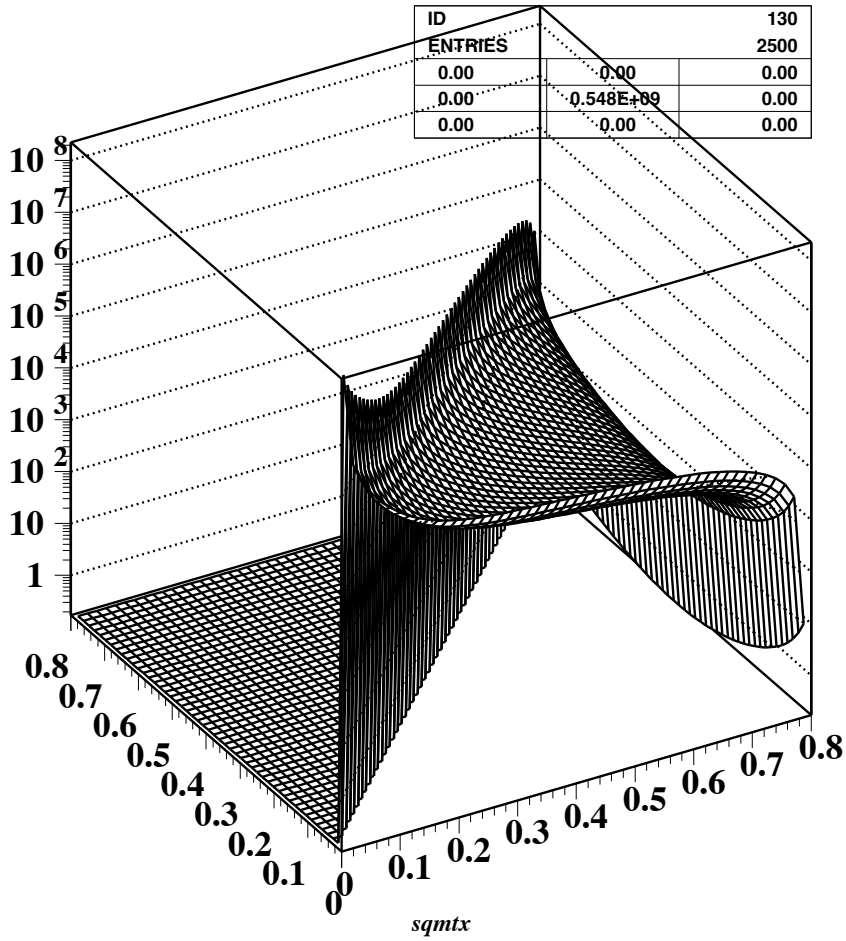

Figure B.2: The absolute square of the amplitude depending on the random numbers for $M_{e^+e^-}$ and $M_{e^{\pm}e^+e^-}$ with certain other values on nine coordinates of freedom.

These problems were solved in the following way. First, we selected the smaller $M_{e^+e^-}$ as M_1 and $M_{e^\pm e^+e^-}$ as M_2 in Eq. B.14, i.e., when the other $M_{e^+e^-}$ candidate was smaller than M_1, this event was rejected. We then calculated the full decay amplitude according to Eq. B.19:

$$\mathcal{M}_{total} = \mathcal{M}_{generate} - \mathcal{M}_{exchange}, \tag{B.19}$$

where $\mathcal{M}_{generate}$ is the amplitude for a given point in the invariant mass coordinates, and $\mathcal{M}_{exchange}$ is the amplitude at the same coordinate except that the two electrons with the same charge are exchanged. With this method, the ridge along the diagonal line shown in Fig. B.2 was removed.

Second, we generated the $M_{e^+e^-}$ only in the ragion $M_{e^+e^-} > 0.005$ GeV/c^2. This lowered the height of the ridge near $M_{e^+e^-} = 0$. The cutoff value allows us to assign the random numbers avoiding the too small invariant mass of e^+e^- pair to generate practically, while we can not avoid to assign the random numbers for the events that *the other pair* has such a small invariant mass. Therefore, the first method again helps us to reject the events having larger invariant mass of generated e^+e^- pair than the other pair.

Third, we modified the phase space generator to distribute more events in the area with a large matrix element. We divided the $M_1 = M_{e^+e^-}$ in 60 bins, and $M_2 = M_{e^\pm e^+e^-}$ in 56 bins. The width of the bin for the high density area was set nrrower, and vice versa, to avoid to be changed the event weight for each event.

Appendix C

Study of Pion-hadron interaction in TRD

In this chapter, we find the function of the ratio of missing pion tracks due to π-hadron interaction in the eight modules of TRD's. Using the *GEANT* simulation, we calculated the probability that an incident pion going through the TRD's, deposits an energy on a CsI calorimeter within 7 cm from the position where the pion would arrive without any interactions. Because we applied the hadronic interaction in the TRD's, a part of pions did not arrive there.

Figure D.1 shows the experimental alignment in the *GEANT* simulation. The energy of pion was given between 10 GeV and 100 GeV with 10 GeV steps. For every energy step, 10000 of pions were tested. The matter of each TRD modules were set according to [11].

Figure C.2 shows the missing ratio as a function of pion energy. We fit an exponential function to this plots as:

$$\delta(E_\pi)^{norm} = I \exp(-E_\pi/\lambda) + C \tag{C.1}$$

where I, λ, and C are fitting parameters. This function expresses the ratio of losses of pions, when the track perpendicularly penetrates the TRD. Therefore, the weight multiplied the pions should be:

$$wt(\pi) = 1 - \delta(\pi) = 1 - \delta(E_\pi)^{norm} L_{\text{path}}, \tag{C.2}$$

where L_{path} is the path length in TRD's normalized by the length of whole of TRD's. When

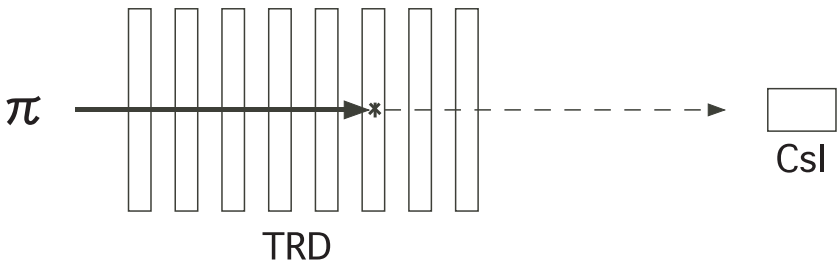

Figure C.1: A schematic of alignment of 'GEANT' simulation. Pions were counted which perpendicularly entered into TRD and deposited an energy on 0.14 m diameter cross section of the CsI. The energies of incident pions were provided between 10 GeV and 100 GeV. Alignment of TRD's and CsI were set according to the KTeV experiment [41].

the pion penetrates the beam holes, the path length in the beam holes is subtracted from the lentgh of whole path. Thereafter, weighted path length in the beam holes are added again, because there is no radiator in the beam holes.

In MC used in this thesis, every event is weighted by $wt(\pi)$ regarding every pion in the event.

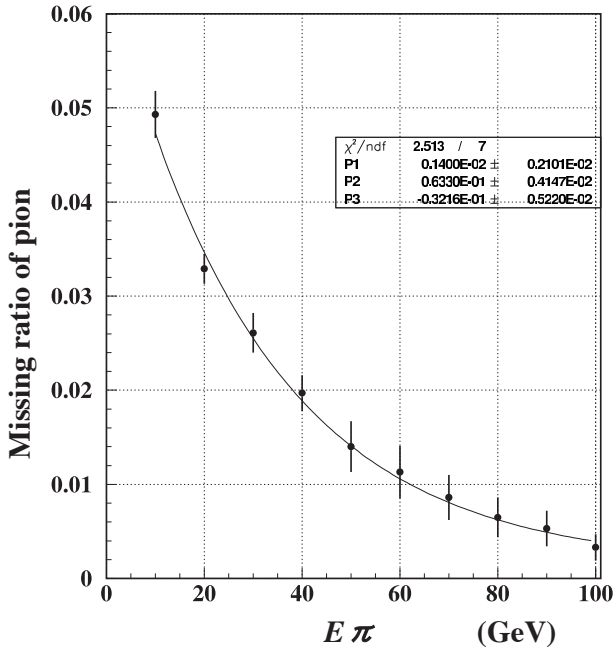

Figure C.2: The ratio of losses of pion tracks as a function of pion energy. The path length is the length of TRD

Appendix D

The index for π-e separation by TRD; $Prob_\pi$

To separate pions and electrons using TRD, we define a variable referred to as *pion probability* ($Prob_\pi$). This variable combines the pulse height information from 16 sense wire planes in the TRD modules, and gives a probability of the track being a pion.

The separation between pions and electrons is based on the difference in the energy deposit in the TRD chamber. Pions and electrons deposit ionization energy in the chamber. Electrons, however, also emit X-rays in the radiator due to transition radiation, and thus deposit larger energy than pions.

Figure D.1 shows the distribution of energy deposit by pions and electrons, separately. The particles were identified by E/p separation for the $K_L \to \pi^\pm e^{\mp(}\bar{\nu}^{)}$ events. The lower plot in Fig. D.1 shows the fraction of the events in the pion distribution above a given threshold, as a function of the threshold ADC counts.

We made this function for each TRD sense wire plane, and named the function for the i-th TRD sense wire plane as CL_i (ADC counts). If events are plotted against CL_i, pions distribute uniformly, whereas electrons peak near $CL_i = 0$.

To introduce the combined CL, we suppose that we have two CL_i from sense plane 1 (CL_1) and 2 (CL_2). When the combined CL_{12} is defined as the new ordering of the product

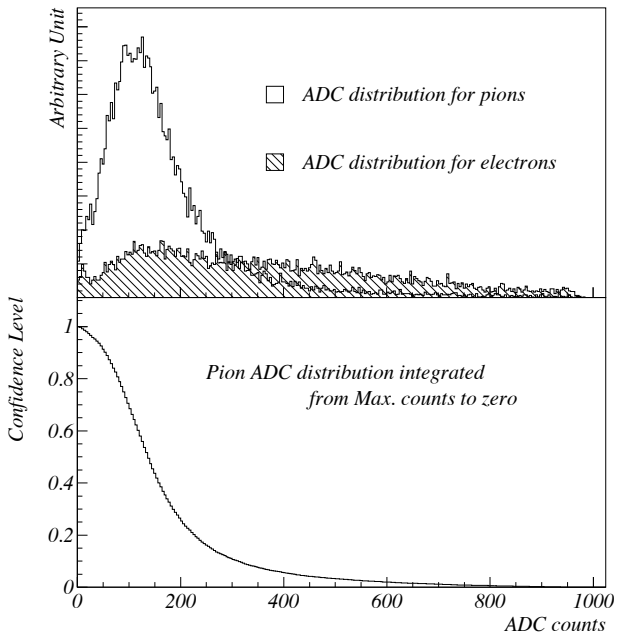

Figure D.1: Top: The ADC distribution for pions (open histogram) and electrons (hatched histogram) in a plane. Bottom: The translation from ADC counts to CL_i. Integrating the ADC distribution for pions (top) from maximum ADC to zero, normalized to make the maximum be unity, gives the bottom plot.

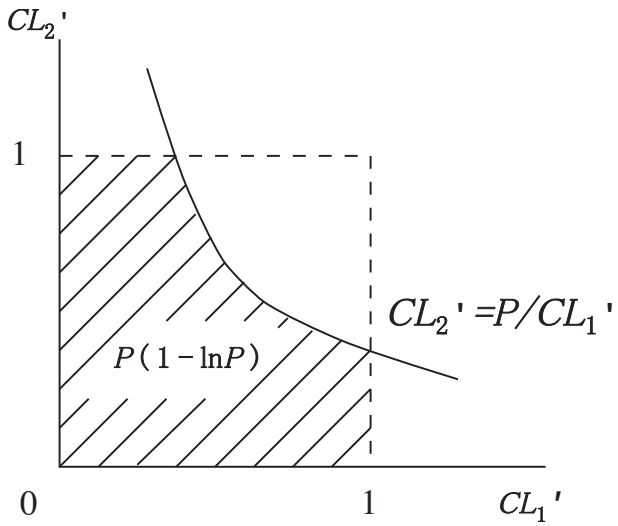

Figure D.2: The two-dimensional combined CL space. The shaded area corresponds to two-dimensional CL_{12} obtained from CL_1 and CL_2. P is provided as $P = CL_1 \times CL_2$, then the hyperbola should be $CL_2' = P/CL_1'$.

$P = CL_1 \times CL_2$ on a two-dimensional space (CL'_1, CL'_2) in Fig. D.2, then the order of P in the (CL'_1, CL'_2) should be the area under the hyperbola $P = CL'_1 \times CL'_2$, where $CL'_1 \times CL'_2 < P$:

$$CL_{12} = 1 - \int_P^1 d(CL'_2) \int_{P/CL'_2}^1 d(CL'_1) \tag{D.1}$$

$$= P(1 - \ln P). \tag{D.2}$$

With a definition of $\prod_{i=1}^{16} CL_i \equiv P_{16}$ and the expansion of Eq. D.1, the combined CL_{Total} in 16-dimensional space becomes:

$$CL_{Total} = P_{16} \times \sum_{i=0}^{15} \frac{(-\ln P_{16})^i}{i!}. \tag{D.3}$$

This expression is based on the assumption that the confidence level between each plane does not have a correlation. However, there are small correlations due to the limited binning in the lookup tables of CL_i functions, and thus the CL_i does not uniformly distribute. In order to make the CL_{Total} as flat as possible in the region $CL_{Total} < 0.8$, we applied an empirically found correction, and defined the corrected CL_{Total} as $Prob_\pi$.

Appendix E

Corrections for inefficiencies in π-e separations

The discrepancies of the inefficiencies of π-e separation between in data and in MC are the sources of the biases on the branching fraction of $K_L \to \pi^{\pm} e^{\mp(}\bar{\nu}^{)} e^+ e^-$. In this chapter, we determine the correction factors, δ_i, for the such biases in the E/p selection and the TRD selection.

E.1 The E/p selection.

The electron inefficiency

Figure E.1 shows the E/p distribution of electrons. These electrons were collected as the $K_L \to \pi^+\pi^-\pi^0_D$ events with $E/p < 0.6$ and TRD $Prob_\pi < 0.01$ for pion tracks, $E/p > 0.6$ for electron tracks, and with strict requirements for the invariant masses of whole system, $0.497 < M_{\pi\pi ee\gamma} < 0.499$ GeV/c^2, and the $e^+e^-\gamma$ system, $0.1345 < M_{ee\gamma} < 0.1360$ GeV/c^2.

The requirement of the final cut, $0.93 < E/p < 1.15$ for electron tracks leaves $(1.84 \pm 0.07)\%$ and $(1.50 \pm 0.05)\%$ of events out of the acceptable region for data and MC, respectively. Therefore, the correction factor ($\delta_{e,E/p}$) on the $BR(K_L \to \pi^{\pm} e^{\mp} \nu e^+ e^-)$ for the electron inefficiency in E/p selection is $(0.34 \pm 0.09)\%$. where the error is only the statistical error. Since the electrons in the $K_L \to \pi^{\pm} e^{\mp(}\bar{\nu}^{)} e^+ e^-$ decays have different distributions of their

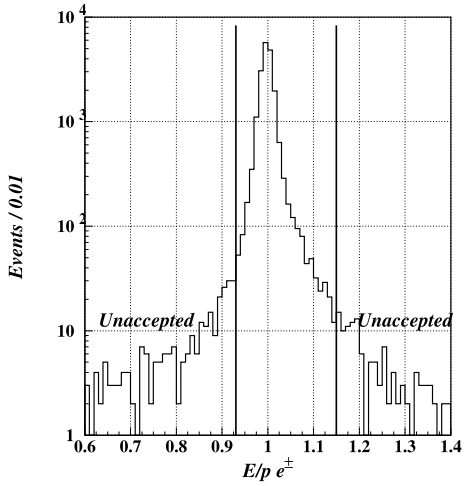

Figure E.1: E/p distribution of electron candidates in $K_L \to \pi^+\pi^-\pi^0_D$ sample collected with restricted invariant mass criteria. The vertical lines indicate the cut bounds of E/p to select the electron candidate. .

energy than the $K_L \to \pi^+\pi^-\pi^0_D$ decays, we investigated the energy dependence of the $\delta_{e,E/p}$.

Because the statistical uncertainty of $\delta_{e,E/p}$ is already 26%, we divided the samples into only two groups: Low $E_{e^\pm}$ sample with $E_{e^\pm} < 8$ GeV and High $E_{e^\pm}$ sample with $E_{e^\pm} > 10$ GeV. For the Low $E_{e^\pm}$ sample, the $\delta_{e,E/p}$ was $(0.29 \pm 0.11)\%$, and for the hight $E_{e^\pm}$ sample, the $\delta_{e,E/p}$ was $(0.34 \pm 0.10)\%$. Since the $\delta_{e,E/p}$'s for both Low and Hight $E_{e^\pm}$ samples are consistent with each other within the statistical error, we ignore the decay mode dependence of $\delta_{e,E/p}$.

The pion inefficiency

Figure E.2 shows the E/p distribution of pion. These pions were collected as $K_L \to \pi^+\pi^-\pi^0$ events followed by $\pi^0 \to \gamma\gamma$ ($K_L \to \pi^+\pi^-{\pi^0}_{\gamma\gamma}$), without E/p performance and with the requirement of the invariant mass of whole of system; $0.497 < M_{\pi\pi\gamma\gamma} < 0.499$.

The requirement of the final cut, $E/p < 0.9$ for pion tracks, leaves $(0.809 \pm 0.011)\%$ and $(0.566 \pm 0.024)\%$ of whole events out of the acceptable region for data and MC, respectively. Therefore, the correction factor ($\delta_{\pi,E/p}$) for the inefficiency of pion in the E/p selection is $(0.243 \pm 0.028)\%$. where the error is only the statistical error. Also for the pion inefficiency

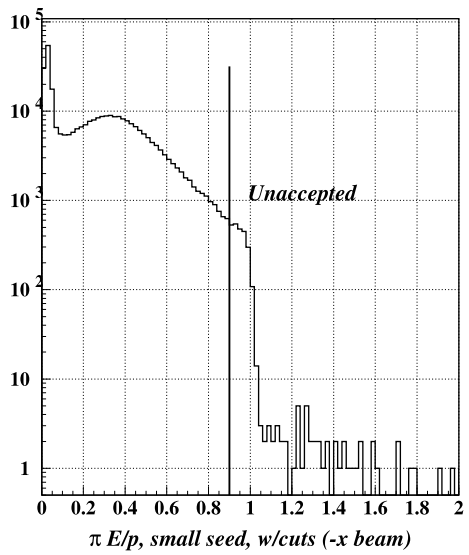

Figure E.2: E/p distribution of pion candidates in $K_L \to \pi^+\pi^-\pi^0_{\gamma\gamma}$ sample collected with restricted invariant mass criteria. The vertical line indicates the cut bound of E/p to select pion. .

in E/p selection, the energy dependence of $\delta_{\pi,E/p}$ were investigated. Because the statistical uncertainty of $\delta_{\pi,E/p}$ is already 11%, we divided the samples in only two groups: Low $E_{\pi^\pm}$ sample with $E_{\pi^\pm} < 18$ GeV and High $E_{\pi^\pm}$ sample with $E_{\pi^\pm} > 22$ GeV.

For the Low $E_{\pi^\pm}$ sample, the $\delta_{\pi,E/p}$ is $(0.25 \pm 0.05)\%$, and for the hight $E_{\pi^\pm}$ sample, the $\delta_{\pi,E/p}$ is $(0.19 \pm 0.06)\%$. Since the $\delta_{\pi,E/p}$'s for both Low and Hight $E_{\pi^\pm}$ samples are consistent with each other within the statistical error, we ignore the decay mode dependence of $\delta_{\pi,E/p}$.

E.2 The TRD selection

Using the same data in the study of the E/p inefficiency of electron i.e.,the $K_L \to \pi^+\pi^-\pi^0_D$ decays, but with more restrict requirement of E/p for electron; $0.95 < E/p < 1.05$, we found that the requirement of the final cut, $Prob_\pi < 0.06$ for the electron tracks, left $3.23 \pm 0.05\%$ and $2.89 \pm 0.03\%$ of whole events out of the acceptable region for data and MC, respectively. Therefore, the correction factor ($\delta_{e,TRD}$) for the inefficiency of electron in the TRD selection is $(0.35 \pm 0.06)\%$.

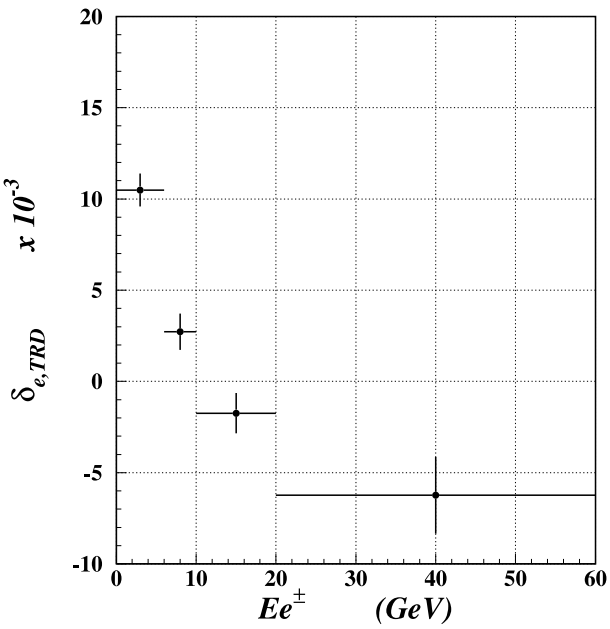

Figure E.3: The electron energy dependence of the correction factor for the electron inefficiency in the TRD selection .

To study the electron energy dependence of $\delta_{e,TRD}$, we divided the samples into the four degrees of energy of electrons: 0-6 GeV, 6-10 GeV, 10-20 GeV, and greater than 20 GeV. As shown in Fig. E.3 there is an electron energy dependence of $\delta_{e,TRD}$.

To obtain the $\delta_{e,TRD}$ for the $K_L \rightarrow \pi^{\pm}e^{\mp(}\bar{\nu}^{)}e^{+}e^{-}$ decays, we summed $\delta_{e,TRD}$ for each electron energy region after weighting it by its composition ratio. The obtained $\delta_{e,TRD}$ for the $K_L \rightarrow \pi^{\pm}e^{\mp(}\bar{\nu}^{)}e^{+}e^{-}$ is $4.0 \pm 1.1\%$. Because the difference of $\delta_{e,TRD}$ depending on the decay modes is smaller than the statistical error, we ignore the decay mode dependence of $\delta_{e,TRD}$.

Appendix F

Correction factor for the ratio that a pion misidentified as an electron

As shown in Fig. 3.8, we need to correct the ratio of the $K_L \to \pi^+\pi^-\pi^0_D$ MC events that the pions are misidentified as electrons. To estimate the correction factor, we plotted the distribution of $M_{\pi\pi ee}$ for the events collected for Fig. 3.8, i.e., collected as the $\pi^\pm e^\mp e^+ e^-$ events but with positive k_{+-0}. To reconstruct the $M_{\pi\pi ee}$, the role of $e^\pm_{ke3}$ candidates were changed to $\pi^\pm$ candidates. Figure F.1 shows such the plot. Additional to the positive k_{+-0}, the $K_L \to \pi^\pm e^{\mp(}\bar{\nu}^{)} e^+ e^-$ sigal events are suppressed because the incorrect ($e^\pm_{ke3} \to \pi^\pm$) assigning makes too large $M_{\pi\pi ee}$ for the actual $\pi^\pm e^\mp e^+ e^-$ events. The correction factor $f_{\pi e:E/p}$ was estimated from the number of events in Fig. F.1 using the following equation:

$$f_{\pi e:E/p} = \frac{N_{data} - \sum_i N_{\mathrm{BG}\ i} - N_{ke3ee}}{N_{\mathrm{BG}+-0}} \tag{F.1}$$

where N_{data} is the number of observed events in the data, N_{BG} is the number of estimated background events i, N_{ke3ee} is the number of estimated signal events, and $N_{\mathrm{BG}+-0}$ is the number of estimated $K_L \to \pi^+\pi^-\pi^0_D$ background events without the correction factor $f_{\pi e:E/p}$. The $f_{\pi e:E/p}$ depends on our final results of the $BR(K_L \to \pi^\pm e^\mp \nu e^+ e^-)$, therefore, $f_{\pi e:E/p}$ was estimated with a iterative process.

The estimated $f_{\pi e:E/p} = 1.760 \pm 0.009$ with a statistical error. For the well suppression of the signal events in Fig. F.1, the $f_{\pi e:E/p}$ is not sensitive to the final result of $BR(K_L \to \pi^\pm e^\mp \nu e^+ e^-)$. We confirmed that 7% of shift of the $BR(K_L \to \pi^\pm e^\mp \nu e^+ e^-)$ corresponds to the statistic error of $f_{\pi e:E/p}$.

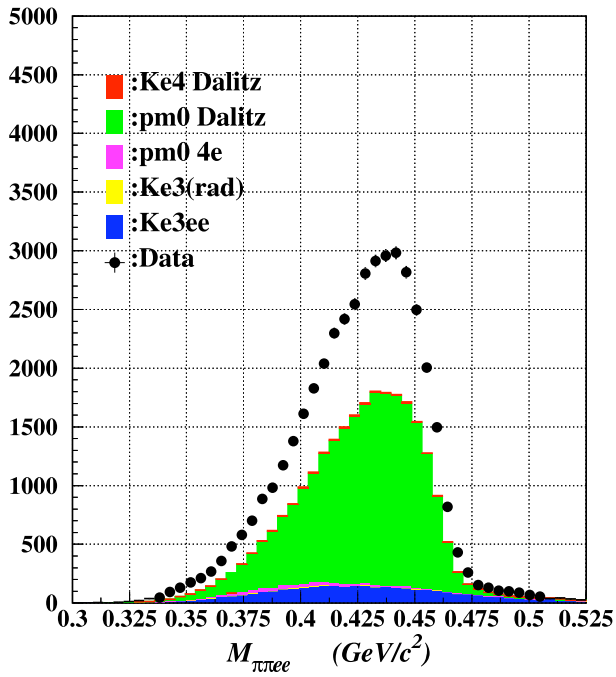

Figure F.1: The invariant mass distribution of $\pi^+\pi^-e^+e^-$ system. The events are corrected as the $\pi^\pm e^\mp e^+e^-$ events. Thereafter, $e^\pm_{ke3}$ candidates are assigned as pions. Ke4 Dalitz, pm0 Dalitz, pm0 4e, Ke3(rad), and Ke3ee denote $K_L \to \pi^\pm e^\mp \nu \pi^0_D$, $K_L \to \pi^+\pi^-\pi^0_D$, $K_L \to \pi^+\pi^-\pi^0_{4e}$, $K_L \to \pi^\pm e^\mp {}^{(}\bar{\nu}^{)}\gamma$, and $K_L \to \pi^\pm e^\mp {}^{(}\bar{\nu}^{)}e^+e^-$, respectively.

Appendix G

The transition momentum

In Sec. 5.2.1, we showed that NLO(p^4) correction removed the discrepancy in t/M_π^2 distribution that existed between data and MC-LO of χPT. Simultaneously, we left the next two questions unanswered,

1. Why is the slope of linear fitted line to the data-to-(MC-LO) ratio smaller than the theoretical prediction shown in Fig. 1.4?

2. What causes the large difference in the shape of t/M_π^2 spectrum between the t/M_π^2 for the E_K maximum solution and the t/M_π^2 for the E_K minimum solution?

In this Appendix, we will investigate these questions.

Hereafter, we call the slope of the linear fitted line to the ratio of the t/M_π^2 distributions between different kinds of MC, or data and MC, as *Slope*. The t/M_π^2 using E_K maximum and E_K minimum solutions are written as t/M_π^2 (max) and t/M_π^2 (min), respectively. Also, MC-LO means the MC by χPT calculated to the leading order, and MC-NLO means the MC corrected by the next to leading order.

G.1 The effect of incorrect E_K selection

First, we study the effect of incorrect selection of the E_K solution that is unavoidable in the reconstruction. Since we know the correct solution in MC, we can separate the events into two categories as the follows:

- The events that their E_K maximum solutions are correct. In this case, the longitudinal momentum of neutrino in the kaon rest frame along the kaon momentum in the laboratory frame is positive. We call those events "$P_\nu^{(+)}$ events".

- The events that their E_K minimum solution are correct for them ($P_\nu^{(-)}$ events).

Without any analysis cuts, the ratio of the number of events in these categories is 50 : 50. We can separately measure the *Slope* in the correct case and in the incorrect case, for t/M_π^2 (max) and t/M_π^2 (min), respectively. The *Slope*s for respective cases are summarized in Table G.1.

Table G.1: The slopes of the (MC-LO)-to-(MC-NLO) ratio with correct E_K solution events, incorrect E_K solution events and whole of evets.

	t/M_π^2 (max)	t/M_π^2 (min)
Correct	4.61±0.07	4.61±0.07
Incorrect	1.87±0.06	1.58±0.06
Whole	3.01±0.05	3.05±0.05
data/MC-LO	2.5±0.6	3.7±0.6
		($\times 10^{-2}$)

For both E_K minimum and E_K maximum solutions, the *Slope*s for the correct E_K events (4.6×10^{-2}) are close to the prediction by theoretical calculation (5×10^{-2}). On the other hand, the *Slope*s for the incorrect E_K events are lower. This is one of the reasons that the *Slope* is smaller for the data/ MC-LO than the theoretical prediction, because the whole data consists of almost the same amount of correct and incorrect events.

G.2 The effects of the selection cuts

We also studied the effects of each cut used in the analysis, on the *Slope* of MC-NLO / MC-LO. We found that requiring $E_\pi > 10$ GeV, and requiring $E_{e^+} > 3$ GeV and $E_{e^-} > 3$ GeV, both changes the *Slope* for t/M_π^2 (max) and t/M_π^2 (min). In the following subsections, we will discuss those mechanisms.

G.2.1 Pion energy cut

After requiring $E_\pi > 10$ GeV, the *Slope* changes as:

$$(3.01 \pm 0.05) \times 10^{-2} \rightarrow (2.75 \pm 0.06) \times 10^{-2} \quad \text{for } t/M_\pi^2 \text{ (max)}, \quad \text{and,}$$
$$(3.05 \pm 0.05) \times 10^{-2} \rightarrow (3.58 \pm 0.06) \times 10^{-2} \quad \text{for } t/M_\pi^2 \text{ (min)}.$$

For each category of $P_\nu^{(+)}$ and $P_\nu^{(-)}$ events, the *Slope* was not affected by the $E_\pi > 10$ GeV cut.

Figure G.1 shows the distributions of the longitudinal pion momentum in the kaon rest frame along the kaon momentum in the laboratory frame ($P_\pi \cdot \hat{P}_K$) for $P_\nu^{(+)}$ events and $P_\nu^{(-)}$ events, with and without the $E_\pi > 10$ GeV cut.

From Fig. G.1, we found that the ratio of $P_\nu^{(+)}$ events and $P_\nu^{(-)}$ events changed from 50:50 to 42:58 after the $E_\pi > 10$ GeV cut.

Using respective *Slope*s of the whole events for t/M_π^2 (max) and t/M_π^2(min), and new correct-incorect compositions by $E_\pi > 10$ GeV cut, we obtained *Slope*s 2.81×10^{-2} and 3.34×10^{-2}, respectively, using linear correlation of the compositions and *Slope*s. Therefore, we conclude that the main reason of difference of *Slope*s between for t/M_π^2 (max) and for t/M_π^2(min) by the E_π cut are brought by an unequal mixture of correct E_K solutions.

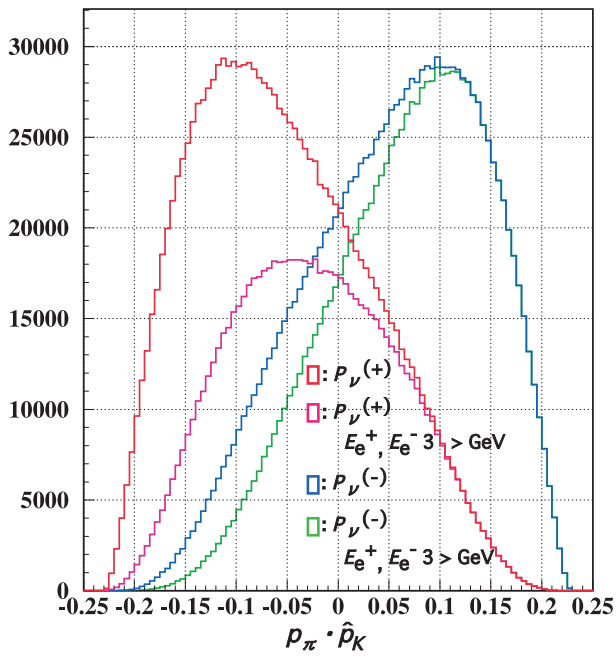

Figure G.1: Distributions of the longitudinal momentum of pion in the kaon rest frame referred to the kaon momentum in the laboratory frame, before and after requiring $E_\pi > 10$ GeV for the groups of events, having E_K maximum solution and having E_K minimum solution.

G.2.2 The electron and positron energy cuts

The cuts on the energy of $e^\pm$ in the pair, $Ee > 3$ GeV, changes the *Slope* as:

$$(3.01 \pm 0.05) \times 10^{-2} \rightarrow (2.39 \pm 0.14) \times 10^{-2} \quad \text{for } t/M_\pi^2 \text{ (max)},$$

$$(3.05 \pm 0.05) \times 10^{-2} \rightarrow (3.12 \pm 0.14) \times 10^{-2} \quad \text{for } t/M_\pi^2 \text{ (min)}.$$

As shown in Fig. G.2, the $Ee > 3$ GeV cut rejects many low energy electron events. When we require electrons to have energy greater than 0.02 GeV in the kaon rest frame, the *Slope* becomes $(2.34 \pm 0.10) \times 10^{-2}$ for t/M_π^2 (max) and $(2.48 \pm 0.10) \times 10^{-2}$ for t/M_π^2 (min). We will explain why the *Slope* is smaller for large electron energy, in the following subsection.

G.2.3 The reason why the *Slope* is smaller for large electron energy

In the $K_L \rightarrow \pi^\pm e^{\mp(}\bar{\nu}^{)}$ decay, NLO makes a correction on the K-π current as a function of the transition momentum, $P_K - P_\pi$, where P_K and P_π are the 4-momentum of kaon and

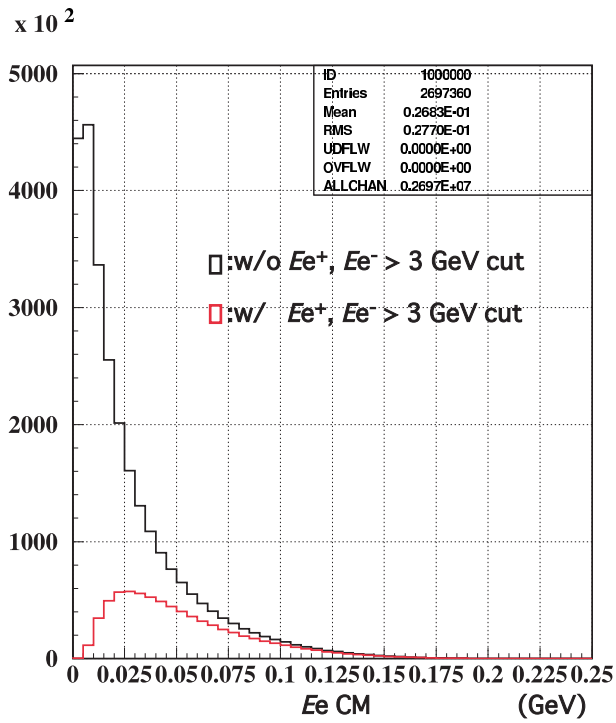

Figure G.2: The energy distributions of the electrons of e^+e^- pair in the kaon rest frame without and with the requiring its energy in the laboratory frame to be greater than 3 GeV.

pion, respectively. If this is also the case for the $K_L \to \pi^\pm e^{\mp(-)}\nu e^+e^-$ decay, the transition momentum Q should be:

$$Q = P_K - P_\pi \quad \text{(for the amplitude that } e^\pm_{Ke3} \text{ radiates a virtual photon)}, \tag{G.1}$$

$$Q = P_K - P_\pi - q \quad \text{(for the amplitude that } \pi^\mp \text{ radiates a virtual photon)}, \tag{G.2}$$

where q is the 4-momentum of the virtual photon. This assumption corresponds to the model that the $K_L \to \pi^\pm e^{\mp(-)}\nu e^+e^-$ decays are dominated by the $K_L \to \pi^\pm e^{\mp(-)}\nu$ decays radiating the virtual photon by inner bremsstrahlung off the pion and the electron [42]. In the experiment, what we measured was the $t \equiv (P_K - P_\pi)^2$. For events with a virtual photon radiating from $e^\pm_{ke3}$, the NLO correction for t is the same as the correction for the same Q^2.

However, for events with a virtual photon radiating from the π, the NLO correction has a smaller t dependence for the following reason.

For these events,

$$t = (Q+q)^2 = M_Q^2 + M_{e^+e^-}^2 + 2(E_Q E_q - |\boldsymbol{Q}||\boldsymbol{q}|\cos\theta_{Q-q}), \tag{G.3}$$

where M_Q and $M_{e^+e^-}$ are the invariant masses of Q and e^+e^- pair, respectively. E_Q (E_q) is the energy, and $\boldsymbol{Q}$ ($\boldsymbol{q}$) is the 3-momentum of Q (q). θ_{Q-q} is the angle between $\boldsymbol{Q}$ and $\boldsymbol{q}$. Since most of the virtual photon is co-linear with pion[1], and Q system and pion tend to be emitted back to back in the kaon rest frame[2], $\cos\theta_{Q-q}$ is negative, and this makes t much larger than Q^2. When the NLO correction has a certain positive dependence on Q^2, t dependence of NLO correction becomes smaller because corresponding Q^2 is smaller than t. This effect is emphasized when $\boldsymbol{q}$ is larger, i.e., E_{e^+} and E_{e^-} are larger.

G.2.4 The reason of the difference between *Slope*s and shapes of t/M_π^2 for E_K maximum and for E_K minimum after $E_{e^+}, E_{e^-} > 3$ GeV cuts

Figure G.3 (a) and (b) show the longitudinal momentum distribution of $e^\pm_{ke3}$ and the virtual photon in the kaon rest frame, along the kaon momentum in the laboratory frame. After $E_{e^+}, E_{e^-} > 3$ GeV/c^2 cuts, both $e^\pm_{ke3}$ and γ^* are preferred to go downstream in the kaon rest frame. As shown in Fig. G.3 (c), this phenomena selects more events with pions going upstream in the kaon rest frame. For the $P_\nu^{(-)}$ events, this lowers the average pion momenta and increase $|\boldsymbol{Q}|$, and vice versa for the $P_\nu^{(+)}$ events. Consequently, the large $|\boldsymbol{Q}|$ in the $K_L \to \pi^\pm e^{\mp(-)}\bar{\nu} e^+e^-$ phase space reduces the effect of $t > Q^2$.

Figure G.3 (d) shows the difference of shapes of t distribution between for $P_\nu^{(+)}$ events and for $P_\nu^{(-)}$ events, like for t/M_π^2 (max) and for t/M_π^2 (min) in Fig. 5.1.

G.2.5 Validation of the hypothesis of the effect of that t becomes greater than Q^2

In Fig. G.4, the amplitude (b) in which the photon is anti-co-linear with their mother particle, has negative value of cosine between the photon and its mother particle, so that

[1]Inner bremsstrahlung photon is co-linear with its mother particle, because the denominator of the propagator of mother particle is $(2Pq + q^2)$, where P is 4-momentum of radiating particle, and Pq equals to $E_P E_q - |\boldsymbol{P}||\boldsymbol{q}|\cos\theta_{Pq}$, where $\boldsymbol{P}$ and $\boldsymbol{q}$ are the 3-momenta for P and q, respectively.

[2]Kaon and pion is pseudo-scaler meson and electron and neutrino has spin 1/2 fermion.

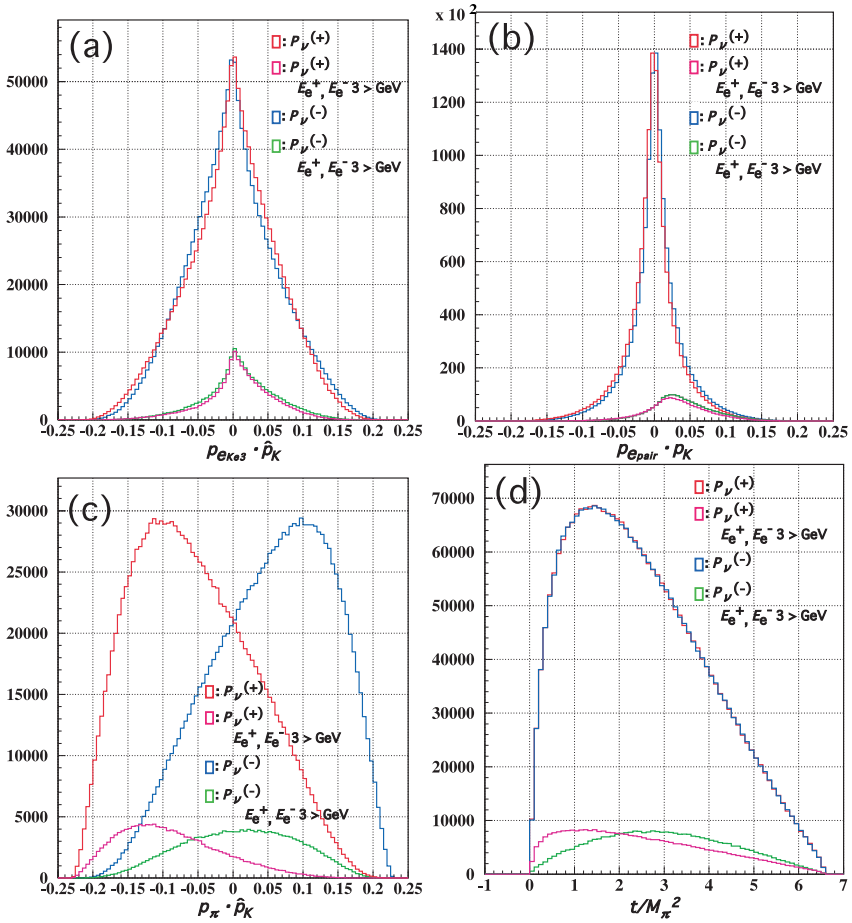

Figure G.3: Distributions of the longitudinal momenta of particles in the kaon rest frame referred to the kaon momentum in the laboratory frame for (a) $e^{\pm}_{ke3}$, (b) electron of the e^+e^- pair, and (c) pion, and distribution of t/M_π^2. Each figure has plots for the event groups which have the E_K maximum or the E_K minimum and without or with $E_{e^+}, E_{e^-} > 3$ GeV cut.

the dominant decays are strongly contributed by the amplitude (a) in which the photon is co-linear with either their mother particle. Figure G.5 (a) shows the distribution of cosines of the angle between the projected γ^* and $e^{\pm}_{ke3}$ momenta on the plane perpendicular to the kaon momentum in the laboratory frame ($\cos\theta_{\perp e-q}$). There is a peak at $\cos\theta_{\perp e-q} = 1$, where events are strongly contributed by the amplitude having inner bremsstrahlung off the electron. Additionally, there is a second peak at $\cos\theta_{\perp e-q} = -1$, where events are strongly contributed by the amplitude having inner bremsstrahlung off the pion. We confirmed this by the plot in Fig. G.5 (b) that the distribution of $\cos\theta_{\perp\pi-q}$ for the events having $\cos\theta_{\perp e-q} < -0.5$ where $\theta_{\perp\pi-q}$ is the angle between the projected pion and virtual photon momenta on the plane perpendicular to the kaon momentum in the laboratory frame.

Table G.2: Effects of the $E_{e^+}, E_{e^-} > 3$ GeV cuts on the slope of the (MC-NLO)-to-(MC-LO) ratio.

	Whole	IB_e	IB_π
w/o $E_e > 3$ GeV cut	4.65±0.05	5.69±0.08	3.11±0.12
w/ $E_e > 3$ GeV cut	3.79±0.14	5.40±0.21	2.31±0.33
			$(\times 10^{-2})$

We call the events in $\cos\theta_{\perp e-q} > 0.5$ as IB_e events, in $\cos\theta_{\perp e-q} < -0.5$ as IB_π events and others. We will show that the events with large Ee radiating off the pion contribute to reduce the *Slope*.

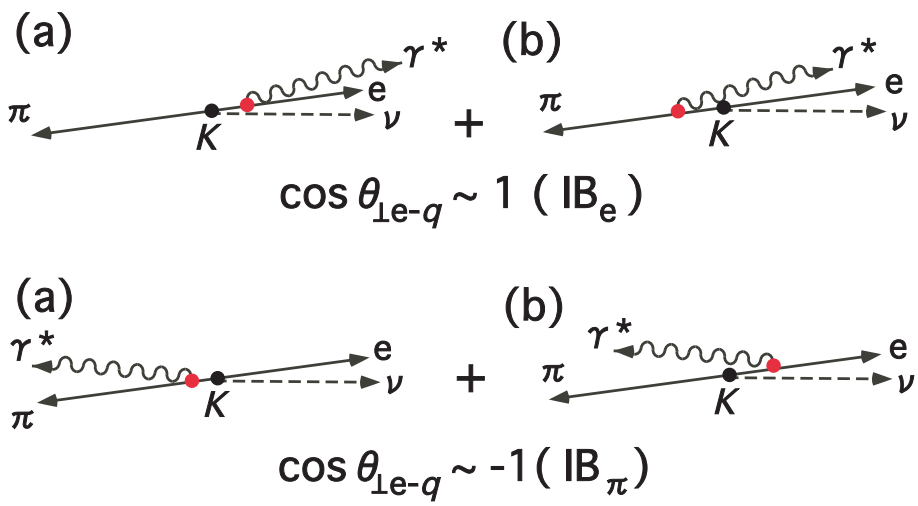

Figure G.4: Schematics for the amplitude of events which have the virtual photon is co-linear with the electron (top), and the pion (bottom).

Table G.2 shows the slope for IB_e events and IB_π events, with and without the $E_{e^+}, E_{e^-} > 3$ GeV cut. First, independent of the $E_{e^+}, E_{e^-} > 3$ GeV cut, the IB_e events have larger *Slope* than the IB_π events. This is because for the IB_e events, t is equal to Q^2, and this sensitive to NLO correction, whereas for the IB_π events the t is polluted with low Q^2 events. Second, for the IB_e events, the change of *Slope* by the $E_{e^+}, E_{e^-} > 3$ GeV cut is less than 1 σ because $t = Q^2$ holds. Third, for the IB_π events, the slope is reduced by $26 \pm 11\%$ by the $E_{e^+}, E_{e^-} > 3$ GeV cuts, because the cut enhances lower Q^2.

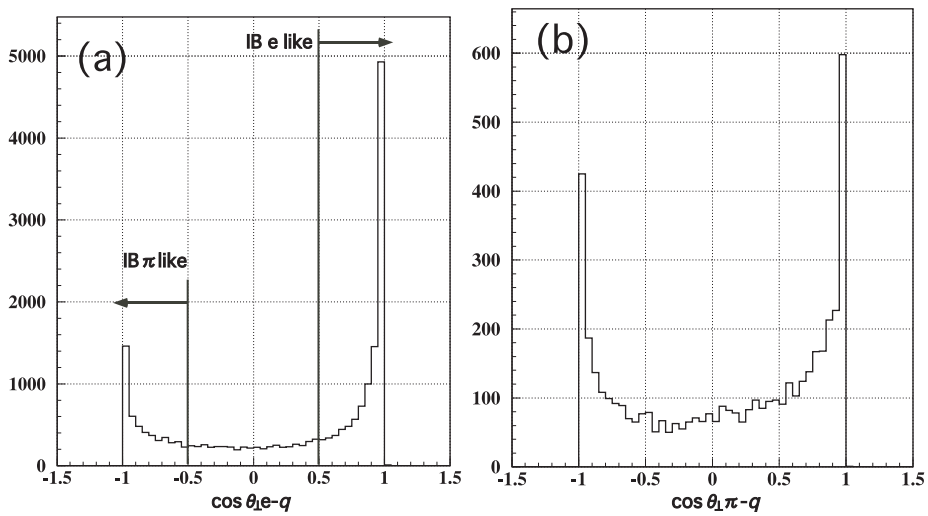

Figure G.5: (a) Distribution of cosines of the angle between the perpendicular component of momentum of $e^{\pm}_{ke3}$ and the virtual photon referred to the kaon momentum in the laboratory frame ($\cos\theta_{\perp e-q}$). (b) Distribution of $\cos\theta_{\perp\pi-q}$ for the events having $\cos\theta_{\perp e-q} < -0.5$, where $\cos\theta_{\perp\pi-q}$ is cosine of the angle between the perpendicular component of momentum of pion and the virtual photon referred to the kaon momentum in the laboratory frame.

G.3 data / MC-LO

G.3.1 The square of the transition momentum

To investigate that the above discussions are consistent with data, we repeated the same study described in Appendix G.2.5, for data. The analysis cuts are the same as listed in Table 3.2.

Table G.3 shows the *Slope*s of the data-to-(MC-LO) ratio for the IB_e events, IB_π events, and whole events. As in MC-NLO / MC-LO, the *Slope* for the IB_e events is larger than IB_π events, and the *Slope* for the IB_e events is insensitive to the choice of E_K solutions, whereas the *Slope* for the IB_π events is sensitive to the choice of E_K solutions.

G.4 Conclusions

The correction to the leading order of χPT by the next to leading order is sensitive to the transition momentum $t \equiv (P_K - P_\pi)^2$. The theoretical calculation predicts that *Slope* of

Table G.3: The slopes of the data-to-(MC-LO) ratio for the IB_e events and the IB_π events
.

	t/M_π^2(max)	t/M_π^2(min)
Whole	2.5±0.6	3.7±0.7
IB_e	4.9±0.9	5.5±0.9
IB_π	1.3±1.2	4.4±1.5
		($\times 10^{-2}$)

linear fitted line to the NLO / LO ratio of the t/M_π^2 dependence is 5×10^{-2}, but data / MC-LO has a smaller *Slope*. There are two reasons:

1. The square of the transition momentum t has a two-fold ambiguity due to the two-fold ambiguity of the energy of kaon. For a half of events, incorrect solution is chosen, and in that case, the *Slope* is smaller. Therefore, the *Slope* for the whole events is reduced from the true slope.

2. For the amplitude with virtual photon radiating from π, the transition momentum of the K-π current should be $Q \equiv P_K - P_\pi - q$, and $t = (Q+q)^2$. Most of events have a small opening angle between γ^* and π, and it makes t larger than Q^2. When the NLO correction has a certain positive dependence on Q^2, t dependence of NLO correction becomes smaller for those events. This effect becomes larger for larger $|\boldsymbol{q}|$. Since high Ee is required in the experimental analysis, the t dependence on the NLO correction was reduced.

The other question on the t spectrum is the large difference of shapes of spectra between for E_K maximum solution and for E_K minimum solution. Requiring $E_{e^+}, E_{e^-} > 3$ GeV tends to collect the events having $e^\pm_{ke3}$ and the virtual photon going downstream, and pions going upstream in the kaon rest frame. This causes that $P_\nu^{(-)}$ events to have larger Q^2 than $P_\nu^{(+)}$ events. Consequently, the $P_\nu^{(-)}$ events provide larger t/M_π^2 for the minimum E_K solution, than the $P_\nu^{(+)}$ events providing t/M_π^2 for the maximum E_K solution.

Appendix H

A study of the shift of Z-vertex of e^+e^- pair

We show that the two-track vertex has tendency to be measured downstream of the actual position.

Suppose that one of two tracks A penetrates the spectrometer along the z axis, and the other has an angle (θ) with A. The original z-vetex position is at z = 100 m. For simplicity, only B is fluctuated by a multiple scattering according to an Gaussian distribution in the Drift chamber 1 at z = 160 m. The angle of fluctuation is symmetric with respect to the original trace B. However, the projection of the result of fluctuation on A is asymmetric. When the fluctuation results the vertex shift upstream, the shift is larger than when the result of fluctuation shifts the vertex downstream, even the angles of fluctuation in DC1 are similar (Fig. H.1). This effect is large, when the opening angle θ is small. The projection of Gaussian distribution from the DC1 to the z-axis (Fig. H.2 (a)) is the probability of the location of the reconstructed vertex after the fluctuation. The plots in Fig. H.2 (a) were calculated as a projected Gaussian function on the z-axsis from the DC1 with the model in Fig. H.1. The symmetry of the fluctuation remains in the fact when we integrate the probability function in Fig. H.2 (a) from infinitely far upstream. However, our detector is not infinite.

Figure H.2 (b) shows the distribution of the vertices of the e^+e^- pairs whose four-track

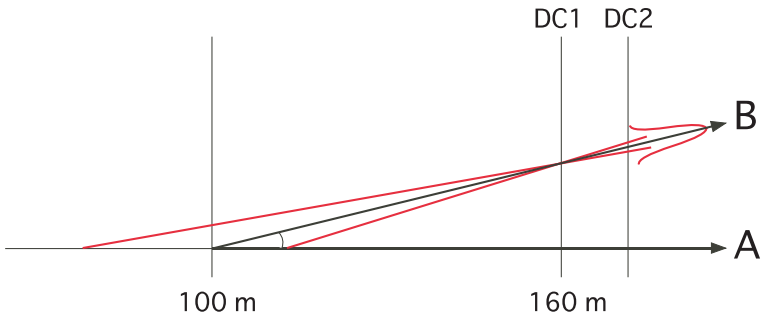

Figure H.1: A simple model where the deviation of vertex is asymmetric between downstream and upstream.

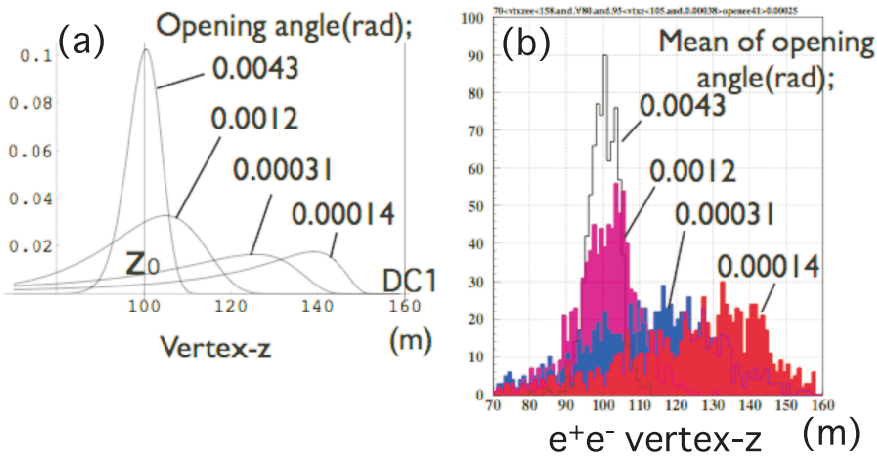

Figure H.2: (a) Projected Gaussian distribution from the DC1 in Fig. H.1 to the z axis. (b) The Z-vertex of e^+e^- pair of the events which have 4-track vertex at z = 100 m.

vertices are at z = 100 m. Our model represent data well.

Bibliography

[1] T. Alexopoulos *et al.* [KTeV Collaboration], Phys. Rev. D **70**, 092007 (2004) [arXiv:hep-ex/0406003].

[2] J. Gasser and H. Leutwyler, Annals Phys. **158**, 142 (1984).

[3] Y. Nambu, Phys. Rev. Lett. **4**, 380 (1960).

[4] Y. Nambu, Phys. Rev. **117**, 648 (1960).

[5] H. W. Fearing, E. Fischbach and J. Smith, Phys. Rev. D **2**, 542 (1970).

[6] F. E. Low, Phys. Rev. **110**, 974 (1958).

[7] K. Tsuji, Private communication.

[8] A. Alavi-Harati *et al.* [KTeV Collaboration], Phys. Rev. D **67**, 012005 (2003) [Erratum-ibid. D **70**, 079904 (2004)] [arXiv:hep-ex/0208007].

[9] A. Alavi-Harati *et al.* [KTeV Collaboration], Phys. Rev. Lett. **93**, 021805 (2004) [arXiv:hep-ex/0309072].

[10] V. Bocean *et al.*, Technical Report TM-2046, Fermilab.

[11] G. Graham, Ph.D. thesis (The University of Chicago, August 1999).

[12] J. Whitmore, "The performance of a high speed pipelined photomultiplier readout system Nucl. Instrum. Meth. A **409**, 687 (1998).

[13] P. S. Shawhan, Ph.D. thesis (The University of Chicago, September 1999).

[14] R. Brun *et al.*, GEANT 3.21, CERN, Geneva, (1994).

[15] G. B. Quinn, Ph.D. thesis (The University of Chicago, June 2000).

[16] P. S. Shawhan, "A Y Track Finder for KTeV", KTeV internal Note 257(1994)

[17] C. Bown, E. Cheu, J. Dusatko, H. Sanders and M. Zeleznik, Nucl. Instrum. Meth. A **369**, 248 (1996).

[18] A. J. Malensek, FERMILAB-FN-0341

[19] E. Barberio and Z. Was, "PHOTOS: A Universal Monte Carlo for QED radiative corrections. Version Comput. Phys. Commun. **79**, 291 (1994).

[20] Z. Was and P. Golonka, Nucl. Phys. Proc. Suppl. **144**, 88 (2005) [arXiv:hep-ph/0411377].

[21] M. A. Barrio, Ph.D. thesis (The university of Chicago, December, 2001).

[22] P. A. Toale, Ph.D. thesis (The university of Colorado, Boulder, 2004).

[23] T. Miyazaki and E. Takasugi, Phys. Rev. D **8**, 2051 (1973).

[24] F. Leber *et al.*, Phys. Lett. B **369**, 69 (1996).

[25] P. Basile *et al.*, Phys. Lett. B **36**, 619 (1971).

[26] G. Makoff *et al.*, Phys. Rev. Lett. **70**, 1591 (1993) [Erratum-ibid. **75**, 2069 (1995)].

[27] H. A. Bethe, Phys. Rev. **89**, 1256 (1953).

[28] W. R. Nelson *et al.*, SLAC Report 265, SLAC preprint(1985).

[29] W.-M. Yao *et al.*, J. Phys. G **33**, 1 (2006)

[30] H. Ping, PhD thesis (University of Wisconsin, Madison, 2005).

[31] K. Senyo, Ph.D. thesis (Osaka university, 1999).

[32] T. Alexopoulos *et al.* [KTeV Collaboration], Phys. Rev. D **70**, 092006 (2004) [arXiv:hep-ex/0406002].

[33] J. A. Graham, Ph.D thesis (University of Chicago, 2001)

[34] J. LaDue, Ph.D thesis (University of Colorado, Boulder, 2003)

[35] S. Bijnens, G. Ecker, J. Gasser, The second DA*Phi*NE Physics Handbook, 125 (1994) [arXiv:hep-ph/9411232].

[36] R. Kessler, Private communication.

[37] V. Cirigliano, H. Neufeld and H. Pichl, Eur. Phys. J. C **35**, 53 (2004) [arXiv:hep-ph/0401173].

[38] M. Gell-Mann, R. J. Oakes and B. Renner, "Behavior Of Current Divergences Under SU(3) X SU(3)," Phys. Rev. **175**, 2195 (1968).

[39] F. James, Monte Carlo Phase space, CERN 68-15 (1968).

[40] R. Hagedorm, "Relativistic kinematics (Benjamin, N.Y., 1964)

[41] K. Hanagaki, Ph.D thesis (Osaka university, 1998)

[42] T. C. Andre, Nucl. Phys. Proc. Suppl. **142**, 58 (2005).